

Structure, Chemistry, and Energetics of Organic and Inorganic  
Adsorbates on Ga-Rich GaAs and GaP(001) Surfaces

Thesis by  
Seokmin Jeon

In Partial Fulfillment of the Requirements  
for the Degree of  
Doctor of Philosophy



CALIFORNIA INSTITUTE OF TECHNOLOGY  
Pasadena, California  
2014  
(Defended September 30, 2013)



“No Pain, No Gain.”

## ACKNOWLEDGEMENTS

I remember my wonderful mood when I first visited Caltech as a prospective student. Just before I came to Caltech, I visited the Columbia University, New York for the same purpose. I found everything in Pasadena including weather and people's attitudes was attractive to me in contrast to what I found in New York. Living and studying in this beautiful place has been my best pleasure. Many individuals have supported, helped, and encouraged me to complete my Ph.D. course at Caltech, so it is my great pleasure to acknowledge them.

I would like to thank my advisor, Professor Harry Atwater for his guidance and support. Especially, I appreciate him for providing me a great deal of freedom and independence on my thesis research. He has also shown me the wisdom, leadership, and enthusiasm that a leading scientist owns. My thesis committee, Professors Bill Goddard, Nate Lewis, and Jack Beauchamp are also my role models. It was my pleasure and honor to be advised by such great scientists.

Many people in the Atwater group have contributed to the successful completion of my thesis research. Particularly, I would like to thank Jeff Bosco, Victor Brar, Seyoon Kim, Samantha Wilson, Min Jang, Jim Fakonas, Dan Tuner-Evans, Chris Chen, Yulia Tolstova, Hal Emmer, John Lloyd, Carissa Eisler, Siying Peng, Sunita Darbe, Amanda Shing, Imogen Pryce, Michael Kelzenberg, Jonathan Grandidier, Marina Leite, Gerald Miller, Vivian Ferry, Stanley Burgos, Ryan Briggs, Andrew Leenheer, Greg Kimball, Adele Tamboli, Deidre O'Caroll, Domenico Pacifici, Davis Darvish, Morgan Putnam, and Matt Sheldon for sharing their knowledge and skills, having time to discuss about research and science, and being good friends. Many thanks also go to the other group members—Cristofer Flowers, Ruzan Sokhoyan, Ana Brown, Raymond Weitekamp, Anna Beck, Howard Lee, Dennis Callahan, Emily Warmann, Naomi Coronel, Emily Kosten, Prineha Narang, Kelsey Whitesell, Sondra Hellstrom, Kate Fountaine, Koray Aydin, Michael Deceglie, Kenneth Diest, Jennifer Dionne, Eyal Feigenbaum, Krista Lageland, and Jeremy Munday. Every single person in the Atwater group is always nice, friendly, and helpful to me.

I have also benefited from several scientists outside the Atwater group. These scientists not only provided skills and scientific advice, but also friendship. I would like to thank Dr. Ungdon Ham and Sangyeob Lee for sharing skills about UHV-STM instrumentation, Dr. Hyungjun Kim for instructing me DFT calculations, Joseph for training XPS, Jean for training HREELS and AES, and Matt Roberts of Omicron Nanotechnology for kind and quick answers for a number of my questions.

I also would like to appreciate the Caltech Korean Graduate Society. From the first day I arrived at LAX to now, they have been friends and family. They have also shared with me plenty of invaluable knowledge about living and family life, which has saved me much time and effort and helped me enjoy this area. Thanks go to Sanghee Park, Young Hyun Kim, Hyojong Lee, Ji hun Kim, Wonhee Lee, Jina Choi, Young Shik Shin, Hanseuk Lee, Junho Suh, In Ho Cho, Jungwook Park, Hoyong Chung, Sungwook Woo, Shinchul Yeom, Taeshik Oh, Min Jung Kang, Chang Ho Sohn, Jaewon Song, Changsoon Park, Daegyeoum Kim, Sang-Mok Lee, Giwook Hwang, Chanyeon Park, Hyungjun Ahn, Seyoon Kim, Hee-jung Chung, Haekong Kim, Minseok Jang, Jeelson Choi, and Mooseok Jang. Without this society, living in Pasadena would not be as exciting and pleasing as it is. I also would like to thank Su Young Ryu, Son Jong Hwang, and Yun-Geun Kim for much advising and mentoring.

I would like to thank my former adviser Professor Sehun Kim for being a constant source of advice and support. He has been the first professor that I contact when I need help. I really appreciate his help. I also thank Professor Hangil Lee for support and encouragement.

I am thankful for the funding support from Kwanjeong Educational Foundation which has supported my tuition and stipend for four years without any cost to me.

Special thanks to my old friends—Bongsu Kim, Gyu Nam Lee, Jae Chul Lee, Ju Han Song, Kwon Ho, Tae Hun Kim, Sung Hoon Choi, and Nicola's for continuous encouragement. I am also thankful to Wooram Lee for unexpected encouraging messages.

I am grateful for support from my parents and elder sister. I owe not just my PhD, but my entire career, to their support and encouragement. I also thank my parents-in-law for encouraging and praying for me.

Lastly, I acknowledge my wife Soojeong, son Yoonwoo, and prospective daughter Tori. Soojeong is amazingly supportive and persistently encourage me for the last four and half years. She also brought me adorable children who are the most significant and precious parts in my life. I sincerely thank her for loving, encouraging, and supporting me. I also thank Yoonwoo and Tory for growing well without serious sickness. Yoonwoo has given me big smiles and warm hugs whenever I come back home after hard work, which cures my tired body. I really thank him.

## ABSTRACT

The work described in this dissertation includes fundamental investigations into three surface processes, namely inorganic film growth, water-induced oxidation, and organic functionalization/passivation, on the GaP and GaAs(001) surfaces. The techniques used to carry out this work include scanning tunneling microscopy (STM), X-ray photoelectron spectroscopy (XPS), and density functional theory (DFT) calculations. Atomic structure, electronic structure, reaction mechanisms, and energetics related to these surface processes are discussed at atomic or molecular levels.

First, we investigate epitaxial  $\text{Zn}_3\text{P}_2$  films grown on the Ga-rich GaAs(001)( $6\times 6$ ) surface. The film growth mechanism, electronic properties, and atomic structure of the  $\text{Zn}_3\text{P}_2/\text{GaAs}(001)$  system are discussed based on experimental and theoretical observations. We discover that a P-rich amorphous layer covers the crystalline  $\text{Zn}_3\text{P}_2$  film during and after growth. We also propose more accurate picture of the GaP interfacial layer between  $\text{Zn}_3\text{P}_2$  and GaAs, based on the atomic structure, chemical bonding, band diagram, and P-replacement energetics, than was previously anticipated.

Second, DFT calculations are carried out in order to understand water-induced oxidation mechanisms on the Ga-rich GaP(001)( $2\times 4$ ) surface. Structural and energetic information of every step in the gaseous water-induced GaP oxidation reactions are elucidated at the atomic level in great detail. We explore all reasonable ground states involved in most of the possible adsorption and decomposition pathways. We also investigate structures and energies of the transition states in the first hydrogen dissociation of a water molecule on the ( $2\times 4$ ) surface.

Finally, adsorption structures and thermal decomposition reactions of 1-propanethiol on the Ga-rich GaP(001)( $2\times 4$ ) surface are investigated using high resolution STM, XPS, and DFT simulations. We elucidate adsorption locations and their associated atomic structures of a single 1-propanethiol molecule on the ( $2\times 4$ ) surface as a function of annealing temperature. DFT calculations are carried out to optimize ground state structures and search transition states. XPS is used to investigate variations of the chemical bonding nature and coverage of the adsorbate species.

## TABLE OF CONTENTS

Acknowledgements .....	iv
Abstract.....	vi
Table of Contents .....	vii
List of Figures.....	ix
List of Tables.....	xi
Nomenclature .....	xii
Chapter I: Introduction.....	1
1.1 Surfaces of III-V semiconductors .....	1
1.2 Major surface study tools used in this dissertation.....	2
1.3 Summary.....	8
Chapter II: Growth Mechanism and Electronic Structure of Zn <sub>3</sub> P <sub>2</sub> on a Ga-Rich GaAs(001) Surface .....	10
2.1 Introduction.....	10
2.2 Experimental and computational details.....	11
2.3 Scanning tunneling microscopy .....	15
2.4 Scanning tunneling spectroscopy.....	20
2.5 X-ray photoelectron spectroscopy .....	22
2.6 Density functional theory calculations.....	26
2.7 Conclusion .....	28
Chapter III: DFT Study of Water Adsorption and Decomposition on a Ga-Rich GaP(001)(2×4) Surface .....	30
3.1 Introduction.....	30
3.2 Computational details.....	31
3.3 Result and discussion .....	33
3.3.1 The reconstructed GaP(001)(2×4) surface.....	33
3.3.2 Premise and scope of the simulation.....	34
3.3.3 Molecular adsorption state.....	36
3.3.4 HO/H decomposition state.....	37
3.3.5 O/2H decomposition state .....	39
3.3.6 Surface oxide state (O/H <sub>2</sub> state).....	41
3.3.7 Overall reaction mechanism.....	45
3.4 Conclusion .....	48
Chapter IV: Investigation of Adsorption Geometries and Thermal Decomposition Reactions of Alkanethiol Molecules on a Ga-Rich GaP(001)(2×4) Surface.....	50
4.1 Introduction.....	50
4.2 Experimental and computational details.....	51
4.3 Results and discussion.....	55
4.3.1 Scanning tunneling microscopy .....	55
4.3.2 X-ray photoelectron spectroscopy.....	65
4.3.3 Density functional theory calculations .....	69
4.4 Conclusion .....	75

Summary.....	76
Bibliography.....	79
Appendix.....	86

## LIST OF FIGURES

<i>Number</i>	<i>Page</i>
1.1 STM images/STS spectra of Si(111) (7×7) .....	4
1.2 Survey and high-resolution XPS spectra of Zn <sub>3</sub> P <sub>2</sub> /GaAs(001) .....	6
1.3 Cluster and periodic slab models for DFT calculations .....	8
2.1 STM images of clean GaAs(001)(6×6) and Zn <sub>3</sub> P <sub>2</sub> /GaAs(001) .....	16
2.2 HRXRD scans of Zn <sub>3</sub> P <sub>2</sub> films on GaAs(001) .....	17
2.3 TEM images of Zn <sub>3</sub> P <sub>2</sub> /GaAs(001) interfaces .....	17
2.4 HRSTM images of clean GaAs(001)(6×6) and Zn <sub>3</sub> P <sub>2</sub> /GaAs(001) .....	19
2.5 STS spectra of clean GaAs(001)(6×6) and Zn <sub>3</sub> P <sub>2</sub> /GaAs(001) .....	21
2.6 P 2p core-level XPS spectra of Zn <sub>3</sub> P <sub>2</sub> /GaAs(001) and Zn <sub>3</sub> P <sub>2</sub> /GaP(001) .....	23
2.7 XPS spectra and energy band alignment of Zn <sub>3</sub> P <sub>2</sub> /GaAs(001) .....	25
2.8 P replacement energetics by DFT calculations .....	27
2.9 Schematic pictures of film growth mechanism of Zn <sub>3</sub> P <sub>2</sub> /GaAs(001) .....	29
3.1 Periodic slab model of a Ga-rich GaP(001)(2×4) mixed-dimer .....	33
3.2 Water/GaP(001)(2×4): molecular adsorption state .....	35
3.3 Water/GaP(001)(2×4): HO/H decomposition state .....	38
3.4 Water/GaP(001)(2×4): O/2H decomposition state .....	39
3.5 Water/GaP(001)(2×4): surface oxide state .....	42
3.6 Water/GaP(001)(2×4): adsorption energies vs. reaction coordinates .....	44
4.1 Cluster model of a Ga-rich GaP(001)(2×4) mixed-dimer .....	54
4.2 STM images of a Ga-rich GaP(001)(2×4) surface reconstruction .....	56
4.3 STM images of 1-propanethiol/GaP(001)(2×4) at various temperatures .....	58
4.4 HRSTM images and line profiles of 1-propanethiol/GaP(001)(2×4) .....	59
4.5 STM images of 1-propanethiol/GaP(001)(2×4) annealed at 400 °C .....	62
4.6 STM images of various organosulfurs on GaP(001)(2×4) at 120~130 K .....	63
4.7 XPS spectra of 1-propanethiol/GaP(001)(2×4) at various temperatures .....	66
4.8 H dissociation of 1-propanethiol on GaP(001)(2×4): structures .....	69
4.9 H dissociation of 1-propanethiol on GaP(001)(2×4): plotting energies .....	70
4.10 Ground state structures of 1-propanethiol on GaP(001)(2×4) .....	72
A.1 Drawing and picture of the previous STM system .....	86

A.2 Drawing and picture of the first generation STM system .....	87
A.3 Drawing and picture of the second generation STM system.....	88
A.4 Comparison of noise levels .....	89

## LIST OF TABLES

<i>Number</i>	<i>Page</i>
3.1 Structural parameters of the Ga-rich GaP(001)(2×4) mixed-dimer.....	34
3.2 Structural parameters: molecular adsorption states in H <sub>2</sub> O/GaP .....	36
3.3 Structural parameters: HO/H decomposition states in H <sub>2</sub> O/GaP .....	38
3.4 Structural parameters: O/2H decomposition states in H <sub>2</sub> O/GaP .....	40
3.5 Structural parameters: surface oxide states in H <sub>2</sub> O/GaP .....	43
4.1 XPS data of 1-propanethiol on GaP(001)(2×4) at various temperatures .....	67
4.2 Comparison of activation/ground state energies from literature .....	71

## NOMENCLATURE

**UHV.** Ultra-high vacuum.

**STM.** Scanning tunneling microscope or microscopy.

**XPS.** X-ray photoelectron spectroscopy.

**DFT.** Density functional theory.

**TEM.** Transmission electron microscope or microscopy.

**XRD.** X-ray diffraction.

**RT.** Room temperature.

**HR.** High resolution.

**GaP.** Gallium Phosphide.

**GaAs.** Gallium Arsenide.



## *Chapter 1*

# Introduction

## 1.1 Surfaces of III-V semiconductors

Group III-V compound semiconductors and their alloys are very intriguing and useful materials such that they have been drawing much attention from scientists and engineers for the last few decades. A variety of compound semiconductors can be synthesized by alloying group III (B, Al, Ga, In) and group V (N, P, As, Sb) atoms, and the resultant semiconductors have a variety of chemical, electrical, and optical properties which are useful for applications such as transistors, light-emitting diodes (LED), photovoltaic devices, photoelectrochemical devices, light sensors, chemical sensors, etc.

Gallium arsenide (GaAs) has desirable electronic and optical properties of significant industrial/research interest. The direct band gap, 1.42 eV, is close to the ideal for a single-junction photovoltaic device with which one expects to achieve theoretically maximum power conversion efficiency. Strong light absorption from a direct band gap allows all the light with energy greater than the band gap to be completely absorbed within 1  $\mu\text{m}$  of the surface. The high electron mobility of up to  $\sim 8500 \text{ cm}^2/\text{V}\cdot\text{s}$  can be utilized in high performance transistors which need a good channel material.[1] A variety of alloy materials based on GaAs support many applications which need tunable optoelectronic properties. The current state-of-the-art GaAs photovoltaic cell achieves 28.2 % efficiency, which is the highest value among the single junction solar cells introduced to date. [2]

GaP is also a very intriguing emerging material especially in renewable energy research fields. Its favorable properties, which create a lot of potential applications, include control of electronic properties by forming InGaP alloys [3] and epitaxial film growth on a silicon substrate due to small lattice mismatch (0.36%). [4, 5] In addition,  $\text{H}_2$  production or  $\text{CO}_2$  reduction can be achieved in aqueous photoelectrochemical systems based on a single crystal GaP, making it of great interest for renewable energy research. [6-8]

Studying the surfaces of the GaAs and GaP is significant since both materials suffer from degradation of electronic properties due to a high density of surface states.[9, 10] This is one of the largest barriers to the widespread use of compound semiconductors instead of Si, despite their superior optoelectronic properties. Therefore, the need to develop a method to protect and passivate the surfaces has driven the surface science research of these materials.

Furthermore, chemical functionalization is also a significant factor in motivating the surface study of these materials. Chemical attachment on inorganic semiconductor surfaces enables new functionalities. First, building new nanoscale architectures are feasible using a variety of organic and polymer synthesis methods. Second, the electronic properties of the semiconductor are changed due to the donation or depletion of electrons by the chemical adsorbates. Third, it can change the local chemical properties of the surface, such as hydrophobicity. We can modify the surface of an inorganic material, which is less reactive and has a limited variety of chemical availabilities, creating a hybrid organic-inorganic surface which is more reactive and has a variety of chemical functionalities.

## 1.2 Major surface study tools used in this dissertation

### *Scanning tunneling microscopy (STM)*

STM uses a very sharp metallic tip to probe the local structural and electronic properties of a conducting surface. The signal from the STM always contains two information such as topography and electronic structure because the tunneling current ( $I$ ) has an exponential relationship with the tip-sample distance ( $z$ ) and tunneling decay constant ( $\kappa$ ) which reflects the electronic structures of the tip and sample:

$$I = I_0 e^{-2\kappa z}, \quad (1.1)$$

$$\kappa = \frac{\sqrt{2m(\phi - eV)}}{\hbar},$$

where  $m$ ,  $I_0$ ,  $\phi$ ,  $e$ , and  $V$  are electron mass, tunneling current at  $z = 0$ , average work function, elementary charge, and sample bias voltage, respectively.

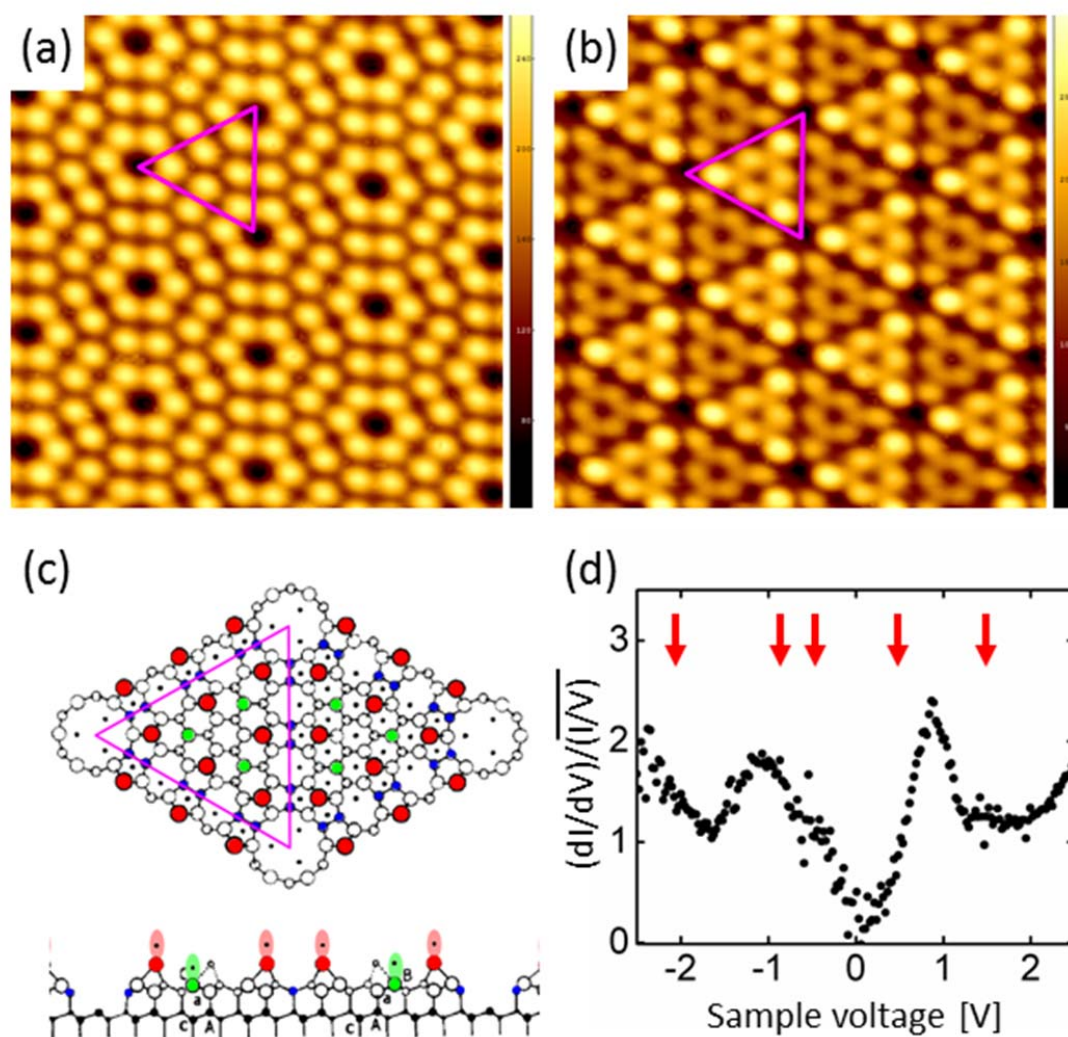
There are two common modes of operation; constant current mode and constant height mode. In the constant current mode, the tunneling current is maintained with an electronic feedback circuit to generate  $Z$  variation while scanning the  $X$ - $Y$  plane. Alternatively, in the constant height mode, the tip-to-sample distance is fixed, and the current signal is recorded. Since the constant height mode does not require a feedback control at each  $X$ - $Y$  scanning point, faster scan rates are achievable. However, there is a risk of crashing the tip on rougher surfaces; thus, the mode is appropriate for applications which need fast scanning on flat surfaces, normally over a small scan area.

Figure 1.1 shows STM images, dimer adatom stacking-fault (DAS) model structure, and tunneling spectra of a clean Si(111)(7×7) surface.[11] In the DAS model (Figure 1.1c), the left half of the (7×7) rhombus marked in a magenta triangle is a stacking fault region. In the STM image obtained at a sample bias voltage of + 1.7 V in Figure 1.1a, there is no difference in STM images of the two half cells. However, in Figure 1.1b, the stacking faulted and unfaulted regions look different. This is a clear example of how STM images contain not only geometric information but also electronic structure information.

Lastly, tunneling spectroscopy gives local electronic structure information as shown in equation (1.2) which is derived based on the Bardeen's theory,

$$I = \frac{4\pi e}{\hbar} \int_0^{eV} \rho_{tip}(E_F - eV + \varepsilon) \rho_{sample}(E_F + \varepsilon) |M|^2 d\varepsilon, \quad (1.2)$$

where  $\rho$ ,  $E_F$ ,  $V$ , and  $M$  are density of state, Fermi level energy, the sample bias voltage, and tunneling matrix element.[12] Tunneling conductance ( $dI/dV$ ) measured at a certain location of a sample surface is proportional to the local electron density of state at the location. Figure 1.1d shows a tunneling conductance versus sample bias voltage curve. The spectrum is an average of the spectra obtained from random locations on the Si(111) (7×7) surface. The peaks represent the electronic states near the Fermi level and their locations agree relatively well with the previously reported peak locations (red arrows).[13]



**Figure 1.1** a), b) Constant current STM images of a Si(111) (7×7) surface at different sample bias voltages; a)  $V_s = +1.7$  V and b)  $V_s = -1.7$  V. c) The top and side views of the DAS model of the Si(111) (7×7) surface. Red, green, and blue dots represent adatoms, rest atoms, and dimers, respectively. The region in the magenta triangle represents the stacking fault region. The picture is adopted from reference.[11] d) Normalized tunneling conductance versus sample bias voltage spectrum which was averaged over a number of spectra obtained at random locations of the surface. Red arrows show the peak positions of the same surface in reference.[14]

*X-ray photoelectron spectroscopy (XPS)*

XPS uses X-ray photons produced by exciting Al or Mg source materials with high energy electrons. The generated X-ray photons are either used directly or filtered through a monochromator for better energy resolution. The core-level electrons of a sample are excited by the X-ray photons, ejected from the sample, and then collected by an electron analyzer. A hemispherical electron analyzer is typically used for this purpose. The kinetic energy (KE) and momentum of the photoelectron are analyzed in the analyzer to determine the binding energy (BE) according to equation (1.3):

$$KE = h\nu - BE - \phi, \quad (1.3)$$

where  $h\nu$  and  $\phi$  are the incident photon energy and instrument work function, respectively. In addition, simultaneous measurement of the momentum of the photoelectron generates the  $E(k)$  versus  $k$  values to map out the electronic band structure of the sample.

For surface chemistry analysis, the parameters of interest typically include the degree of shift and area of a core-level XPS peak. The existence of a particular peak verifies the existence of a particular element in the detection area of the sample. The core-level peak shift is due to the chemical environment of the element of interest. In addition, the area of the peak is used to obtain quantitative information such as composition, thickness, and coverage.

XPS is a surface sensitive technique since the photoelectron escape depth in a solid material is relatively short, on the order of a few nanometers, while a photon escape depth is on the order of microns. Using an Al X-ray source, the escape depth of a photoelectron is smaller than  $20 \sim 30 \text{ \AA}$ , which implies that  $\sim 10$  monolayers of atoms from the surface are sampled with this method [15].

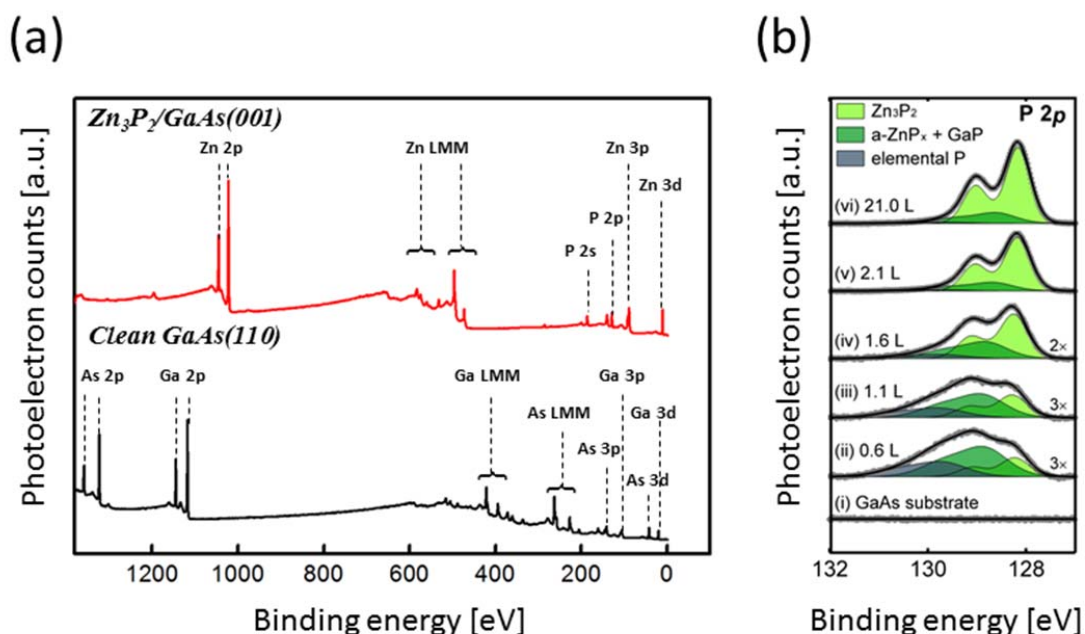


**Figure 1.2** a) XPS survey scans (Al K $\alpha$  source, pass energy of 80 eV) of a clean GaAs(110) surface (black) and 21 L Zn<sub>3</sub>P<sub>2</sub> epitaxial film grown on GaAs(001) at 180 °C. Significant peaks are labeled. b) High-resolution XPS (Al K $\alpha$  source, pass energy of 20 eV) in P 2*p* region with varying coverage of Zn<sub>3</sub>P<sub>2</sub> epitaxial films grown on GaAs(001) at 180 °C. 1 Langmuir (L) = 1 × 10<sup>-6</sup> Torr · sec.

Figure 1.2 displays low- and high-resolution XPS spectra of clean GaAs(110) and Zn<sub>3</sub>P<sub>2</sub>/GaAs(001) surfaces. By assigning the core-level binding energies of constituent elements, the composition of the sample can be verified, as shown in Figure 1.2a. In addition, high resolution spectra allow for resolution of the different oxidation states and chemical bonds of the constituent elements with their neighboring atoms, based on relative shifts in binding energy. For instance, the P 2*p* region in Figure 1.2b is composed of three components with different core-level binding energy shifts which stem from dissimilar chemical environment of each component.

#### *Density Functional Theory (DFT) calculations*

DFT is a method of solving the Schrödinger equation (SE) of a multi-electron system to obtain the ground state energy and electron density. Equation (1.4) is the time-independent non-relativistic Schrödinger equation for a multiple-electron and nucleus system,

$$\left[ -\frac{\hbar^2}{2m} \sum_{i=1}^N \nabla_i^2 + \sum_{i=1}^N V(\mathbf{r}_i) + \sum_{i=1}^N \sum_{j<i} U(\mathbf{r}_i, \mathbf{r}_j) \right] \psi = E\psi. \quad (1.4)$$

The SE contains  $3N$  variables representing the coordinates of  $N$  electrons. Thus, solving this equation and obtaining the wave functions of the electrons is a formidable task. Hohenberg and Kohn proposed that the ground state energy of the SE has a one-to-one correspondence with an electron density function. Using this theorem, the equation (1.4) is modified to the Kohn-Sham equation:

$$\left[ -\frac{\hbar^2}{2m} \nabla^2 + V(\mathbf{r}) + V_H(\mathbf{r}) + V_{xc}(\mathbf{r}) \right] \psi_i(\mathbf{r}) = \varepsilon_i \psi_i(\mathbf{r}) \quad (i = 1, 2, \dots, N), \quad (1.5)$$

where  $V$  and  $V_H$  are the known potentials which stem from electron-nucleus and electron-electron interactions, respectively.  $V_{xc}$  is the potential stemming from the exchange-correlation of a single electron.

The first three terms are due to the electron kinetic energy, electron-nuclei Coulomb interaction, and electron-electron Coulomb interaction. These three are known from the original SE. The fourth term explains all left-over undefined contributions. This is the exchange correlation term, and its form is the largest ambiguity in this theorem. However, many approximation methods have been introduced; for example, the local density approximation (LDA), generalized gradient approximation (GGA), etc. Finally, in practice, this Kohn-Sham equation (1.5) is solved with an initial guessed electron density function using the self-consistent method.

In DFT calculations, there are two widely-used approaches to simulate a solid surface. One approach uses a non-periodic cluster structure and localized wave functions (Figure 1.3a). This approach has been developed to simulate isolated molecules or atoms, but it can be used to simulate a surface as well. The other approach uses a periodic structure and plane-wave functions (Figure 1.3b). This method provides a more accurate representation of the structure of the solid surface. However, it does not provide a good answer when searching for transition states in comparison to the former method, especially within a reasonable computation time. Thus, in this dissertation, we use both models to calculate the structures and energies of ground and transition states.

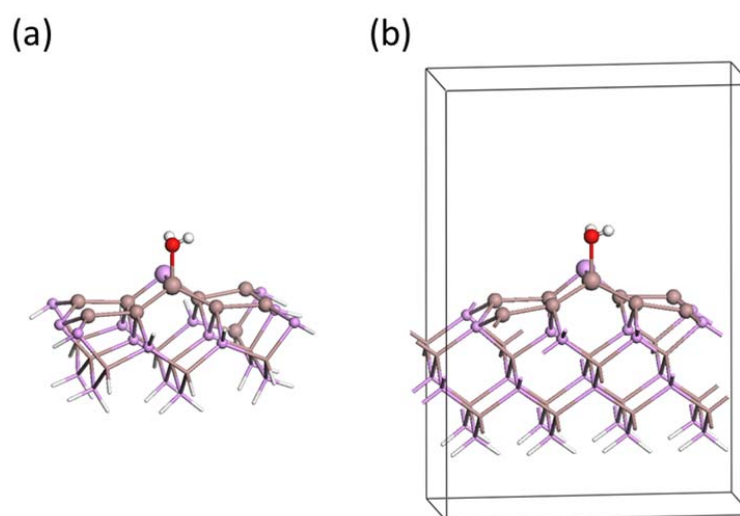


**Figure 1.3** a) A cluster and b) periodic model structures of a water molecule adsorbed on the GaP(001)(2×4) mixed-dimer surface. The unit cell structure enclosed in the black line boundaries in b) build a periodic boundary condition in an actual simulation. Purple, brown, red, and white spheres/rods represent P, Ga, O, and H atoms, respectively.

### 1.3 Summary

As the size regime of interest in semiconductor research decreases, molecular level understanding of the structure, chemistry, electronics, and energetics of adsorbates on III-V semiconductor surfaces becomes very important. The combination of STM, XPS, and DFT enables one to study the molecule/III-V semiconductor system in great detail.

This dissertation is composed of three original pieces of research which deal with three example systems, including organic and inorganic materials adsorbed on clean GaAs and GaP(001) surfaces. We investigated the structure, chemistry, energetics, and electronics of the example systems using scanning tunneling microscopy, X-ray photoelectron spectroscopy, and density functional theory calculation.

Chapter 2 is a study of the  $Zn_3P_2$  epitaxial film grown on the Ga-rich GaAs(001)(6×6) surface. The purpose of this study is to thoroughly understand the film growth mechanism and the electronic and geometric properties of the  $Zn_3P_2$ /GaAs(001) system. We discovered that a P-rich

amorphous layer covers the crystalline  $Zn_3P_2$  film during and after growth. We also describe an accurate picture of the structural and electronic properties of the GaP interface between  $Zn_3P_2$  and GaAs.

Chapter 3 is a DFT study of water-induced oxidation of the Ga-rich GaP(001)(2×4) surface. This chapter elucidates structural and energetic information of every step in the gaseous water-induced GaP oxidation reactions, at the atomic level, in great detail. We explored all reasonable ground states involved in most of the possible adsorption and decomposition pathways using DFT simulations.

Chapter 4 comprises high resolution STM, XPS, and DFT studies of adsorption structures and thermal decomposition pathways of 1-propanethiol on the Ga-rich GaP(001)(2×4) surface. We elucidated adsorption locations and structures of a single molecule on the surface as a function of annealing temperature. We also used DFT calculations to determine the energetics of ground states and to find relevant transition states. The chemical bonding nature and coverage variation of the system was studied with XPS.

## *Chapter 2*

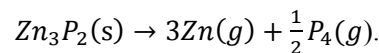
# Growth Mechanism and Electronic Structure of Zn<sub>3</sub>P<sub>2</sub> on a Ga-Rich GaAs(001) Surface

## 2.1 Introduction

Zinc phosphide (Zn<sub>3</sub>P<sub>2</sub>) is a novel photovoltaic (PV) material with a direct band gap of 1.50 eV, a long minority-carrier diffusion length, and strong light absorption in the visible region.[16-18] In addition, the terrestrial abundance of its constituent elements attracts additional attention due to the recent interest in developing high-efficiency PV devices using earth-abundant materials.[19] The superior absorption and other advanced optoelectronic properties of Zn<sub>3</sub>P<sub>2</sub> make it an appropriate light absorber for earth-abundant solar applications.

The growth of high-quality, thin-film Zn<sub>3</sub>P<sub>2</sub> for PV applications has been attempted using a variety of growth techniques such as vacuum deposition, ionized-cluster beam deposition, vapor phase deposition, and hot wall deposition.[20-24] However, these techniques typically produced polycrystalline Zn<sub>3</sub>P<sub>2</sub> films without the necessary electronic material quality for efficient photovoltaic application.

In order to enhance the material quality of Zn<sub>3</sub>P<sub>2</sub> thin films, other growth techniques have been reported, including metal organic vapor phase epitaxy (MOCVD) [25, 26] and molecular-beam epitaxy (MBE).[27] Epitaxial Zn<sub>3</sub>P<sub>2</sub> films were also grown using a compound-source MBE technique, [28] which is possible because Zn<sub>3</sub>P<sub>2</sub> sublimes congruently as follows: [29]



The compound source MBE technique was not only simpler due to the reduced number of sources required, but produced films with excellent crystalline quality. However, the detailed

chemistry, mechanism, and geometric/electronic structures of this growth process have yet to be thoroughly explored. Understanding the surface and interface properties of a  $\text{Zn}_3\text{P}_2$  epilayer has important implications on device fabrication and performance. Knowledge of the atomic structure of the epitaxial  $\text{Zn}_3\text{P}_2$  surface plays a significant role in additional processing steps; for example, the growth of additional epilayers, design of surface passivation/window layers, and functionalization/modification of the surface with chemical species. In addition, understanding the reaction chemistry and electronic properties at the interface between  $\text{Zn}_3\text{P}_2$  and the GaAs substrate significantly contributes to developing functional heterojunction devices.

In this chapter, we report the detailed chemical, structural, and electronic properties of the surface and interface of pseudomorphic  $\text{Zn}_3\text{P}_2$  epilayers grown on the GaAs(001) surface. Scanning tunneling microscopy (STM) and high-resolution x-ray photoelectron spectroscopy (XPS) were employed to elucidate the geometric and electronic structure of the  $\text{Zn}_3\text{P}_2$  films at the initial growth stages under various conditions. Additionally, high-resolution x-ray diffraction (HRXRD) and transmission electron microscopy (TEM) were used to verify the crystallinity and orientation of the as-grown films. The energy-band alignment of the  $\text{Zn}_3\text{P}_2$  epilayer with respect to the GaAs substrate was determined based on thickness-dependent XPS measurements. Finally, the formation of a thin GaP layer at the interface between  $\text{Zn}_3\text{P}_2$  and GaAs was corroborated by scanning tunneling spectroscopy (STS), XPS, and TEM data, as well as density functional theory (DFT) simulations. The impact of the observed morphological and electronic properties of the  $\text{Zn}_3\text{P}_2/\text{GaAs}$  interface on the construction of  $\text{Zn}_3\text{P}_2$  solar cells is discussed.

## 2.2. Experimental and computational details

The growth of  $\text{Zn}_3\text{P}_2$  epilayers on the Ga-rich GaAs(001) substrate was carried out in an ultra-high vacuum (UHV) molecular beam epitaxy (MBE) chamber (base pressure,  $< 1 \times 10^{-10}$  Torr). We used n-type GaAs(001) single crystal wafers (carrier concentration  $\sim 1 \times 10^{18} \text{ cm}^{-2}$ , AXT Inc.) as epitaxial substrates. The surface of the substrate was cleaned by several cycles of  $\text{Ne}^+$  ion bombardment (500 eV) and annealing (530 °C) in the UHV chamber. A Ga-rich GaAs(001)-(6×6) surface reconstruction was reliably obtained, which was verified by STM.[30-32]. The well-defined surface structure at the atomic level keeps the surface structure and stoichiometry constant for all  $\text{Zn}_3\text{P}_2$  growth. In addition, the (6×6) surface does not contain excess Ga droplets, which results in an increase of the surface Ga/As ratio compared with the mathematically obtained Ga/As ratio of the

(6×6) reconstruction.  $\text{Zn}_3\text{P}_2$  epilayers were grown on the clean well-defined (6×6) surface at normal growth temperature (180 °C) and various high temperatures ( $\geq 300$  °C) using the compound source MBE technique.[28] The  $\text{Zn}_3\text{P}_2$  flux was maintained by applying a constant power on the  $\text{Zn}_3\text{P}_2$ -loaded effusion cell, which gave an effusion cell temperature of 420 °C and a chamber background pressure of around  $1 \times 10^{-9}$  Torr. We expect the pressure of the source beam to be around two orders of magnitude higher than the measured pressure due to the position of the nude ion gauge. Every  $\text{Zn}_3\text{P}_2/\text{GaAs}(001)$  sample was prepared by one-time deposition, and the amount of deposition was only controlled by time. This procedure prevents intermittence in the deposition, which potentially generates chemical inhomogeneity inside the epilayer. The amount of  $\text{Zn}_3\text{P}_2$  deposition is expressed in Langmuir (1 Langmuir (L) =  $1 \times 10^{-6}$  Torr · 1 sec). Based on TEM images of  $\text{Zn}_3\text{P}_2/\text{GaAs}(001)$  samples grown by the procedure above, the growth rate was estimated to be less than 0.1 nm per minute.

The scanning tunneling microscopy (STM) and tunneling spectroscopy characterizations were carried out in a separate UHV chamber (base pressure,  $< 3 \times 10^{-11}$  Torr) which was connected to the MBE chamber; thus, the as-grown sample was transferred from the MBE chamber to the STM chamber under UHV. The analysis of the surface topography was carried out using a commercial STM (VT-STM XA, Omicron Nanotechnology). The filled-state STM images were obtained in the constant current mode with a sample bias voltage between  $-2.5$  V and  $-3.0$  V, and set-point current of 100 pA. The tunneling spectra (tunneling current versus sample bias voltage curve; I-V curve) were acquired from a given feature on the STM images at a fixed sample-to-tip distance, which was defined by fixing the bias voltage at  $-2.5$  V and set-point current at 100 pA. A number of I-V curves from the same feature are averaged, and the  $dI/dV$  curves were obtained by differentiating the I-V curves. All STM and tunneling spectroscopy data were taken at room temperature after cooling down the as-grown  $\text{Zn}_3\text{P}_2/\text{GaAs}(001)$  films in the STM chamber.

X-ray photoelectron spectroscopy (XPS) measurements were carried out in a separate UHV chamber (base pressure,  $< 3 \times 10^{-9}$  Torr) where a Kratos Ultra DLD spectrometer and monochromatic Al  $K\alpha$  radiation ( $h\nu = 1486.58$  eV) were installed. The  $\text{Zn}_3\text{P}_2/\text{GaAs}(001)$  samples were transferred from the MBE chamber to the XPS chamber in a portable stainless steel chamber filled with anhydrous nitrogen gas. Thus, the sample was not exposed to ambient gas during transportation. High-resolution spectra were collected at a fixed analyzer pass energy of 20 eV.

The spectra were collected at  $0^\circ$  with respect to the surface normal direction. The binding energy was referenced to the instrument Fermi level which was calibrated using the Au  $4f_{7/2}$  level (84.00 eV) of a clean gold surface. The XPS data were analyzed with commercial software, CasaXPS (version 2.3.16). The individual peaks were fitted by a Gaussian/Lorentzian function after Shirley type background subtraction. Spin-orbit splittings and branching ratios were held constant; 865 meV and 0.5 for P  $2p$  core level and 701 meV and 0.666 for As  $3d$  core level, respectively.

Density functional theory (DFT) calculations were carried out using the flavor of Perdew-Burke-Ernzerhof (PBE) exchange-correlation functional. These calculations replaced the Ar core of Ga, the Ne core of P, and the He core of O with projected augmented-wave (PAW) potentials optimized for the PBE functionals. Thus Ga is described with three valence electrons, P with five, and O with six. All calculations were performed using the Vienna Ab-initio Simulation Package (VASP). The electronic wave functions were expanded in a plane-wave basis set using a cutoff energy of 380 eV, and the reciprocal space was sampled using k points generated by  $4 \times 2 \times 1$  Monkhorst-Pack scheme. The convergence criteria for electronic and ionic optimization were set to  $1 \times 10^{-4}$  and  $1 \times 10^{-3}$  eV, respectively.

The lattice parameters for the slab calculation were determined from the separate calculation of bulk GaAs, for which the cubic lattice constant is optimized as 5.75 Å. The Ga-rich GaAs(001)- $\beta 2(2 \times 4)$  surface was modeled using a periodic slab geometry composing of eight Ga and nine As layers with a vacuum region equivalent to eight Ga and As layers, resulting in the composition of the simulation cell being 30 Ga and 35 As atoms. All atomic positions were optimized except the bottom two Ga and As layers, which were fixed. The bottom As layer was passivated with  $0.75e^-$  pseudo-hydrogen atoms to avoid any possible artificial electrostatic force due to spurious charge separation.[33]

Energetics of the anion replacement reactions are discussed in this report. In order to compare the stabilities of the alloy systems, which contain different numbers of constituent atoms, we calculate the surface formation energy, [34]

$$E_{surf} = \frac{1}{A} [E(mnl) - m\mu(Ga) - n\mu(As) - l\mu(P)]. \quad (2.1)$$

$A$  is area of the surface model of interest (for our  $(2 \times 4)$  superstructure model,  $A = 8$ ).

$m$ ,  $n$ , and  $l$  represent the number of Ga, As, and P atoms in a surface model, respectively.  $E(mnl)$  is the calculated total energy of the surface model at 0 K using the method described above.  $\mu(X)$  is the chemical potential of element X in the alloy. The chemical potentials of P and As atoms are restricted by the following equations:

$$\Delta\mu(P) = \mu(P) - \mu(P^{bulk}), (\Delta H_f(GaP) \leq \Delta\mu(P) \leq 0), \quad (2.2)$$

$$\Delta\mu(As) = \mu(As) - \mu(As^{bulk}), (\Delta H_f(GaAs) \leq \Delta\mu(As) \leq 0). \quad (2.3)$$

We are interested in the relative stability of a certain surface model with respect to the reference surface model, which is set to the GaAs(001)- $\beta 2(2 \times 4)$  reconstruction in this report. Thus, the equation (2.1) is modified to obtain the relative surface formation energy ( $\Delta E_{surf}$ ) as follows:

$$\Delta E_{surf} = \frac{1}{A} [E(mnl) - E_{ref}(m' n' l') + \mu(Ga)(m' - m) + \mu(As)(n' - n) + \mu(P)(l' - l)], \quad (2.4)$$

where  $m'$ ,  $n'$ ,  $l'$  represent the number of Ga, As, and P atoms in the reference surface model. In Equation (2.4), the number of the Ga atoms for the anion replacement reaction is fixed ( $m' - m = 0$ ). In the anion replacement reaction where As is replaced by P, the total number of As plus P is maintained ( $n + l = n' + l'$ ). These limiting conditions are applied to Equation (2.4), and then we obtain,

$$\Delta E_{surf} = \frac{1}{A} \{E(mnl) - E_{ref}(m' n' l') + (l' - l)[\mu(P^{bulk}) - \mu(As^{bulk}) + \Delta\mu(P) - \Delta\mu(As)]\}. \quad (2.5)$$

The bulk chemical potentials of P and As are calculated using the black P and crystalline As bulk structures with the same DFT methods described above; ( $\mu(P^{bulk}) = -5.27575$  eV and  $\mu(As^{bulk}) = -4.25974$  eV).[35, 36]

## 2.3. Scanning tunneling microscopy

Figure 2.1 shows STM images of the  $Zn_3P_2$  epilayers grown on the Ga-rich GaAs(001)-(6×6) surface with various  $Zn_3P_2$  coverages maintaining the substrate temperature at 180 °C. The inset in Figure 2.1a (also refer to Figure 2.4a) shows a high resolution STM image of the GaAs(001)-(6×6) reconstruction. Each red protrusion at high topographic location along the surface normal direction is attributed to the As atom of the first atomic layer Ga-As or As-As dimer. The As atom of the Ga-As dimer has one dangling bond which protrudes out of the surface and is seen as a single bright dot in the STM image, and the two neighboring As atoms on the As-As dimer are seen as a peanut-shaped feature. The array of these Ga-As or As-As dimers along the  $[-110]$  direction forms a Ga-As or As-As dimer row on the first atomic layer. The atoms in the blue area between the red dimer rows are located in the second and third atomic layers from the top. There are zig-zag features in light blue which are associated with As atoms of the Ga-As dimers on the layer. The Ga-As or As-As dimer rows in the first layer and the zig-zag features in the second and third layer are signatures of the (6×6) reconstruction in an STM image.[30, 31] The grey STM image in Figure 2.1a shows not only the large-scale picture of atomic steps and terraces but also the small-scale Ga-As or As-As dimer rows running along the  $[-110]$  direction. The density and distribution of the steps and terraces are typical of the GaAs surface after inertion sputter cleaning procedures.

Upon exposure of the clean (6×6) surface to a small quantity of  $Zn_3P_2$  ( $\leq 0.2$  L; 1 Langmuir (L) =  $1 \times 10^{-6}$  Torr · 1 sec), the surface showed bright protrusions at random locations in addition to the clean (6×6) features (Figure 2.1b and c). The size and density of the protrusions increased with increasing deposition amount and were therefore assumed to be  $Zn_3P_2$  nucleation points, or seeds. For epitaxy on the (001) face following the island growth mechanism,[37] the islands are usually seen as square or rectangular shapes at the initial growth stage due to the continuity of bond symmetry between the epilayer and substrate. [30, 38] The shapes and sizes of the seeds or islands in our  $Zn_3P_2$  film are irregular and featureless. In addition, STM images collected at higher  $Zn_3P_2$  exposures (Figures 2.1d and 1e) show that the islands do not grow to form bigger islands or films, but instead the number density of the islands increases. The height of the islands had a wide distribution and did not exhibit discrete multiples of an atomic step size of  $Zn_3P_2$ .

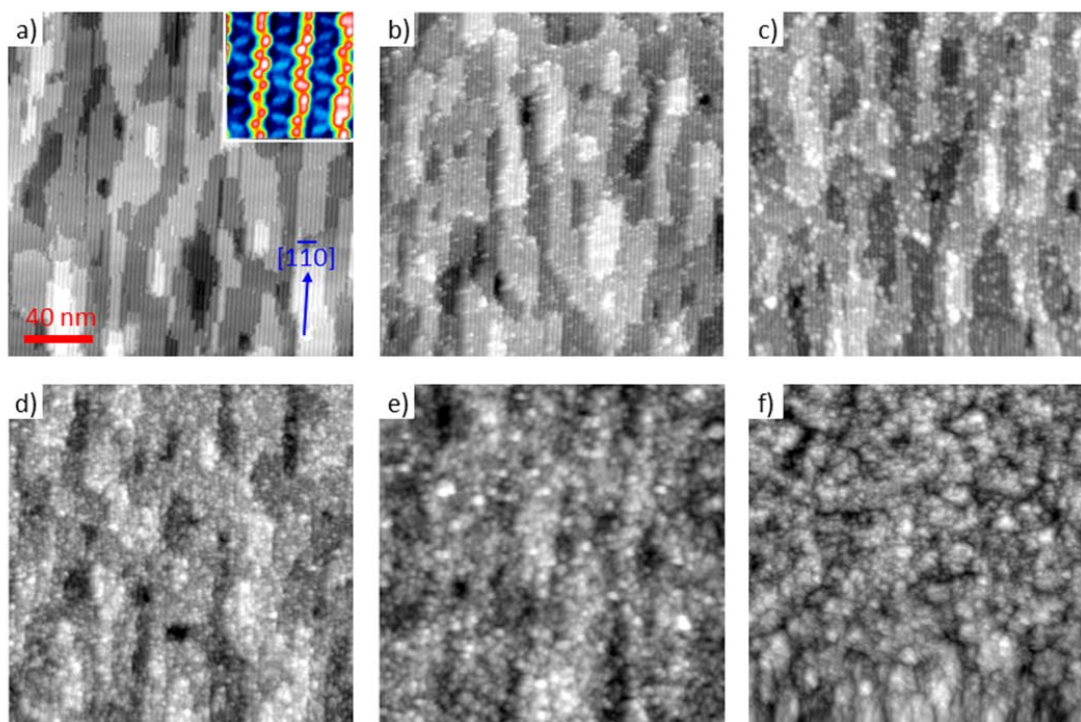


**Figure 2.1** STM topography images of a) clean GaAs(001)-(6×6) and Zn<sub>3</sub>P<sub>2</sub>/GaAs(001) with various amounts of deposition; b) 0.05 L, c) 0.2 L, d) 0.63 L, e) 0.95 L, and f) 3.4 L at the same substrate temperature of 180 °C. The image size of the inset of a) is 8 nm<sup>2</sup>.

In order to check whether the Zn<sub>3</sub>P<sub>2</sub> epilayer was crystalline, HRXRD patterns and TEM images of the Zn<sub>3</sub>P<sub>2</sub>/GaAs samples were collected as shown in Figures 2.2 and 2.3. Surprisingly, the HRXRD and TEM data clearly demonstrated that the Zn<sub>3</sub>P<sub>2</sub> films were crystalline and pseudomorphic in nature with growth occurring along the (001) direction of the tetragonal Zn<sub>3</sub>P<sub>2</sub> lattice. This indicates that the Zn<sub>3</sub>P<sub>2</sub> film must have a crystalline phase directly beneath the irregularly-shaped overlayer observed in the STM images. Figure 2.1f displays the STM image of a thick (a few nanometers) Zn<sub>3</sub>P<sub>2</sub> layer. We note that the irregular-shaped surface features observed in the STM images are not associated with artifacts due to a blunt or molecule-coated tip. Clear, single-atom-sized protrusions were clearly observed in high-magnification STM images of the irregular surface, but atomic lattice features could not be identified. Such a featureless topography even in high resolution STM images is very similar to those observed for an amorphous phase. [39]

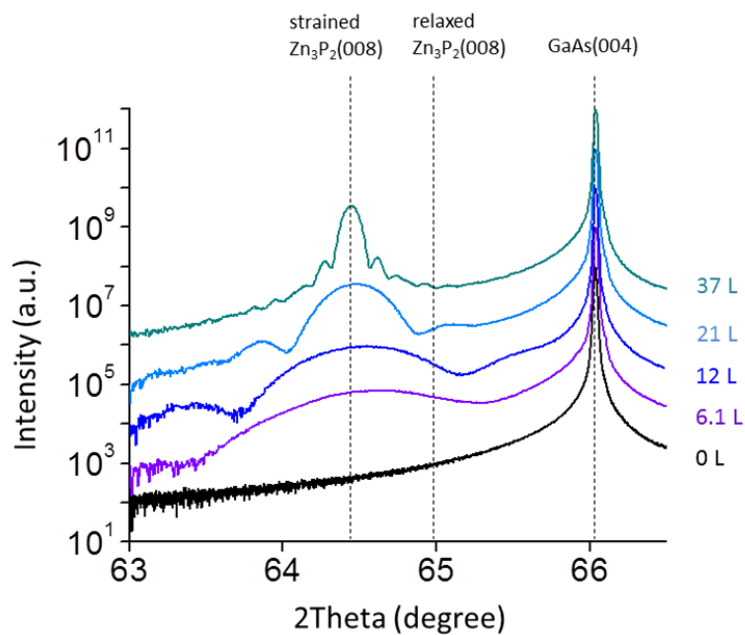


**Figure 2.2** Symmetric HRXRD scans of the Zn<sub>3</sub>P<sub>2</sub>/GaAs(001) with Zn<sub>3</sub>P<sub>2</sub> deposition amounts of 0, 6.1, 12, 21, and 37 L. Vertical dashed lines indicate the diffraction peak positions of pseudomorphic epitaxy Zn<sub>3</sub>P<sub>2</sub> (008), crystalline Zn<sub>3</sub>P<sub>2</sub> (008), and crystalline GaAs(004), respectively.

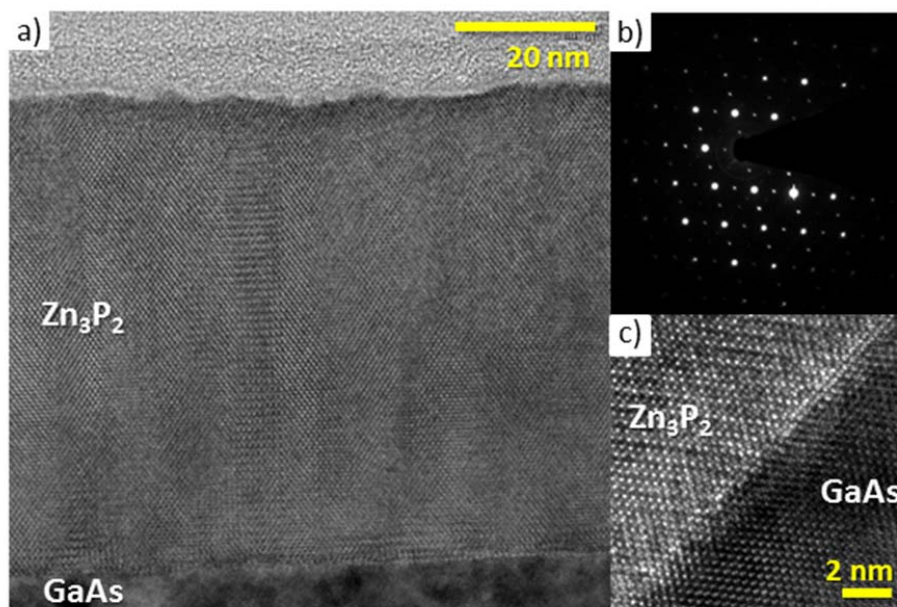


**Figure 2.3** a), c) TEM images of the Zn<sub>3</sub>P<sub>2</sub>/GaAs(001) with the Zn<sub>3</sub>P<sub>2</sub> deposition amount of 37L. b) SAED image of the Zn<sub>3</sub>P<sub>2</sub>/GaAs(001).

Figure 2.4 shows high-resolution STM images (top), cross-sectional line profiles (center), and proposed structure models (bottom) of a clean GaAs(001)-(6×6) surface and sub-monolayer Zn<sub>3</sub>P<sub>2</sub> layers grown on the clean (6×6) surface at high temperatures (300, 490, and 560 °C). XPS data showed that the films grown at temperature higher than 400 °C did not contain Zn, which is supported by previous reports where Zn desorption occurs below 323 °C, depending on the coverage and surface properties.[40, 41] Thus, we expect that the films grown at high temperatures are effectively the same as those formed using only an elemental P<sub>4</sub> source. Figure 2.4a displays the clean GaAs(001)-(6×6) surface reconstruction. The cross-sectional line profile shows the lateral distance along [110] direction between two neighboring Ga-As or As-As dimer rows is six times larger than the dimension of the surface unit cell. In the structure model, the first-layer Ga-As or As-As dimer sits on top of the (1×2) Ga rectangle composed of the six, second-layer Ga atoms shown in the blue rectangle in Figure 2.4a. On the (1×2) Ga rectangle, there are two locations on which a Ga-As or As-As dimer can occupy. Sometimes, both of locations are occupied with Ga-As or As-As dimers – seen as a double peanut-shaped feature (red arrow in Figure 2.4a). However, in most cases, only one of the two locations is occupied by a Ga-As or As-As dimer.

When 0.14 L of Zn<sub>3</sub>P<sub>2</sub> was deposited on the clean (6×6) surface at 300 °C, the number of double peanut-shaped features increased on the first-layer dimer rows (Figure 2.4b). Since the peanut-shaped feature was also observed on the films grown at higher temperature than the Zn desorption temperature, Zn was not associated with this feature. In addition, since Zn and Ga are electron-deficient species in Zn<sub>3</sub>P<sub>2</sub> and GaAs, the atoms in the STM images recorded at the negative sample voltage were expected to be darker than the group-V anion. Finally, upon exposure of the clean (6×6) surface to a P source, any additional feature whose number density increases as the amount of P exposure increases was associated with P atoms. Thus, the double peanut-shaped feature was attributed to As-As, As-P, or P-P dimers. In Figure 2.4b, there is a slight contrast difference within a dimer or between dimers. This may have resulted from the difference in atomic radii of As and P. However, it was difficult to discretely assign As and P positions based on the STM images since the contrast difference may also have resulted from dimer buckling or a geometric and/or electronic effect caused by the replacement of Ga or Zn atoms by As or P atoms underneath the dimer.

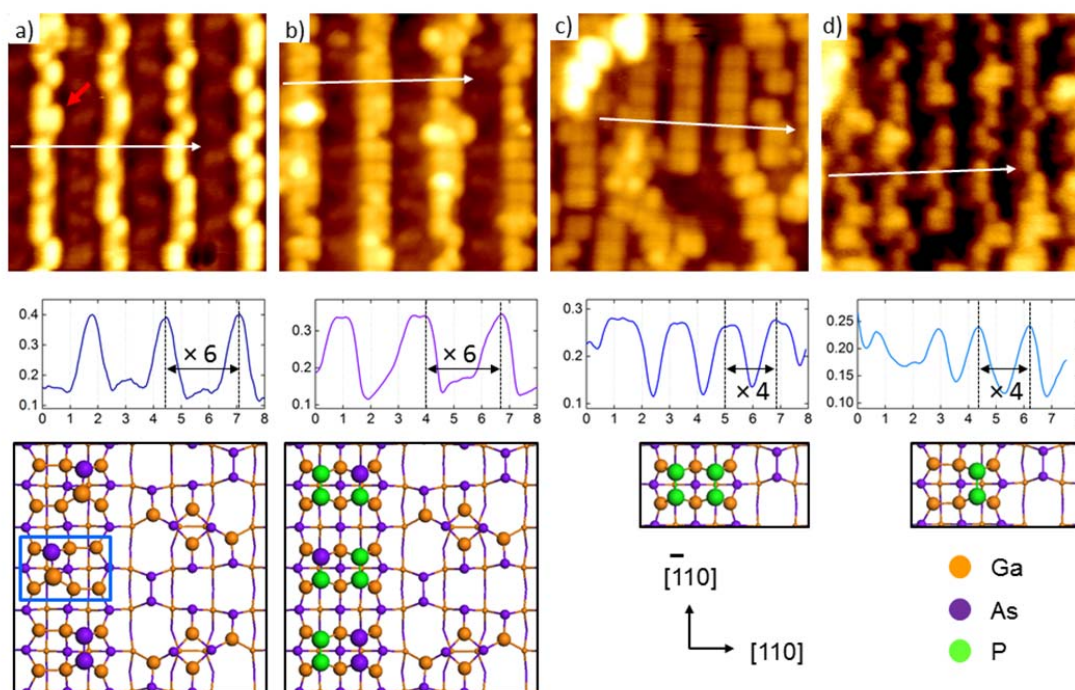


**Figure 2.4** STM topography images (size  $10 \text{ nm}^2$ ), cross section line profiles, and proposed structure models of  $\text{Zn}_3\text{P}_2/\text{GaAs}(001)$  grown at different conditions; a) clean  $\text{GaAs}(001)$ - $(6 \times 6)$ , b)  $0.14 \text{ L}$  at  $300 \text{ }^\circ\text{C}$ , c)  $3.7 \text{ L}$  at  $490 \text{ }^\circ\text{C}$ , and d)  $3 \text{ L}$  at  $560 \text{ }^\circ\text{C}$ . The red arrow and blue rectangle in column a) indicate double As-As dimers in the first layer and a  $(1 \times 2)$  Ga rectangle in the second layer, respectively.

Figure 2.4c displays the  $\text{GaAs}$  surface where  $3.7 \text{ L}$  of  $\text{Zn}_3\text{P}_2$  was deposited at  $490 \text{ }^\circ\text{C}$ . Interestingly, the inter-dimer row distance along the  $[110]$  direction was decreased from  $\times 6$  to  $\times 4$  while maintaining the double peanut-shaped feature. The growth temperature of  $490 \text{ }^\circ\text{C}$  is the temperature at which desorption of As from  $\text{GaAs}(001)$ - $(2 \times 4)$  [42] and formation of the  $\text{GaP}(001)$ - $\beta 2(2 \times 4)$  surface reconstruction was observed.[43] Thus, persistence of the double peanut-shaped feature is attributed to replacement of As by P to form P-P dimer rows on the  $\text{GaP}(001)$ - $\beta 2(2 \times 4)$  reconstruction. Among the stable  $\text{GaP}(001)$  surface reconstructions, the symmetry and shape of the double peanut-shaped P-P dimer rows with  $(2 \times 4)$  symmetry is characteristics of the  $\text{GaP}(001)$ - $\beta 2(2 \times 4)$  reconstruction. [44]

Finally, we exposed the  $\text{GaAs}(001)$  surface to  $\text{Zn}_3\text{P}_2$  flux at  $560 \text{ }^\circ\text{C}$  (Figure 2.4d). Most of the dimer rows are composed of single peanut-shaped features in a  $(2 \times 4)$  unit cell. The line

profile shows the inter-dimer row distance has  $\times 4$  symmetry. Among the GaP(001)-(2 $\times$ 4) reconstructions, which are both theoretically stable and experimentally observable, [45] the single peanut-shaped feature with the (2 $\times$ 4) symmetry is associated with GaP(001)- $\delta$ (2 $\times$ 4). The transition from  $\beta 2$  to  $\delta$  phase under group-V overpressure at high temperature has been also observed by STM in a similar system. [46]

## 2.4. Scanning tunneling spectroscopy

The three curves in Figure 2.5a are tunneling spectra (tunneling current versus sample bias voltage curves; I-V curves) obtained from the (i) first-layer Ga-As or As-As dimer on the clean GaAs(001)-(6 $\times$ 6) surface (black), (ii) the first-layer P-P, P-As, or As-As dimer on the 3.7 L Zn<sub>3</sub>P<sub>2</sub>/GaAs(001) epilayer grown at 490 °C (red), and (iii) an arbitrary feature on the 13 L Zn<sub>3</sub>P<sub>2</sub>/GaAs(001) epilayer grown at 180 °C (blue), respectively. For the last sample, there is no periodic feature on the surface as shown in Figure 2.1f. Therefore, the tunneling spectra were collected from arbitrary locations on the surface. A substantial number of I-V curves were collected from each surface, averaged, and then derived to produce dI/dV curves. The dI/dV from tunneling spectroscopy is proportional to the local density of states at the surface.[47] The positions of the valence-band maximum and conduction-band minimum for each surface were determined by linear extrapolation of the leading edges of the dI/dV curve. The apparent band gaps, which were calculated as the difference between valence-band and conduction-band edges, are also displayed in Figure 2.5b-d.

The apparent band gap of 1.38 eV collected for the clean GaAs(001)-(6 $\times$ 6) surface is in excellent agreement with the known GaAs bulk band gap of 1.42 eV (Figure 2.5b). In addition, since the Fermi level ( $V_{\text{sample}} = 0$ ) is located in the middle of the band gap in spite of high n-doping level ( $N_d \sim 1 \times 10^{18} / \text{cm}^2$ ), the (6 $\times$ 6) surface prepared by the inert-ion sputtering annealing method in this study demonstrated Fermi level pinning. Based on the literature, Fermi level pinning is strongly dependent on the surface structure and defects which are influenced by the surface preparation method, the type of reconstruction, the type and density of defects, etc. Therefore, there are often contradictory results among different studies in which the Fermi level is observed to be pinned and unpinned for a given surface reconstruction.[48, 49] In addition, the electron counting model itself cannot explain Fermi level pinning on the (6 $\times$ 6) surface because

there are a number of variations in the type and location of the first-layer Ga and As atoms.[50] For instance, the electron counting model works when the first-layer atoms consist of three dimers with four As and two Ga in the (6×6) surface; however, the surface structures observed in STM images deviate a great deal from this fixed composition.

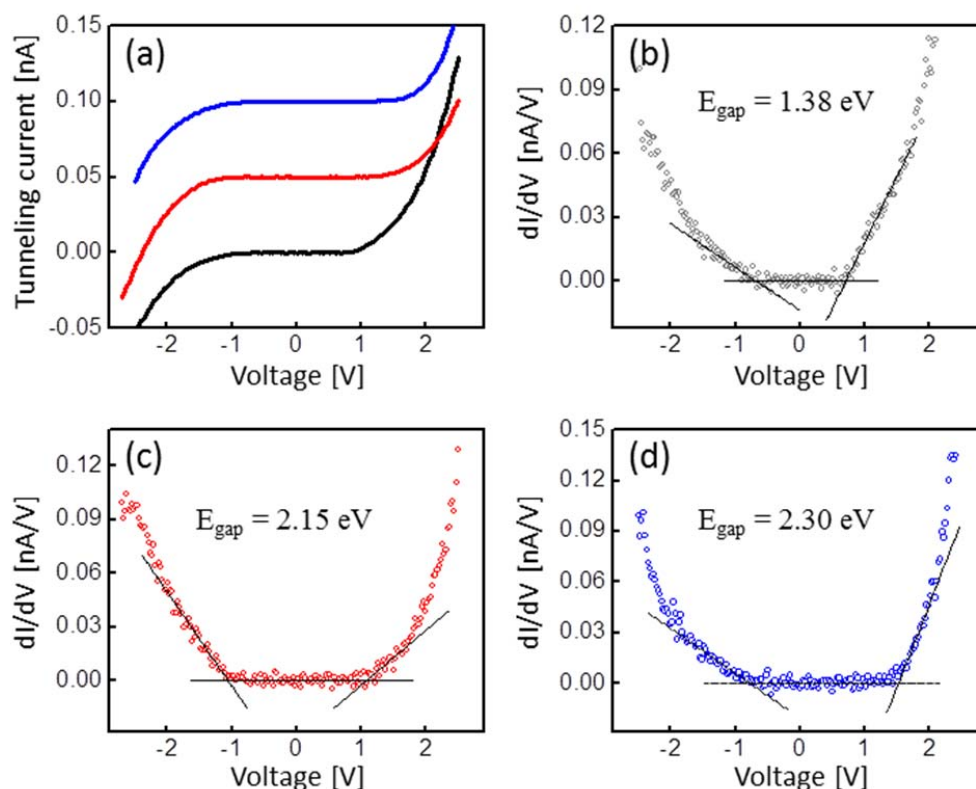


**Figure 2.5** a) Tunneling current versus sample voltage (I-V) spectra obtained from clean GaAs(001)-(6×6) [black], 3.7 L Zn<sub>3</sub>P<sub>2</sub>/GaAs(001) at 490 °C [red], and 13 L Zn<sub>3</sub>P<sub>2</sub>/GaAs(001) at 180 °C [blue]. b)-d) The dI/dV versus V curve of each I-V spectrum in a). The black lines in b)-d) indicate the linear extrapolation curves of the leading edges of the dI/dV versus V curves. The number displayed above the dI/dV curve is the apparent band gap.

Exposure of the clean surface to Zn<sub>3</sub>P<sub>2</sub> flux caused substantial changes in the observed tunneling spectra. The dI/dV obtained from Zn<sub>3</sub>P<sub>2</sub>/GaAs(001) grown at 490 °C displayed an apparent band gap of 2.15 eV and evidence of Fermi level pinning at the mid gap (Figure 2.5c). The band gap is significantly different from the known crystalline Zn<sub>3</sub>P<sub>2</sub> band gap of 1.5 eV.[16, 28] Instead, the large band gap on this surface is close to the known band gap of GaP of 2.26 eV.

Therefore, tunneling spectroscopy supports the formation of the GaP layer on the surface of the GaAs(001) when exposed to  $Zn_3P_2$  at high temperatures.

Finally, the tunneling spectra obtained from  $Zn_3P_2$ /GaAs(001) grown at 180 °C (Figure 2.5d) demonstrated an apparent band gap of 2.30 eV which is again significantly larger than the  $Zn_3P_2$  band gap. The larger apparent band gap is attributed to the surface overlayer phase composed of amorphous zinc phosphide ( $a-ZnP_x$ ) and elemental P. The band gap of  $ZnP_2$  of 1.44 ~ 2.60 eV [51] indicates that an increased P/Zn atomic ratio of  $Zn_xP_y$  is one of sources of the band gap increase. Thus, our STS data supports that the overlayer is composed of P-rich amorphous  $ZnP_x$  and/or elemental P. However, the position of the Fermi level close to the valence-band edge indicates p-type doping, which is consistent with previous reports.[28]

## 2.5. X-ray photoelectron spectroscopy

Figure 2.6 shows the fitted X-ray photoelectron spectra of the P  $2p$  core level collected on  $Zn_3P_2$  epilayers grown at various surface coverages and temperatures. The  $Zn_3P_2$  epilayers in Figure 2.6a and b are grown at 180 °C (normal growth temperature). The P  $2p$  region is fitted with three discrete bonding states: (1) a crystalline  $Zn_3P_2$  state ( $c-Zn_3P_2$ ), (2) a P-rich  $a-ZnP_x$  state, ( $x > 1$ ; + 0.55 eV versus  $c-Zn_3P_2$ ), and (3) an elemental P state (+ 1.4 eV versus  $c-Zn_3P_2$ ). The  $a-ZnP_x$  state exists throughout all  $Zn_3P_2$  coverages as shown in the coverage dependent XPS data in Figure 2.7a. We note that the full width at half maximum (FWHM) of the  $a-ZnP_x$  peak at  $\leq 1.1$  L is 30% larger than ones at  $\geq 2.1$  L. This is due to the existence of a GaP bonding state (+ 0.7 eV versus  $c-Zn_3P_2$ ) at  $\leq 1.1$  L with a slightly higher binding energy shift than the  $a-ZnP_x$  phase. We will discuss the GaP bonding state later. The core-level binding energy shift of + 0.55 eV in the  $a-ZnP_x$  phase is likely due to disordered bonding which includes P-P and Zn-Zn bonds. The existence of the disordered bonding (around 25 %) has been demonstrated in the amorphous III-V system.[52] The P atom in the crystalline  $Zn_3P_2$  has four or six bonds with the neighboring Zn atoms. Since Zn has a lower electronegativity than P, the formation of P-P rather than P-Zn on P in the  $a-ZnP_x$  overlayer shifts the P  $2p$  core-level binding energy to a higher value. The STM and tunneling spectroscopy data also support the existence of the P-rich  $a-ZnP_x$  overlayer which has featureless surface morphology and larger apparent band gap than  $c-Zn_3P_2$ .

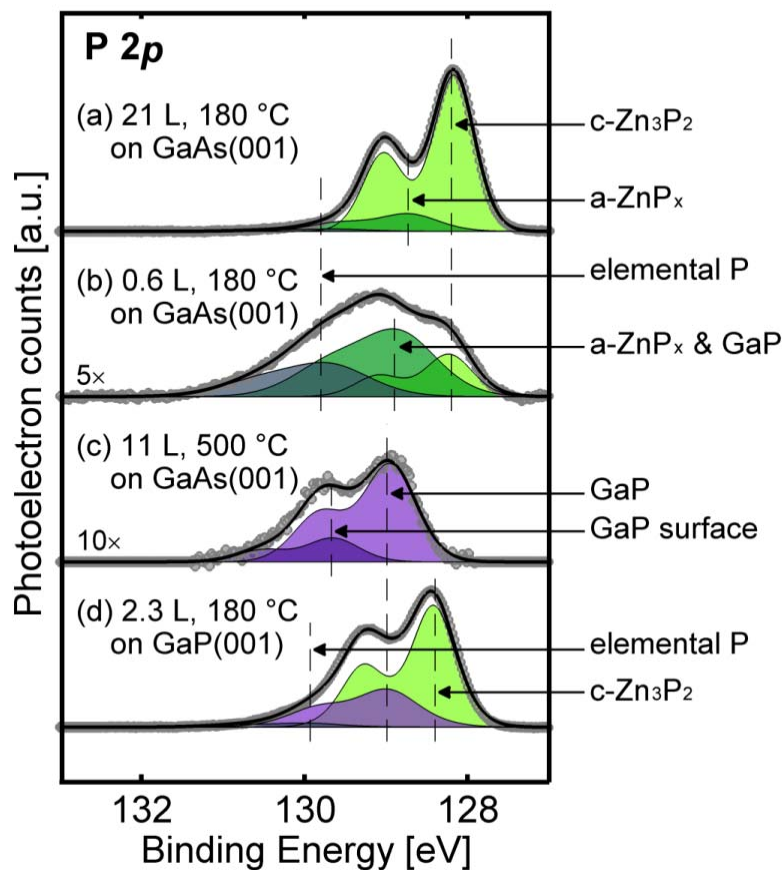


**Figure 2.6** P  $2p$  core-level X-ray photoelectron spectra of the  $\text{Zn}_3\text{P}_2$  film grown at various depositions and substrate temperatures. a) 21 L and b) 0.6 L  $\text{Zn}_3\text{P}_2$  grown on the Ga-rich GaAs(001)-(6 $\times$ 6) at 180 °C. c) 18 L  $\text{Zn}_3\text{P}_2$  grown on the Ga-rich GaAs(001)-(6 $\times$ 6) at 400 °C. d) 2.3 L  $\text{Zn}_3\text{P}_2$  grown on the Ga-rich GaP(001)(2 $\times$ 4) at 180 °C. Gray circles, black curves, and colorful curves represent raw data, sum of the fitted components, and each displayed component, respectively.

The third component with the highest binding energy shift of + 1.4 eV is due to an elemental P layer. The existence of the phase and the binding energy shift of the elemental P are evidenced from previous reports.[53, 54] Figure 2.6c shows the fitted photoelectron spectrum in the P  $2p$  region of the 11 L  $\text{Zn}_3\text{P}_2$  grown on GaAs(001) at 500 °C. The P  $2p$  region is fitted with two discrete components; a GaP state (+ 0.7 eV versus c- $\text{Zn}_3\text{P}_2$ ) and a GaP surface state (+ 1.3 eV versus c- $\text{Zn}_3\text{P}_2$ ). The assignment of the GaP bonding state is based on the P  $2p$  core-level binding energy of bulk GaP in literature.[55] The GaP surface state is associated with the P-P and As-P

dimers on the surface. The substrate in this experiment has a well-defined surface structure; that is, GaAs(001)-(6×6). The formation of a GaP interfacial layer is likely due to either the reaction of P with the Ga adatoms on the Ga-rich surface or anion replacement of subsurface As with P atoms prior to or during film growth. The coverage of the GaP layer in the Zn<sub>3</sub>P<sub>2</sub> grown on GaAs(001) over 300 °C does not exceed 1 ML (monolayer) based on our quantitative analysis of the XPS data, in spite of Zn<sub>3</sub>P<sub>2</sub> exposures as high as 18 L, which agrees with previous results. [56]

In order to verify the binding energy shift of the GaP phase with respect to the c-Zn<sub>3</sub>P<sub>2</sub> phase, photoelectron spectra were collected on Zn<sub>3</sub>P<sub>2</sub> films grown directly on a single crystal GaP(001) substrate. The surface of GaP(001) was prepared by inert-gas ion sputtering and annealing methods which produce a Ga-rich GaP(001)(2×4) surface. Figure 2.6d shows fitted photoelectron spectra of a P 2*p* region from a Zn<sub>3</sub>P<sub>2</sub> film grown on the Ga-rich GaP(001) at 180 °C. There are three components in this region: a crystalline Zn<sub>3</sub>P<sub>2</sub> state (c-Zn<sub>3</sub>P<sub>2</sub>), a GaP state (+ 0.5 eV versus c-Zn<sub>3</sub>P<sub>2</sub>), and an elemental P state (+ 1.3 eV versus c-Zn<sub>3</sub>P<sub>2</sub>). The binding energy of the GaP state in the Zn<sub>3</sub>P<sub>2</sub>/GaP(001) system is consistent with that of the GaP layer in the Zn<sub>3</sub>P<sub>2</sub> grown on GaAs(001) at 500 °C in Figure 2.6c. Thus, existence of the GaP state for interfaces grown at high temperatures is supported by both internal and external evidence. On the other hand, existence of the GaP interface at the normal growth temperature (180 °C) was difficult to substantiate with XPS data alone. This is because 1) the amount of P in the GaP layer was very small (≤ 1 ML) especially on the film grown at normal growth temperatures, and therefore difficult to observe and 2) the GaP binding energy shift of + 0.7 eV is too close to separate from the B.E. shift of + 0.55 eV of the a-ZnP<sub>x</sub> state. However, in the STM experiment, we observed P atoms adsorbed on top of the second-layer Ga atoms to form P-P or P-As dimers at initial coverages for both normal growth and high temperatures. In addition, the binding energy shift of the GaP layer in the Zn<sub>3</sub>P<sub>2</sub>/GaAs grown at high temperature is exactly matched by the known GaP binding energy. Thus, a thin GaP layer exists at the interfacial region between the Zn<sub>3</sub>P<sub>2</sub> epilayer and the GaAs(001) substrate. It is surprising that the GaP layer permits the growth of Zn<sub>3</sub>P<sub>2</sub> films that are pseudomorphic, indicating the GaP is itself strained to the in-plane GaAs native lattice constant.

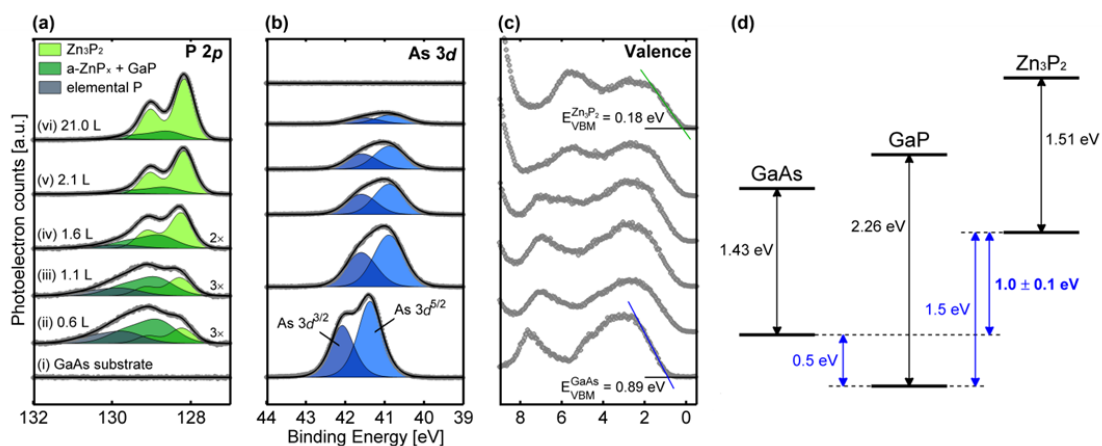


**Figure 2.7** Fitted X-ray photoelectron spectra of the a) P  $2p$  core level, b) As  $3d$  core level, and c) valence band region measured on  $\text{Zn}_3\text{P}_2/\text{GaAs}(001)$  heterojunction interfaces with increasing overlayer thickness. d) The energy-band alignment for an  $\text{Zn}_3\text{P}_2/\text{GaP}/\text{GaAs}(001)$  heterostructure.

XPS of the P  $2p$  core level, As  $3d$  core level, and valence-band region of  $\text{Zn}_3\text{P}_2(001)/\text{GaAs}(001)$  interfaces of increasing epilayer thickness are presented in Figure 2.7a-c. From the XPS data, the  $\text{Zn}_3\text{P}_2/\text{GaAs}$  valence-band discontinuity ( $\Delta E_V$ ) for the  $\text{Zn}_3\text{P}_2/\text{GaP}/\text{GaAs}(001)$  heterostructure was estimated using the method proposed by Kraut et al.[57] This procedure was previously used to determine the valence-band offsets for a series of epitaxial II-VI/ $\text{Zn}_3\text{P}_2$  heterojunctions.[58, 59] The offset calculation was supplemented by XPS measurements of  $\text{Zn}_3\text{P}_2$  epilayers grown directly on the  $\text{GaP}(001)$  surface under identical conditions. The measured band offsets for the system are displayed in Figure 2.7d. A value of  $\Delta E_V = 1.00$  eV was found for the  $\text{Zn}_3\text{P}_2/\text{GaAs}$  system. The  $\text{GaP}/\text{GaAs}$   $\Delta E_V$  of  $\sim 0.5$  eV was previously obtained from optical measurements on  $\text{GaP}-\text{GaAs}$  quantum well structures.[60] Therefore, assuming the transitivity of band discontinuities is valid for this material system results in a  $\text{Zn}_3\text{P}_2/\text{GaP}$   $\Delta E_V$  of  $\sim 1.5$  eV.

## 2.6. Density functional theory calculations

Our STM measurements indicated that exposure of the GaAs(001)-(6×6) to a Zn<sub>3</sub>P<sub>2</sub> overpressure caused the formation of a GaP(001)-β2(2×4) surface reconstruction at 490 °C. Tunneling spectroscopy and XPS data on the (2×4) surface showed the formation of a GaP layer with the P surface coverage limited to < 1 ML and with no Zn adsorption. Since there is no Zn, the transition from a (6×6) to a (2×4) symmetry is attributed to P adsorption which leads to the formation of one additional P-P or P-As dimer row per (6×6) surface unit cell. However, the additional P atoms can also incorporate into the subsurface layers in addition to surface adsorption. High growth temperatures of over 490 °C likely create favorable conditions to overcome the energy barrier of the subsurface anion replacement reaction.

To understand the energetics for the anion replacement of As by P on the surface and at the subsurface in the (2×4) reconstruction, we used density functional theory (DFT) calculations. A periodic supercell model was built and optimized to describe the GaAs(001)-β2(2×4) reconstruction, whose energy was set as the reference. We then studied the thermodynamics of the anion replacement reaction. Although it is helpful to simulate P adsorption and replacement reactions on all observed surface reconstructions, such as the (6×6), β2(2×4), and δ(2×4), the surface reconstruction was fixed to the β2(2×4) in this study.

In order to compare energies between the clean GaAs(001)-β2(2×4) and the P-replaced β2(2×4) structures and their dependence on the number of substitutions, the surface formation energy was calculated as a function of the P and As chemical potentials. Up to three As atoms were replaced by P atoms according to the following procedure. First, each As atom on the surface or in the subsurface (up to the 7<sup>th</sup> layer from the top) was replaced by a P atom followed by geometry optimization. Among the 28 possible cases for the P-replaced structures, P-replacement in the third-layer As atom under the center of the As dimer block in the first layer (Figure 2.8d) had the lowest energy. Substitution of the first- or third-layer As atom, which is exposed to the vacuum, for a P atom gave an energetically less favorable structure whose energy is 331 ~ 341 meV higher than the most stable P-replacement structure in the subsurface layer. The structure in Figure 2.8a shows the most stable surface P replacement among the six structures in which the surface As atoms in the first- or third-layer were replaced by P atoms. On the other hand, replacement of the third-layer As atom below the first-layer As dimer block is preferred

over that of the fifth-layer As atom by 95 ~ 153 meV. Thus, replacement of the third-layer As atom under the As dimer block is favored over that of either the surface or deep (below third layer) As atoms. After fixing the first P-replacement location, we searched for the second P-replacement position. The most stable structure including two P replacements is shown in Figure 2.8e. For the surface replacement, formation of a P-P dimer (Figure 2.8b) was energetically more favorable than two As-P dimers on the first-layer by 37 ~ 45 meV. Finally, after fixing the locations of the two P atoms, we replaced every As atom located up to the fifth-layer by a P atom, followed by geometry optimization. The result showed that formation of a Ga-P-Ga-P chain in the third-layer on the plane which bisects the surface As dimer block is most energetically favorable (Figure 2.8f).

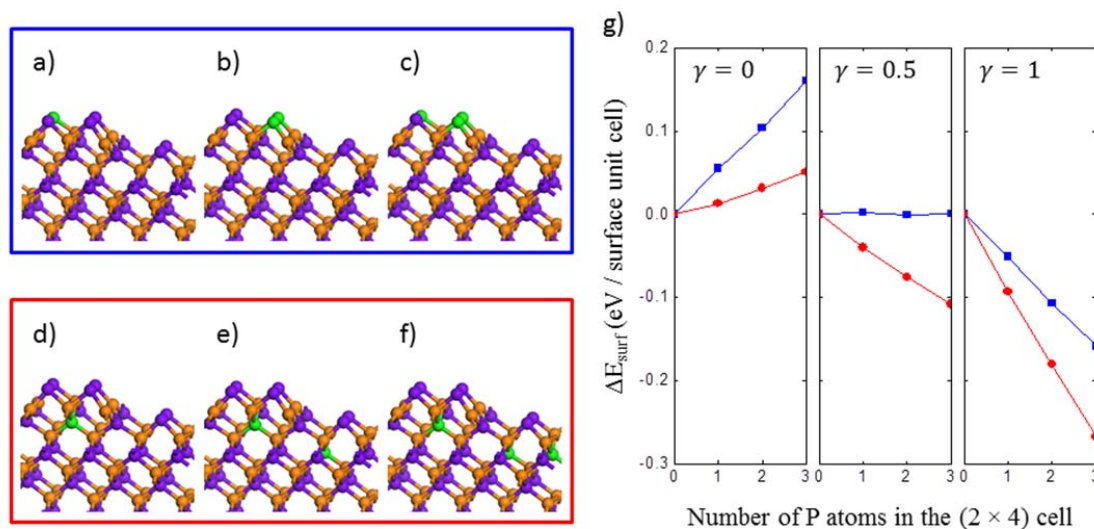


**Figure 2.8** DFT optimized geometries for a), d) one, b), e) two, and c), f) three As replacements by P in the GaAs(001)- $\beta 2(2 \times 4)$  model. The most stable geometries are shown among a) ~ c) surface and d) ~ f) subsurface P replacements at given numbers of P and As atoms in the  $(2 \times 4)$  cell. Purple, orange, and green spheres represent As, Ga, and P atoms, respectively. g) Relative surface formation energy versus the number of P atoms in the GaAs(001)- $\beta 2(2 \times 4)$  cell at three As chemical potentials ( $\Delta\mu(\text{As}) = \gamma \cdot \Delta H_f(\text{GaAs})$ ;  $\gamma = 0, 0.5, \text{ and } 1$ ). The chemical potential of P is fixed ( $\Delta\mu(\text{P})=0$ ).

A relative surface formation energy diagram, demonstrating the dependence on the number of P-replacements and the P chemical potential, is displayed in Figure 2.8g. In our experiments, we exposed the  $\beta 2(2 \times 4)$  surface to P flux, which is assumed to be an extremely P-

rich condition,  $\Delta\mu(\text{P}) = 0$ . On the other hand, the lack of As supply in our experimental condition yields the chemical potential of As ( $\Delta\mu(\text{As})$ ) to be lower than 0. Figure 2.8g shows three conditions; extremely As-rich ( $\gamma = 0$ ), intermediate ( $\gamma = 0.5$ ), and As-poor ( $\gamma = 1.0$ ).

The following results are motivated from our DFT simulations. First, at any given As chemical potential, the red points are below the blue points, meaning that replacement of As for P in the subsurface region is energetically more favorable than that on the surface. Second, at the experimental conditions reported herein, for example at a low As chemical potential, which is assumed to be  $\gamma = 0.5$  and 1, replacement of subsurface As by P is exothermic. On the other hand, replacement of surface As for P is exothermic when the As chemical potential is sufficiently lower (e.g.,  $\gamma \leq 0.5$ ). Third, the anion replacement is initiated from the third layer that is under the surface As dimer block, followed by the second replacement in the fifth layer under the As-As dimer which is at the trough. Further anion replacement forms a  $(\text{Ga-P})_n$  chain structure at the subsurface. Finally, anion replacement occurring at a location deeper than the third layer is energetically less favorable than that on the third layer.

## 2.7. Conclusion

The schematic diagram in Figure 2.9 displays the proposed film growth mechanism of  $\text{Zn}_3\text{P}_2$  on the Ga-rich GaAs(001). P bonds to the surface Ga atoms on the Ga-rich surface to form GaP interfacial layers. At initial coverages, STM observations indicated that the P atoms preferentially adsorb on the second layer Ga to form P-P or P-As dimer rows. This process was followed by the formation of featureless islands with random locations on the surface. The thickness of the GaP interface layer is dependent on both the initial Ga coverage and roughness of the clean substrate surface as well as the film growth temperature. Under further Zn and P flux, an epitaxial  $\text{Zn}_3\text{P}_2$  film grows, which was confirmed by XPS, XRD, and TEM. However, the surface of the  $\text{Zn}_3\text{P}_2$  epilayer remains covered by an elemental P and amorphous zinc phosphide overlayer with a total thickness of  $\sim 1$  nm. Formation of the P abundant overlayer is likely due to the low sticking coefficient of Zn as compared to P, especially at low  $\text{Zn}_3\text{P}_2$  coverage. Thus, the film growth is expected to be limited by Zn adsorption.

At higher temperatures, ( $> 490$  °C) Zn does not adsorb on the GaAs surface, but P does, to transform the GaAs(001)-(6 $\times$ 6) surface to the GaP(001)- $\delta$ (2 $\times$ 4) surface reconstruction with an

intermediate GaP(001)- $\beta 2(2 \times 4)$  reconstruction occurring. DFT simulations elucidate that when appropriate activation energy is supplied, the anion replacement of As by P in both surface and subsurface is exothermic under P rich and As poor conditions. In addition, As atoms in the third layer are preferentially replaced by P atoms by forming the (Ga-P)<sub>n</sub> chain. This simulation result is consistent with XPS observations where a GaP interfacial layer forms, but is limited to <1 ML even at temperatures as high as 560 °C and Zn<sub>3</sub>P<sub>2</sub> exposures as high as 18 L.

The compound source MBE is a simple and reliable technique for growing an Zn<sub>3</sub>P<sub>2</sub> epilayer on Ga-rich GaAs(001). The top P-rich overlayer may be used as a protecting layer for further application. Alternatively, it may need appropriate processes to remove the amorphous layer for further chemical functionalization or additional film growth. The thin interface GaP layer also can play a role in a hole barrier for electronic application.

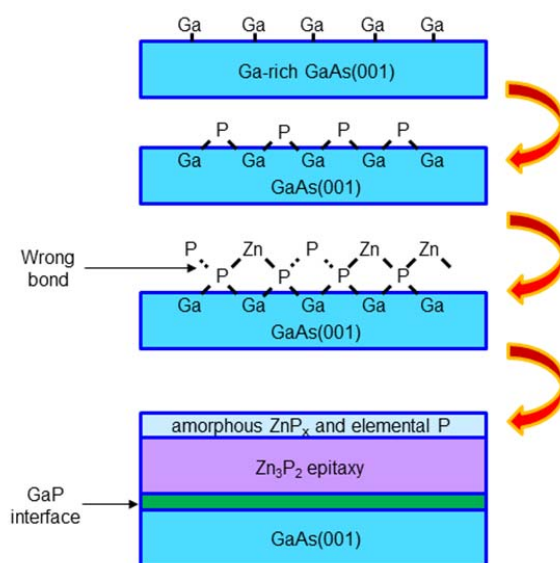


**Figure 2.9** Schematic pictures of the film growth mechanism of Zn<sub>3</sub>P<sub>2</sub>/GaAs(001).

## Chapter 3

# DFT Study of Water Adsorption and Decomposition on a Ga-Rich GaP(001)(2×4) Surface<sup>1</sup>

### 3.1 Introduction

The III-V compound semiconductor surfaces and interfaces lead to outstanding optical and electronic properties [61]. In particular while facilitating controllable electronic properties by forming III-V alloys [3, 62-65], epitaxy film growth on a silicon substrate due to small lattice mismatches (0.36%) [4] and selectivity for aqueous CO<sub>2</sub> reduction in photoelectrochemical systems [8-10] create a lot of potential applications.

We are interested in photoelectrodes of GaP and GaInP alloys since H<sub>2</sub> production or CO<sub>2</sub> reduction can be achieved in aqueous photoelectrochemical systems, making them of great interest for renewable energy research [8, 66]. In these photoelectrochemical systems, it is essential to understand how solvent interactions with semiconductor surfaces affect the reaction mechanisms at the semiconductor/electrolyte interfaces. Since water is a common precursor for the ALD process and wet oxidation, the preparation of stable surface oxides from water is likely to be involved in GaP-based device fabrications. Accordingly, it is important to determine the adsorption and decomposition reactions of water on the GaP surface.

---

<sup>1</sup> Reproduced with permission from Seokmin Jeon, Hyungjun Kim, William A. Goddard, III, and Harry A. Atwater, "DFT Study of Water Adsorption and Decomposition on a Ga-rich GaP(001)(2×4) Surface" *J. Phys. Chem. C*, **2012**, 116 (33), 17604-17612. Copyright 2012 American Chemical Society

Despite the wealth of quantum mechanical studies for adsorption, dissociation, or decomposition reactions of water on the (001) surfaces of elemental semiconductors such as silicon and germanium [67-70], there are few studies on any surface of III-V zinc blend semiconductors such as GaAs, GaP, and InP [66]. In addition, little molecular-level information has been reported on the adsorption and decomposition mechanisms of water on the GaP(001) surface.

The surface structure of GaP(001) is complex due to the presence of several surface reconstruction structures [44, 45, 61, 71, 72]. Of particular interest is the Ga-rich surface reconstruction structure since,

- 1) During the material growth processes [61] the desorption rate of a P atom is higher than that of a Ga atom under annealing conditions,
- 2) During the sputter-annealing process to remove the native oxide layer from GaP, P desorbs more easily than Ga [73].

Two likely Ga-rich reconstruction structures have been suggested from previous theoretical studies [17-20]; (2×4) Ga-P mixed dimer surface reconstruction and (2×4) Ga-Ga dimer surface reconstruction. Experimental studies, however, argued that the Ga-P mixed dimer was more stable than the Ga-Ga dimer in the commonly attainable Ga-rich conditions [44, 45, 61, 72]. Thus, we chose the Ga-rich GaP(001)(2×4) mixed dimer surface reconstruction structure as the clean surface structure in this study.

In this article, we report DFT studies of the adsorption and decomposition of a water molecule on the GaP(001)(2×4) surface. Here we considered a molecular coverage of 0.125 ML, and optimized the ground state energy to obtain the structures for both molecular adsorption and decomposition states. This provides the fundamental thermodynamics for the initial adsorption and decomposition processes of water molecules on the GaP(001)(2×4) surface.

## 3.2. Computational details

We carried out density functional theory (DFT) calculations using the exchange-correlation functional of Perdew-Burke-Ernzerhof (PBE). These calculations replaced the Ar core of Ga, the Ne core of P, and the He core of O with projected augmented-wave (PAW) potentials optimized for

PBE functionals. Thus Ga is described with three valence electrons, P with five, and O with six. All calculations used the Vienna Ab-initio Simulation Package (VASP). The electronic wave functions were expanded in a plane-wave basis set using a cutoff energy of 350 eV. The electron density was obtained from four k points generated by  $4 \times 2 \times 1$  Monkhorst-Pack scheme. The convergence criteria for electronic and ionic optimization were set to  $1 \times 10^{-4}$  and  $1 \times 10^{-3}$  eV, respectively. With this description we calculated a cubic lattice constant of 5.52 Å for bulk GaP (experimental value 5.45 Å [74]). Thus in the slab calculations we used this value for the periodic cell parameters in the x and y directions. All energies are for ground state structures at 0 K.

The Ga-rich GaP(001)( $2 \times 4$ ) mixed dimer surface was modeled using a periodic slab geometry composing of six Ga and P layers with a vacuum region equivalent to ten Ga and P layers (Figure 1.3b). This cell has 25 Ga and 25 P atoms. The bottom two Ga and P layers (eight Ga and eight P) were fixed with all remaining atoms fully relaxed. The bottom P layer was passivated with 0.75e- pseudo-hydrogen atoms to prevent charge separation, which exerts an artificial electrostatic force [33].

We calculated the adsorption energies of molecular and decomposed water on the GaP(001)( $2 \times 4$ ). The adsorption energy  $E_{ads}$  is obtained by subtracting the sum of the energies of water and bare GaP(001)( $2 \times 4$ ) from the total energy of water-adsorbed GaP(001)( $2 \times 4$ ):

$$E_{ads}(eV) = E_{tot}(H_2O \text{ adsorbed on GaP}) - E(GaP) - E(H_2O).$$

To obtain the ground state energy of a gas phase water molecule, the water molecule was modeled using a periodic cubic cell with a cell length of 15 Å.

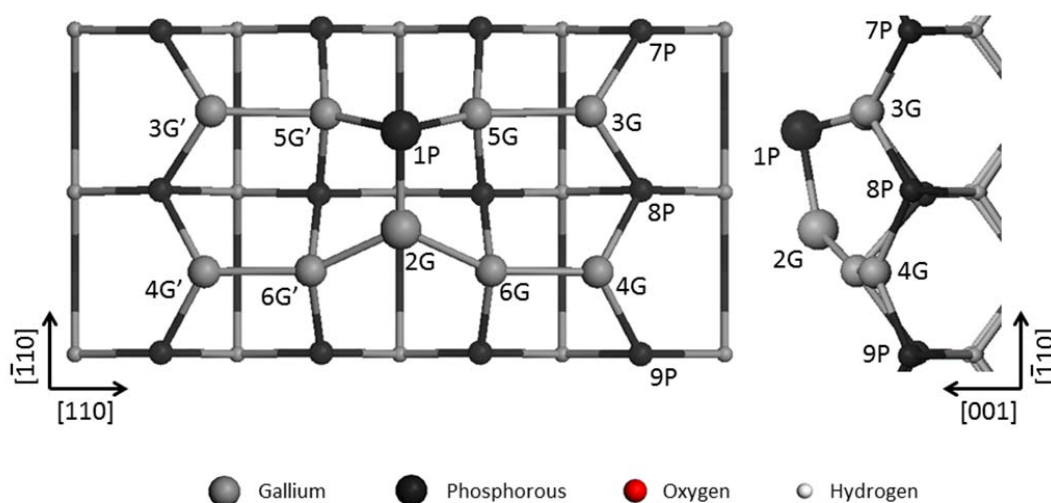


**Figure 3.1** Top and side views of the optimized geometry of the bare Ga-rich GaP(001)(2×4) mixed dimer model. 1P and 2G atoms are located on the 1<sup>st</sup> layer (top-most layer) with 1P bonded to 2G, 5G, and 5G' atoms and 2G bonded to 1P, 6G, and 6G' atoms. 3G, 3G', 4G, and 4G' atoms are located on the 2<sup>nd</sup> layer but each with just two bonds to P and one bond to Ga. 5G, 5G', 6G, and 6G' are located on the 2<sup>nd</sup> layer with four bonds (three P atoms and one Ga atom for 5G and 5G'; two P atoms and two Ga atoms for 6G and 6G'). 7P, 8P, and 9P atoms are located on the 3<sup>rd</sup> layer.

### 3.3 Result and discussion

#### 3.3.1 The reconstructed GaP(001)(2×4) surface

A top view of the GaP(001)(2×4) surface reconstruction model is displayed in Figure 3.1, with important structure parameters listed and compared with previous studies in Table 3.1 [61, 74, 75]. The main structural parameters, including dimer lengths and bucklings, are in good agreement with other calculation results. The buckling in the table is defined as the difference of the *Z* coordinates of two atoms consisting of a dimer. Small discrepancies in bond lengths and bucklings may arise from differences in the bulk lattice parameters. Throughout this report, for the reader's convenience, the surface Ga and P atoms of interest in the (2×4) unit cell are named 1P, 2 ~ 6G, 3 ~ 6G', 7 ~ 9P as shown in Figure 3.1.

Method	Lattice constant	$d_{\text{Ga-P}}^*$ 1 <sup>st</sup> layer	Ga-P buckling** 1 <sup>st</sup> layer	$d_{\text{Ga-Ga}}^*$ 2 <sup>nd</sup> layer	Ga-Ga buckling** 2 <sup>nd</sup> layer	P-P buckling** 3 <sup>rd</sup> layer
PBE model (this work)	5.502	2.402	0.403	2.58 ~ 2.74	0.431	0.337
LDA model [61]	5.42	2.36	0.39	2.47 ~ 2.62		
PW91 model [75]	5.50	2.403	0.385	2.58 ~ 2.73	0.43	0.31
experiment [74]	5.45					

**Table 3.1** Structural parameters of the bare Ga-rich GaP(001)(2×4) mixed dimer models (Unit: Å). \* The total bond distance in the first or second layer. \*\* The difference of Z coordinates of buckled pairs of atoms in the first, second, or third layer.

### 3.3.2. Premise and scope of the simulations

The (2×4) mixed dimer structure has several sites at which a single water molecule might bind, leading to a number of possible adsorption and decomposition states to consider. We consider here four binding states for H<sub>2</sub>O each of which may be involved in several adsorption and dissociation reaction pathways.

1. *Molecular adsorption state*; Section 3.3.3 considers that a water molecule binds to an empty orbital on the surface Ga. We examined atop, bridge, and hollow sites around the surface Ga atoms in the (2×4) unit to determine the energetically favorable adsorption geometries for the molecular adsorbate.
2. *HO/H decomposition state*; in Session 3.3.4 we examine preferred adsorption geometries for the two decomposition adsorbates.
3. *O/2H decomposition state*; in Session 3.3.5 we consider that the H atom of the HO adsorbate from the HO/H adsorption state could further decompose to create the O/2H decomposition state.
4. *Surface oxide state (O/H<sub>2</sub> state)*; Session 3.3.6 discusses energetics of the surface oxide states.

In this report, we do not consider the transition states between sequential ground states. Instead, we focus on exploring every possible intermediate state (local minimum) which might be

involved in the possible adsorption and decomposition reaction pathways in the 0.125 ML water/GaP(001)(2×4) system.

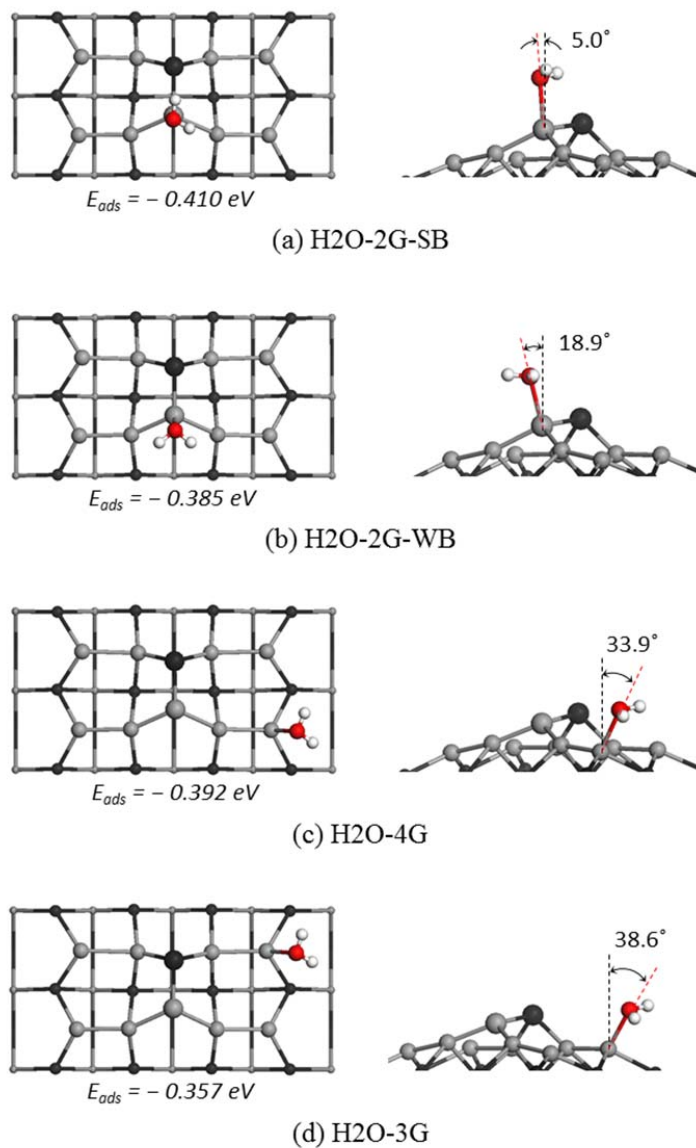


**Figure 3.2** The first column displays optimized geometries (top view) and corresponding adsorption energies of the molecular adsorption states. The second column displays the angles between surface normal (black dashed line) and O-Ga bond (red dashed line).

### 3.3.3. Molecular adsorption state

A water molecule with two lone pairs (LP) of electrons can bind as a Lewis base (LB) to the five surface Lewis acid (LA) sites in the (2×4) surface unit cell: 2G, 3G, 3G', 4G, and 4G', each of which makes three covalent bonds to its nearest neighbors, leaving an empty hybrid *p*-orbital to accept LP electrons of water (Figure 3.1). We expect no barrier in forming such LA-LB additions [76-81]. To obtain accurate adsorption ground states geometries, we optimized the geometries as follows. Since the (2×4) surface unit cell is symmetric with respect to the mirror plane that includes the [001] and [-110] vectors and bisects the surface unit cell, we considered only sites in the right half of the (2×4) unit cell (Figure 3.1). We started with 16 initial structures classified into three groups;

1. atop structures with the water molecule positioned at the top site: 1P, 2G, 3G, 4G, 5G, and 6G atoms,
2. bridge structures with the water molecule positioned at the bridge position of a pair of surface atoms: 1P-2G, 1P-5G, 2G-6G, 3G-5G, 4G-6G, 3G-7P, 3G-8P, 4G-8P, and 4G-9P,
3. a hollow structure with the water molecule positioned at the center of the trapezoid consisting of 3G, 4G, 5G, and 6G atoms.

For all 16 initial structures, a water LP was pointed toward nearby surface Ga atoms. After geometry optimization we found just four distinct local minimum structures from the 16 initial structures as shown in Figure 3.2 and Table 3.2.

Adsorption state	$E_{\text{ads}}$ (eV)	$d_{\text{Ga-O}}$ (Å)	$d_{\text{O-H1}}$ (Å)	$d_{\text{O-H2}}$ (Å)	$\Theta_{\text{H-O-H}}$ (°)
Water*			0.972	0.973	104.0
H2O-2G-SB	-0.410	2.308	0.976	0.983	106.4
H2O-2G-WB	-0.385	2.311	0.978	0.978	104.8
H2O-4G	-0.392	2.297	0.979	0.979	105.2
H2O-3G	-0.357	2.345	0.979	0.980	104.6

**Table 3.2** Adsorption energies and structural parameters for the molecular adsorption states. \* Values are obtained from the current calculation.

The adsorption energies calculated for these four states ( $-0.357$  to  $-0.410$  eV) are slightly larger than the adsorption energy in the  $\text{H}_2\text{O}/\text{Ge}(001)$  system ( $-0.33$  eV) but smaller than those in the  $\text{H}_2\text{O}/\text{Si}(001)$  system ( $-0.51$  eV to  $-0.57$  eV) [67-69]. For the water adsorbed on the 2G atoms, we found there are two stable adsorption geometries; strong bound state (H2O-2G-SB, Figure 3.2a) and weak bound state (H2O-2G-WB, Figure 3.2b). The adsorption energy for the H2O-2G-SB state is 0.025 eV greater than the H2O-2G-WB state. More importantly, the two H-O bond lengths in the H2O-2G-SB state differ from each other. The H-O bond parallel to the  $[-110]$  direction is longer than the other by 0.007 Å. This occurs because the LP on 1P atom interacts with the H atom of the  $\text{H}_2\text{O}$  adsorbate leading to stronger binding. On the other hand, for the molecular adsorption states on the G3 and G4 atoms (Figure 3.2c and d), the bonding is weak ( $-8.2 \sim -9.1$  kcal/mol), since no neighboring site provides an LP electron. For the weakly bound states (Figure 3.2b, c, and d), the geometry of the  $\text{H}_2\text{O}$  changes little upon bonding, leading to little change in the water LP, and we consider the bonding to be physisorption [82, 83]. Given the entropy of a free water of  $S = 45.1$  cal/mol·K =  $1.96 \times 10^{-3}$  eV/atom·K, [84] we expect desorption of water for the four molecular adsorption states at  $T > \Delta H/\Delta S = 209$  K. Finally, since the adsorption energies differ by only 0.05 eV, we expect them to have similar occupation over the three sites (2G, 3G, and 4G).

### 3.3.4 HO/H decomposition state

We predicted the stable adsorption geometries for the two adsorbates, HO and H, on the  $\text{GaP}(001)(2 \times 4)$ .

**3.3.4a 1P-2G site** One can think of the bonding here as adding the proton to the P LP pointed away from the surface to form a covalent P-H bond (1.425 Å, Table 3.3), which pulls the covalent 1P-2G bond pair toward the P (increasing it by 0.140 Å from 2.419 Å to 2.559 Å) to form a LA-LB bond while a LP on the OH<sup>-</sup> binds to what was originally an empty  $p$  orbital on 2G to form a covalent Ga-O bond (1.838 Å, Table 3.3). Thus, we started with the initial position of the H adsorbate on atop site of the 1P atom. The mechanism for forming this site might start with the 2G site of molecularly bound  $\text{H}_2\text{O}$  (Figure 3.2a), with the reaction coordinate involving the H moving toward to 1P lone pair. This mechanism is compatible with the known decomposition mechanism of water on GaAs(110) and GaAs(001) surfaces [76, 77, 85].

**3.3.4b 1P-3G and 1P-4G sites** Given the proton bonding to the P LP, we can expect that besides 2G, the OH<sup>-</sup> binds to the other good sites at the four other sites with Ga empty  $p$  orbitals: 3G, 4G and the equivalent 3G', 4G'. However we built all 13 initial structures in which the H is at 1P

while the HO adsorbate is located at atop site of the 2, 3, and 4G atoms, bridge site of the 1P-2G, 1P-5G, 2G-6G, 3G-5G, 4G-6G, 3G-7P, 3G-8P, 4G-8P, and 4G-9P atoms, and hollow site of the 3G-4G-6G-5G trapezoid. After geometry optimization, of the thirteen tested structures, three ground states have the most stable structures; HO-2G\_H-1P (considered above), HO-3G\_H-1P, and HO-4G\_H-1P; shown in Figure 3.3 with adsorption energies and structural parameters tabulated in Table 3.3.

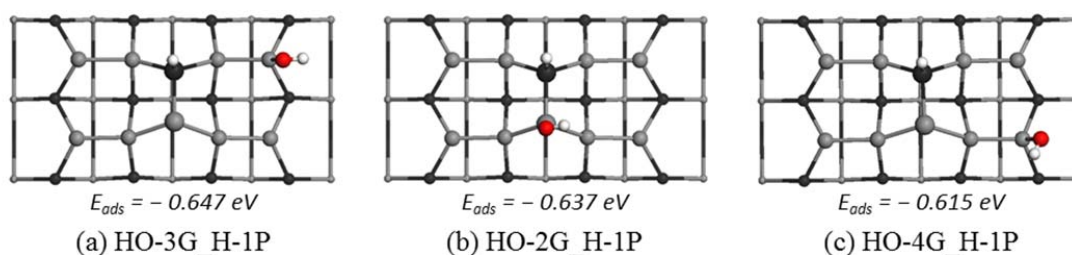


**Figure 3.3** Top view of the optimized geometries of HO/H decomposition states.

Adsorption state	$E_{ads}$ (eV)	$d_{Ga-O}$ (Å)	$d_{O-H}$ (Å)	$d_{P-H}$ (Å)	$\Theta_{Ga-O-H}$ (°)
HO-3G_H-1P	-0.647	1.842	0.974	1.427	109.3
HO-2G_H-1P	-0.637	1.838	0.976	1.425	110.9
HO-4G_H-1P	-0.615	1.842	0.972	1.431	109.4

**Table 3.3** Adsorption energies and structural parameters of HO/H decomposition states.

The final chemisorption energies of the three HO-XG\_H-1P (X=2, 3, and 4) states are within 5%, but the kinetic barriers to going from water to these states may be significantly different. Thus, we expect that the dissociation mechanism from the H<sub>2</sub>O-2G state to the HO-2G\_H-1P state is preferred, since H needs to move along by 2~3 Å in migrating from the O to the P. H must move by 4~5 Å in the HO-3G\_H-1P structure and 5~6 Å in the HO-4G\_H-1P structure, which would lead to a substantial barrier if only one H<sub>2</sub>O were available. In the presence of more water molecules in the unit cell, lower-barrier hydrogen relay mechanisms would likely lead to

lower barriers to form HO-3G\_H-1P or HO-4G\_H-1P. This may require surface water coverage exceeding 0.125 ML.

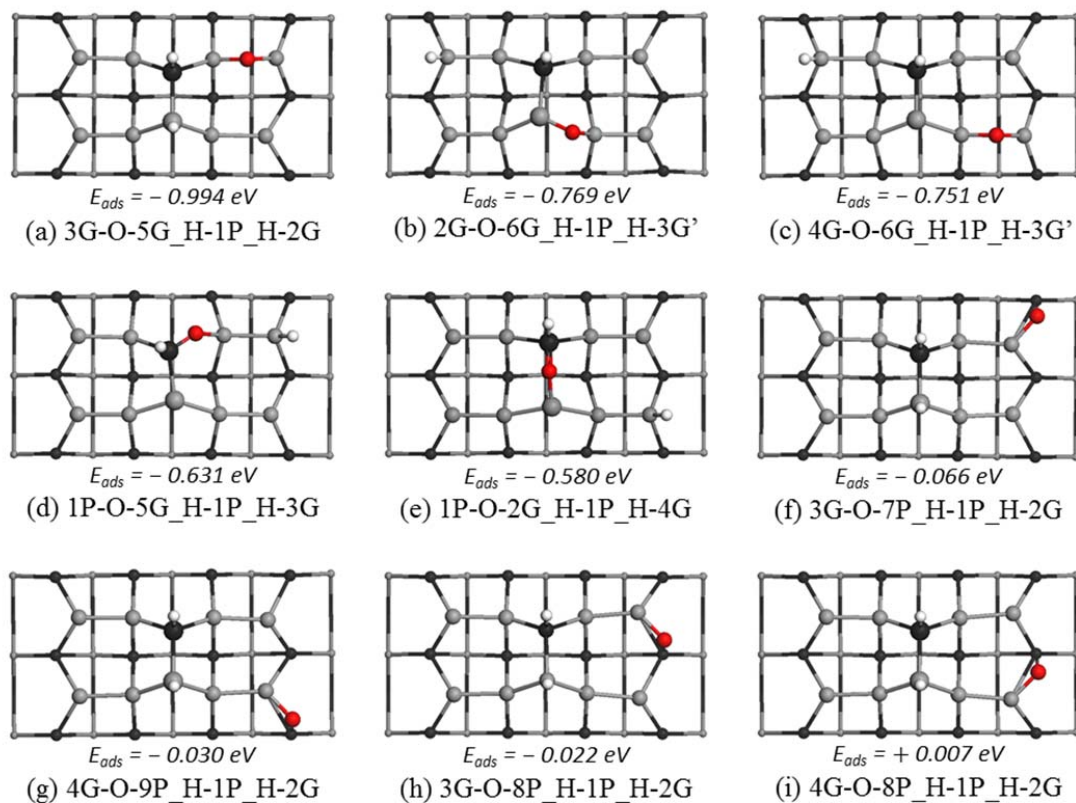


**Figure 3.4** Top view of the optimized geometries of O/2H decomposition states.

### 3.3.5 O/2H decomposition state

Next, we investigate complete decomposition of the water adsorbate with one oxygen and two hydrogens, where each reacts at sites on the GaP(001)(2×4) surface unit cell. To identify stable adsorption geometries for the oxygen adsorbate, we positioned an oxygen atom at several high symmetry positions (atop, bridge, and hollow sites) of the (2×4) unit cell and carried out geometry optimization. We find that the bridge positions are more favored than the other tested positions for the oxygen adsorption, which agrees well with a previous result [66]. For the H adsorbates, the atop positions are stable as we already mentioned in Session 3.3.4.

Adsorption state	$E_{\text{ads}}$ (eV)	$d_{\text{Ga-O}}$ (Å)	$d_{\text{A*O}}$ (Å)	$\Theta_{\text{Ga-O-A*}}$ (°)	$d_{\text{P-H}}$ (Å)	$d_{\text{Ga-H}}$ (Å)
3G-O-5G_H-1P_H-2G	-0.994	1.791	1.871	117.4	1.427	1.570
2G-O-6G_H-1P_H-3G'	-0.769	1.827	1.812	117.3	1.429	1.577
4G-O-6G_H-1P_H-3G'	-0.751	1.793	1.860	119.0	1.428	1.574
1P-O-5G_H-1P_H-3G	-0.631	1.969	1.586	128.0	1.433	1.571
1P-O-2G_H-1P_H-4G	-0.580	1.945	1.583	130.0	1.434	1.569
3G-O-7P_H-1P_H-2G	-0.066	1.897	1.463	110.5	1.425	1.571
4G-O-9P_H-1P_H-2G	-0.030	1.907	1.458	109.1	1.427	1.568
3G-O-8P_H-1P_H-2G	-0.022	1.894	1.457	109.1	1.425	1.572
4G-O-8P_H-1P_H-2G	+0.007	1.905	1.516	111.6	1.426	1.570

**Table 3.4** Adsorption energies and structural parameters of O/2H decomposition states. \* A = Ga or P

There are a total of 17 Ga-Ga or Ga-P bridge sites for an oxygen atom to sit on in the (2×4) unit cell, but eight of them are redundant due to mirror symmetry. Thus, we considered the nine bridge oxide structures; 1P-O-2G, 1P-O-5G, 2G-O-6G, 3G-O-5G, 4G-O-6G, 3G-O-7P, 3G-O-8P, 4G-O-8P, and 4G-O-9P. For each of these nine cases (except for the 1P-O-2G structure), there are six available atop positions for the H. This leads to  $6 \times 5/2 = 15$  possible cases for two H to sit on. As discussed in Session 3.3.4, hydrogen prefers to bond with the 1P atom rather than the Ga; hence, we assumed that one of the hydrogen atoms is located on top of 1P (H-1P), leading to five possibilities for the other hydrogen adsorption sites (H-XG, where XG=2G, 3G, 3G', 4G and 4G') per bridge oxide configuration. The 1P-O-2G structure, however, has only three different initial structures due to mirror symmetry. Then we carried out geometry optimizations for all the 43 structures. [86]

We sorted these 43 into nine groups; each containing five structures with the same oxygen site and the same first hydrogen site to be atop 1P, but varying the site for the second hydrogen atom to be atop 2G, 3G, 3G', 4G, or 4G' (in the group containing the 1P-O-2G configuration, there are only three sites for the second H due to mirror symmetry; 2G, 3G, and

4G). We find that within a given group, the adsorption energies of the five different structures vary by just 0.15 eV. Of these five structures, one is particularly less stable than the other four. That is, when the second hydrogen atom is bound to the Ga atom which is a member of a bridge Ga-O-Ga configuration, the adsorption energy is the least of the five structures. This is because the Ga-O-Ga configuration leads to the best energetics of the O/2H ground states. When a hydrogen atom bonds with one of Ga atoms of this Ga-O-Ga, the bonds around the H-bound Ga atom change from  $sp^2$  to  $sp^3$  hybrid character. The significant change of the ideal bond angle ( $120^\circ$  to  $109.5^\circ$ ) induced by the change of hybridization builds up geometrical strains around the H-bound Ga atom, resulting in a smaller adsorption energy. On the other hand, for the other four states where the second hydrogen bonds with an  $sp^2$  Ga atom not involved in the Ga-O-Ga, the change of hybridization of the bonds around the H-bound Ga atoms does not destabilize the adsorption structure as significantly as for the Ga-O-Ga-H configuration. Figure 3.4 and Table 3.4 show the geometries, adsorption energies, and structural parameters of nine representatives of the 43 optimized structures. Each representative structure has the most stable adsorption energy among the three (in 1P-O-2G group) or five (in eight other groups) other structures in each group.

### 3.3.6 Surface oxide state (O/H<sub>2</sub> state)

The remaining adsorption state for water adsorption and decomposition reactions is the surface oxide state with both H adsorbates leaving as an H<sub>2</sub> molecule. Surface oxide formation after desorption of H<sub>2</sub> has been observed experimentally in temperature programmed desorption (TPD) experiments on water/GaAs(001) [76, 77]. Sloan et al. observed the D<sub>2</sub> TPD peak at 400 ~ 600 K from the GaAs(100) surface which had been covered with D<sub>2</sub>O dissociative adsorbates. Chung et al. also obtained the D<sub>2</sub> desorption spectrum at 600 ~ 700K from the D<sub>2</sub>O adsorbed GaAs(001)(4×2) surface. They suggested a D<sub>2</sub> regeneration mechanism in which the D<sub>2</sub> gas is produced from two hydroxyl adsorbates when the surface is annealed. To provide insights about the energetics of this mechanism while keeping the simulation cell size (surface water coverage of 0.125 ML) fixed, we calculated the final ground states where the oxide is left on the GaP surface after the desorption of a H<sub>2</sub> molecule.

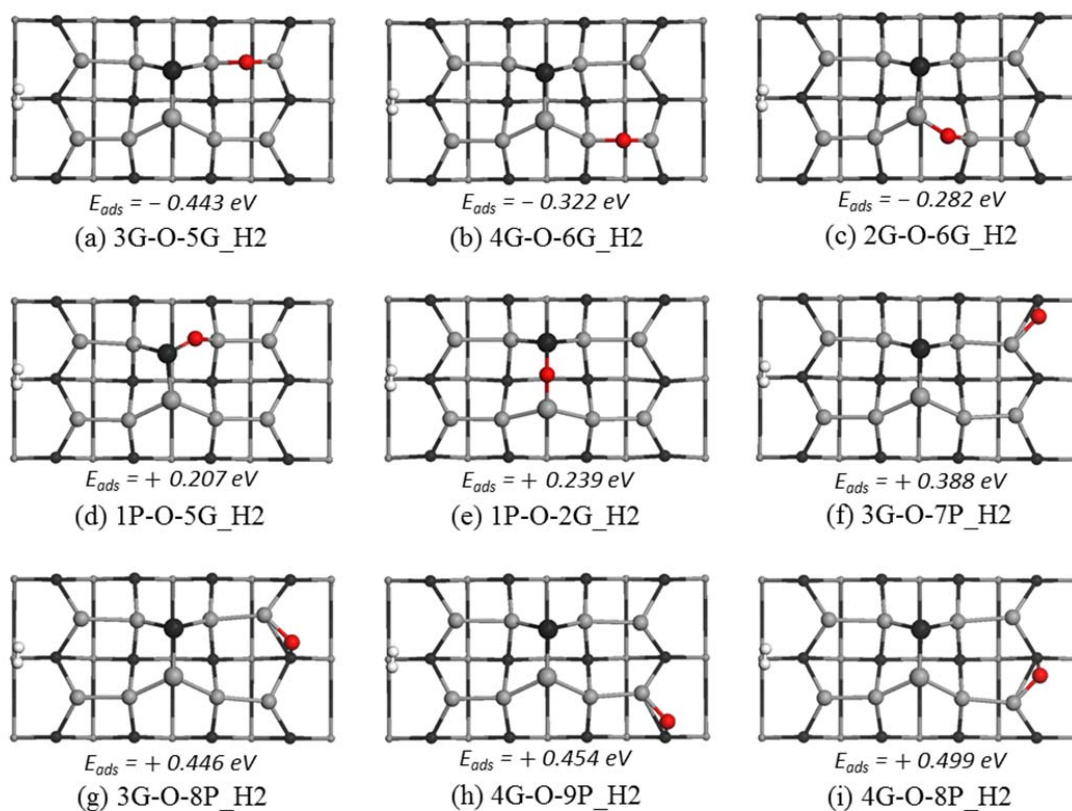


**Figure 3.5** Top view of optimized geometries of surface oxide states.

We built the initial structures for the oxygen adsorbates whose coordinates referred to those of the oxygen adsorbates in the optimized structures of the O/2H state in Session 3.3.5. Figure 3.5 and Table 3.5 show the final structures and their energies in the surface oxide state. The two hydrogen atoms in the surface oxide state are combined to a hydrogen molecule in the vacuum. Since we want to describe a desorbed hydrogen molecule, we selected the initial coordinates of the hydrogen molecule to be as far as possible from either top or bottom surface. During the geometry optimization the coordinates of the hydrogen atoms in vacuum are fully relaxed, but the coordinates of the hydrogen molecule remain little changed in the final structures (less than 0.1%) implying negligible interactions between the hydrogen molecule and the two surfaces. To verify that the presence of an H<sub>2</sub> in the vacuum of the simulation unit cell does not affect on energetics of the surface oxide, we compared the coordinates of the surface atoms and the adsorption energies for the surface oxide structure with and without a hydrogen molecule in

vacuum.[86] For all simulated oxide structures, differences of the coordinates of surface atoms and the adsorption energies for the two structures are less than 2 % and 0.4 %, respectively. More importantly, there was no correlation between the variation on the hydrogen-to-surface distance and the variation on the adsorption energy. That is, the small energy difference (0.4%) might arise only from slight differences in the convergence levels in the structures during the geometry optimization. Therefore, our O/H<sub>2</sub> state models are appropriately constructed to represent the surface oxide state where hydrogen adsorbates are completely desorbed from the surface.

From the simulation results of the surface oxide state summarized in Table 3.5, we conclude that thermodynamically stable oxide structures after the hydrogen molecule is desorbed are Ga-O-Ga surface bridge structures. The net enthalpy changes for forming the surface Ga-O-Ga bridge oxides are negative (thermodynamically favored) compared to the reference state of water plus clean GaP surface. In contrast the surface oxide states involving the Ga-O-P bridge structures, are less stable than this reference.

Adsorption state	$E_{\text{ads}}$ (eV)	$d_{\text{Ga-O}}$ (Å)	$d_{\text{A}^*\text{-O}}$ (Å)	$\Theta_{\text{Ga-O-A}^*}$ (°)	$d_{\text{H-H}}$ (Å)	$d_{\text{H}_2\text{-4G}^{**}}$ (Å)
3G-O-5G_H2	-0.443	1.887	1.781	119.3	0.748	8.223
4G-O-6G_H2	-0.322	1.857	1.790	120.3	0.749	8.233
2G-O-6G_H2	-0.282	1.820	1.818	116.4	0.747	8.232
1P-O-5G_H2	+0.207	1.881	1.628	132.5	0.752	8.239
1P-O-2G_H2	+0.239	1.883	1.621	138.8	0.748	8.213
3G-O-7P_H2	+0.388	1.913	1.458	112.7	0.752	8.221
3G-O-8P_H2	+0.446	1.909	1.423	111.3	0.751	8.221
4G-O-9P_H2	+0.454	1.892	1.468	107.3	0.751	8.221
4G-O-8P_H2	+0.499	1.888	1.500	108.7	0.749	8.222

**Table 3.5** Adsorption energies and structural parameters of surface oxide states. \* A = Ga or P. \*\* Distance between the center of two H atoms and the nearest Ga or P atom located on the surface.

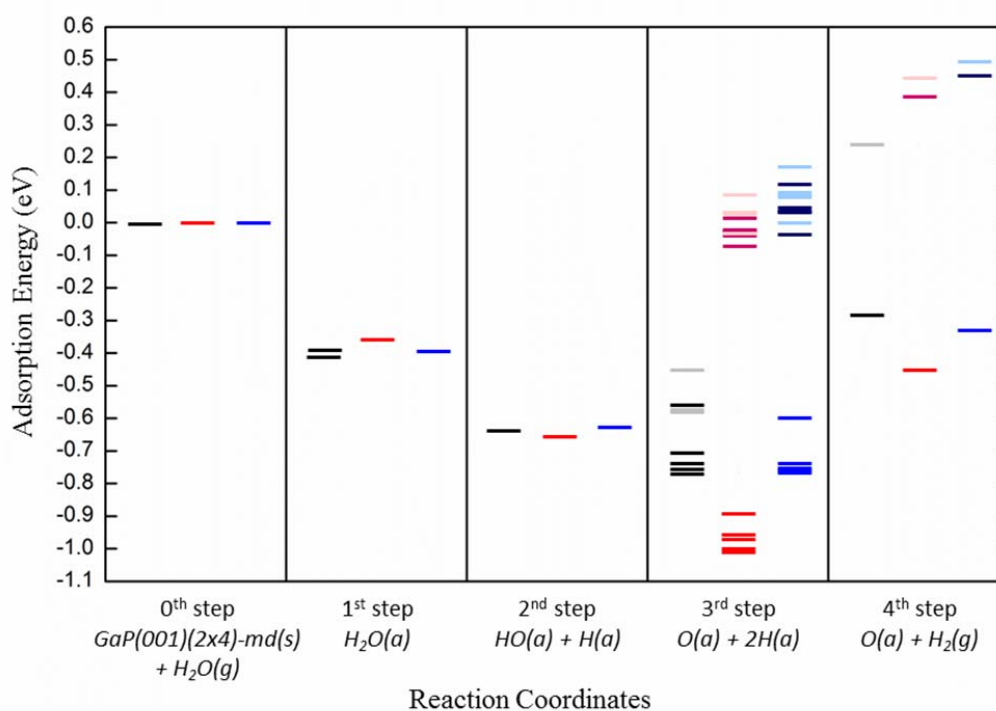


**Figure 3.6** Adsorption energies versus reaction coordinates of entire adsorption states.

**Black lines** indicate the mechanism for  $\text{H}_2\text{O}-2\text{G}-\text{WB}, \text{H}_2\text{O}-2\text{G}-\text{SB} \rightarrow \text{HO}-2\text{G}_\text{H-1P} \rightarrow 2\text{G}-\text{O}-6\text{G}_\text{H-1P}_\text{H-XG} \rightarrow 2\text{G}-\text{O}-6\text{G}_\text{H}_2$  ( $\text{XG}=2\text{G}, 3\text{G}, 3\text{G}', 4\text{G}$  and  $4\text{G}'$ ). In the 3<sup>rd</sup> and 4<sup>th</sup> steps, we use gray for  $1\text{P}-\text{O}-2\text{G}_\text{H-1P}_\text{H-XG}$  and  $1\text{P}-\text{O}-2\text{G}_\text{H}_2$  states.

**Red lines** indicate the mechanism for  $\text{H}_2\text{O}-3\text{G} \rightarrow \text{HO}-3\text{G}_\text{H-1P} \rightarrow 3\text{G}-\text{O}-5\text{G}_\text{H-1P}_\text{H-XG} \rightarrow 3\text{G}-\text{O}-5\text{G}_\text{H}_2$  ( $\text{XG}=2\text{G}, 3\text{G}, 3\text{G}', 4\text{G}$  and  $4\text{G}'$ ). In the 3<sup>rd</sup> and 4<sup>th</sup> steps, we use dark red for  $3\text{G}-\text{O}-7\text{P}_\text{H-1P}_\text{H-XG}$  and  $3\text{Ga}-\text{O}-7\text{P}_\text{H}_2$  states, and light red for  $3\text{G}-\text{O}-8\text{P}_\text{H-1P}_\text{H-XG}$  and  $3\text{G}-\text{O}-8\text{P}_\text{H}_2$  states.

**Blue lines** indicate the mechanism for  $\text{H}_2\text{O}-4\text{G} \rightarrow \text{HO}-4\text{G}_\text{H-1P} \rightarrow 4\text{G}-\text{O}-6\text{G}_\text{H-1P}_\text{H-XG} \rightarrow 4\text{G}-\text{O}-6\text{G}_\text{H}_2$  ( $\text{XG}=2\text{G}, 3\text{G}, 3\text{G}', 4\text{G}$  and  $4\text{G}'$ ). In the 3<sup>rd</sup> and 4<sup>th</sup> steps, we use dark blue for  $4\text{G}-\text{O}-9\text{P}_\text{H-1P}_\text{H-XG}$  and  $4\text{G}-\text{O}-9\text{P}_\text{H}_2$  states, and light blue for  $4\text{G}-\text{O}-8\text{P}_\text{H-1P}_\text{H-XG}$  and  $4\text{G}-\text{O}-8\text{P}_\text{H}_2$  states.

### 3.3.7 Overall reaction mechanism

Sessions 3.3.3 ~ 3.3.6 explored all ground states potentially involved in the adsorption and decomposition mechanisms of a single water molecule on the Ga-rich GaP(001)(2×4) mixed-dimer surface. Although we did not calculate the transition states for the reactions forming these states from H<sub>2</sub>O, we suggest some possible reaction pathways in Session 3.3.7. Figure 3.6 indicates the adsorption energies of all the ground states introduced above. Ground states with the same color indicate adsorption species that we assume are involved in the same reaction pathway. For instance, the black lines along the reaction coordinates indicate the ground states in the decomposition mechanism of the water molecule adsorbed on the 2G site.

#### *Black mechanisms*

In Figure 3.6, the black lines in each step indicate the adsorption energies for the mechanism; H<sub>2</sub>O-2G-WB, H<sub>2</sub>O-2G-SB → HO-2G\_H-1P → 2G-O-6G\_H-1P\_H-XG → 2G-O-6G\_H<sub>2</sub> (XG=2G, 3G, 3G', 4G and 4G'). Here Gray lines indicate the adsorption energies for 1P-O-2G\_H-1P\_H-XG (XG=2G, 3G, 3G', 4G and 4G') states in the third step and the 1P-O-2G\_H<sub>2</sub> state in the fourth step. We see that adsorption of a water molecule onto the 2G atom is thermodynamically favored (the first step to the second step in Figure 3.6). Then the molecular water adsorbate on 2G decomposes to form the HO-2G\_H-1P state with a small transition energy, because such hydrogen dissociation-and-transportation within one dimer is frequently observed in surface decomposition reactions [67-70, 79-81]. When energy is further supplied to the HO-2G\_H-1P state, two competitive decomposition pathways are followed (black and gray in the third step, Figure 3.6). The hydroxyl group (HO-2G) may transform to either 2G-O-6G bridge states (black lines in the third step, Figure 3.6) or 1P-O-2G bridge states (grey lines in the third step, Figure 3.6). Of the two surface oxide states, the 2G-O-6G bridge state has lower adsorption energy and will be more favored than its counter pathway.

#### *Red mechanisms*

Red lines represent the adsorption energies for the mechanism; H<sub>2</sub>O-3G → HO-3G\_H-1P → 3G-O-5G\_H-1P\_H-XG → 3G-O-5G\_H<sub>2</sub> (XG=2G, 3G, 3G', 4G and 4G'). Here dark red lines display the adsorption energies of the 3G-O-7P\_H-1P\_H-XG (XG=2G, 3G, 3G', 4G and 4G') state in the third step and the 3Ga-O-7P\_H<sub>2</sub> state in the fourth step. The light red lines

represent the adsorption energies of 3G-O-8P\_H-1P\_H-XG (XG=2G, 3G, 3G', 4G and 4G') states in the third step and the 3G-O-8P\_H2 state in the fourth step. We expect that the decomposition reaction pathway from the H2O-3G state to the HO-3G\_H-1P state will require a high activation energy due to the long H transportation distance. However, with additional waters or dissociated water species to help H transfer, there may exist other low barrier pathways for this reaction (requiring higher water coverage than 0.125 ML). Otherwise, decomposition proceeds from the H2O-3G state to the 3G-O-5G\_H-1P\_XGa state through another HO/H decomposition state whose adsorption energy is not, however, lower than that of the HO-3G\_H-1P state.

### *Blue mechanisms*

The blue lines represent the adsorption energies for the mechanism, H2O-4G → HO-4G\_H-1P → 4G-O-6G\_H-1P\_H-XG → 4G-O-6G\_H2 (XG=2G, 3G, 3G', 4G and 4G'). The dark blue lines represent the adsorption energies of the 4G-O-9P\_H-1P\_H-XG (XG=2G, 3G, 3G', 4G and 4G') states in the third step and the 4G-O-9P\_H2 state in the fourth step. The light blue lines represent the adsorption energies of the 4G-O-8P\_H-1P\_H-XG (XG=2G, 3G, 3G', 4G and 4G') states in the third step and the 4G-O-8P\_H2 state in the fourth step. The decomposition pathway from H2O-4G to HO-4G\_H-1P would have a high activation barrier just as in the H2O-3G decomposition. Since the hydrogen transportation distance is even longer than in either the H2O-2G or H2O-3G cases, it is unlikely for H2O-4Ga to be directly transformed to 4G-O-6G\_H-1P\_H-XG unless a second water or decomposed water species is involved.

### *Comparison of black, red, and blue mechanisms*

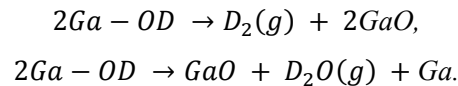
All three adsorption pathways are exothermic from the zeroth step to the first step. In the first step, the energy variations for the three adsorption states (H2O-2, 3, and 4G) are small. Similarly, the H decomposition reactions from the first step to the second step are exothermic for all three cases. In addition, since the three HO decomposition states have comparable adsorption energies, there is no preference over the three decomposition pathways in terms of thermodynamics. However, considering kinetics of the decomposition reactions (first step to second step), we anticipate that the HO-2G\_H-1P state is favored, since the H transportation distance, which is related to barrier height, is much shorter than for the other structures.

In the third step, noticeable differences are observed for the adsorption energies of eight surface bridge oxide groups (black, grey, red, light red, dark red, blue, light blue, and dark blue).

- First, the Ga-O-Ga bridge oxide configurations are more stable than the Ga-O-P bridge oxide configurations.
- Second, the bridge oxides consisting of second layer Ga atoms and third layer P atoms (light red, dark red, light blue, and dark blue), whose adsorption energies are larger than the zeroth step energy, 0 eV, are very unstable.
- Third, when comparing with the energies of three groups of Ga-O-Ga bridge oxides such as 2G-O-6G\_H-1P\_H-XG (black) (XG=2G, 3G, 3G', 4G and 4G'), 3G-O-5G\_H-1P\_H-XG (red), and 4G-O-6G\_H-1P\_H-XG (blue), the 3G-O-5G\_H-1P\_H-XG group is the most stable. The three decomposition pathways connecting the black, red, and blue lines between the second step and the third step are thermodynamically favorable. Of the three pathways, the pathway to form the 3G-O-5G configuration is the most favorable. However, since we have not verified the transportation mechanism of the second hydrogen atom from the HO configuration to the H-Ga configuration, we cannot conclude which pathway is preferred.

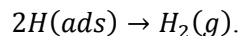
In the fourth step, after desorption of hydrogen adsorbates, we suggest the Ga-O-Ga bridged oxide to be the most stable adsorption configuration. The adsorption energy for the bridge oxide state is lower than the initial state. Thus, decomposition of water to form surface oxide on the Ga-rich GaP(001)(2x4) mixed dimer surface is thermodynamically favorable.

Ref. [77] suggested that surface oxides are formed after regeneration and desorption of water or hydrogen gases from two HO adsorbates rather than from two hydrogen adsorbate,



This hydrogen regeneration was verified using TPD, HREELS, and XPS experiments. Since we restricted ourselves to one H<sub>2</sub>O per cell, we could not examine this mechanism, which we consider reasonable. However we do describe the final GaO formed.

Foord et al. [87] observed regeneration of hydrogen gas from hydrogen adsorbates on the GaAs(100) surface and suggested a hydrogen regeneration mechanism in the H<sub>2</sub>S/GaAs(100) system which proceeds through



It seems to us that an intermediate mechanism in which a weaker surface H starts to break and then forms H<sub>2</sub> from an adjacent OH might be reasonable. However this last step of H<sub>2</sub> formation will require detailed reaction pathways starting with the species we have enumerated.

### *Caveats*

In this chapter, we discuss extensively the thermodynamics of all possible stable ground states, but we do not suggest full decomposition and desorption mechanisms to clarify how surface oxide and gaseous hydrogen are formed from HO and H adsorbates. Therefore, one should use care when interpreting the reaction pathways in Figure 3.6; especially, the pathways from the second step to the fourth step.

Since the pathways do not include transition state energies, there could be additional barriers and local minima between neighboring ground states. In addition, we have kept the water coverage at 0.125 ML for each (2×4) unit cell. However, it could be that some cells would locally have more than one water molecule even though the average coverage is 0.125 ML. For instance, there might be two neighboring HO adsorbates in one (2×4) unit cell, which could lead to a lower barrier pathway to produce the final surface oxide state similar to that observed in the water/Ga-rich GaAs(001)(2×4) system [77].

## 3.4 Conclusion

We report here, the adsorption and decomposition thermodynamics of 0.125 ML water on a Ga-rich GaP(001)(2×4) surface predicted using ab-initio DFT simulation. This surface reconstruction is complicated, leading to a number of potential decomposition reaction pathways. This study is the first to exhaustively consider the various possible reaction intermediates involved in mechanisms of water-induced transformations on GaP(001)(2×4). Here we explore all reasonable ground states involved in most possible adsorption and decomposition pathways, but we have not provided the full reaction mechanism, which would require searching transition states and quantifying barrier heights.

We consider a sequence of the ground states involving four adsorption states:

- The molecular water adsorption state, where we find that the molecular adsorption geometry is most stable when H<sub>2</sub>O is adsorbed on top of the surface *sp*<sup>2</sup> Ga atom of either Ga-P mixed dimer or Ga-Ga dimers.
- The HO/H decomposition state, where we find that the HO group bonds with a surface *sp*<sup>2</sup> Ga atom, and H binds to with the first layer P atom, with both HO and H groups having the atop configurations.
- The O/2H decomposition state, where the thermodynamically favorable adsorption structure for the O atom is the bridged Ga-O-Ga structure. Here the one hydrogen adsorbate prefers to be located on top of the first layer P atom while the other prefers a surface of *sp*<sup>2</sup> Ga atoms.
- The surface oxide state, where the O atom forms the Ga-O-Ga bridge oxide configuration after desorption of H<sub>2</sub>. The oxide formation process is exothermic when referenced to the initial state energy.

## *Chapter 4*

# Investigation of Adsorption Geometries and Thermal Decomposition Reactions of Alkanethiol Molecules on a Ga-Rich GaP(001)(2×4) Surface

## 4.1 Introduction

Organic thin film technologies using alkanethiols are widely used to chemically modify and physically/electronically protect a variety of metal and semiconductor surfaces [88-90]. Among many systems, the alkanethiol-bound gold surface has been most frequently and thoroughly researched. The usefulness of the Au-S bond stems from the appropriate strength of the bond. That is, long alkanethiol molecules form a self-assembled monolayer (SAM) on the surface when intermolecular interaction is stronger than the Au-S bond.[88] On the other hand, in some applications the strong character of the Au-S covalent bond is used to attach organic or bio molecules to the surfaces of planar Au films and Au particles.[91, 92]

The scope of research on alkanethiol-based thin films formation has been extended to III-V semiconductors. Due to the applications of III-V semiconductor materials in advanced electronics and optoelectronics, much research has been performed on alkanethiol/III-V semiconductor systems. [93-96] In addition to the existing merits of the depositing alkanethiol films on inert metal surfaces for use as chemical functionalization and protection, binding sulfur onto the III-V semiconductor surfaces adds additional benefits to the electronic properties of the III-V semiconductors. Sulfur has been reported to be one of the best reagents for passivation of trap states on various semiconductor

surfaces, these surface trap states being one of the main sources of degradation in the electronic properties of the semiconductor devices.[97]

The covalent bonding between S and the III-V semiconductor surface atoms can be used to graft molecules to the surfaces.[98] This strong grafting is necessary in modifying and functionalizing the semiconductor surface with organic molecules. Thus, it is important to understand the adsorption geometries and energetics of alkanethiol molecules on such surfaces. In spite of its significance, fundamental research on the adsorbate structures and corresponding energetics on the III-V semiconductor surfaces has not yet been thoroughly conducted. In addition, most surface studies of alkanethiol molecules adsorbed on the III-V semiconductors have been dependent on spectroscopic techniques such as X-ray photoelectron spectroscopy (XPS) and thermal desorption spectroscopy (TDS). These are powerful tools for exploring reaction chemistry but do not provide information for investigating the detailed molecular structure of the adsorbate.

In this chapter, we use high-resolution scanning tunneling spectroscopy (STM) and density functional theory (DFT) calculations to elucidate the geometry and energetics of alkanethiol molecules adsorbed to the Ga-rich GaP(001)(2×4) mixed-dimer surface. We also investigate the effect of annealing on the adsorption geometry and bonding characteristics using X-ray photoelectron spectroscopy (XPS) as well as the previous two techniques.

## 4.2 Experimental and computational details

A GaP(001) sample (*n*-type, carrier concentration  $1.7 \times 10^{18} \text{ cm}^{-3}$ , EL-CAT Inc.) was cleaved and mounted to a tantalum sample plate using two tantalum foils, and then loaded into the ultra-high vacuum (UHV) sample preparation chamber (base pressure  $< 1 \times 10^{-10}$  Torr). The GaP(001) sample surface was cleaned by several cycles of sputtering with 500 eV  $\text{Ne}^+$  ions for 7 min at 250 °C and annealing at 500 °C for 10 min in the preparation chamber. A type-K thermocouple and infrared optical pyrometer were used to measure the temperature of the GaP(001) sample while preparing the clean surface as well as during annealing of molecule-dosed GaP surfaces.

After preparing a sample in the preparation chamber, it was transferred under vacuum to the STM chamber (base pressure  $< 3 \times 10^{-11}$  Torr). A large domain composed of a single surface

reconstruction structure which was the Ga-rich GaP(001)-(2×4) mixed-dimer reconstruction [44, 71] was reliably observed by scanning tunneling microscopy (STM), with images matching those previously reported. [61, 99]

1-propanethiol (99 %, Aldrich), 1-octanethiol (98.5 %, Aldrich), 1,2-ethanedithiol (98 %, Fluka), and dipropyl disulfide (98 %, Aldrich) were purchased and further purified by several freeze-pump-thaw cycles to remove dissolved gases prior to exposure to the sample. The source chemicals were inserted into the STM chamber using a variable leak valve at room temperature (RT). The temperature of the sample surface during dosing varied from 130 K to RT. The temperature was measured using a Si diode temperature sensor embedded in the commercial STM system.

The scanning tunneling microscopy (STM) characterization of the surface topography was carried out using a commercial STM (VT-STM XA 50/500, Omicron Nanotechnology). The filled-state STM images were obtained in a constant current mode with the sample bias voltage varied from  $-3.5\text{ V} \sim -4.5\text{ V}$  and set-point current of  $100 \sim 200\text{ pA}$ . All STM experiments were collected using a commercial tungsten tip (Bruker Corp) which was fabricated using the electrochemical etching method.

X-ray photoelectron spectroscopy (XPS) measurements were carried out in a separate UHV chamber (base pressure,  $< 3 \times 10^{-9}$  Torr) which was located in Beckman Institute, California Institute of Technology, Pasadena, USA. The system is equipped with a Kratos Ultra DLD spectrometer and monochromatic Al  $K\alpha$  radiation ( $h\nu = 1486.58\text{ eV}$ ) source. The alkanethiol/GaP(001) samples were transferred from the STM prep chamber to the XPS chamber in a portable stainless steel chamber filled with anhydrous nitrogen gas. Thus, exposure to ambient gas during transportation was minimized. Low-resolution survey and high-resolution spectra were collected at fixed analyzer pass energies of 80 and 10 eV, respectively. The spectra were collected at  $45^\circ$  with respect to the surface normal direction. The binding energies of the spectra were referenced to the clean Au  $4f_{7/2}$  core level spectrum with a fixed binding energy of 84.0 eV. The XPS data were analyzed with commercial software, CasaXPS (version 2.3.16). The individual peaks were fitted with a Gaussian/Lorentzian product function after a Shirley-type background subtraction. Spin-orbit splittings and branching ratios were held constant; 1.1 eV and

0.51 for S  $2p$  core level, 0.86 eV and 0.52 for P  $2p$  core level, and 0.44 eV and 0.69 for Ga  $3d$  core level, respectively.[55]

The substrate-overlayer model [100] was used to calculate the coverage of surface-adsorbed molecules and sulfur atoms from the XPS core-level spectroscopic data.

$$\frac{I_{ov}}{I_{sub}} = \left( \frac{SF_{ov}}{SF_{sub}} \right) \left( \frac{\rho_{ov}}{\rho_{sub}} \right) \left[ \frac{1 - \exp\left(-\frac{d_{ov}}{\lambda_{ov} \sin \theta}\right)}{\exp\left(-\frac{d_{ov}}{\lambda_{sub} \sin \theta}\right)} \right]. \quad (4.1)$$

In Equation (4.1),  $I_{ov}$  and  $I_{sub}$  indicate integrated peak areas of the element of interest in the overlayer and substrate, respectively.  $SF_{ov}$  and  $SF_{sub}$  are the instrument sensitivity factors (0.2780 for C  $1s$ , 0.4453 for S  $2p$ , and 0.2634 for Ga  $3d$ ).  $\rho_{ov}$  and  $\rho_{sub}$  are the molar densities of the atoms in the overlayer and the substrate, respectively. The molar densities of C and S atoms in the overlayer were estimated from the density of adventitious hydrocarbon ( $3.3 \times 10^{-10}$  mol/cm<sup>3</sup>)[101] and molten liquid sulfur (1.819 g/cm<sup>3</sup>), respectively. The molar density of Ga atoms in the substrate was calculated from the crystalline GaP density (4.14 g/cm<sup>3</sup>).  $d_{ov}$  is the thickness of the overlayer.  $\lambda_{ov}$  and  $\lambda_{sub}$  indicate escape depths of photoelectrons originating from the orbitals of the atoms of interest located in the overlayer and substrate, respectively. Finally,  $\theta$  is the take-off angle between the photoelectron detector and the sample surface (fixed at 45° in the current report).

The escape depths of photoelectrons through the molecular overlayers were approximated by an attenuation length ( $\lambda$ ) which is calculated using the following empirical equation: [100]

$$\lambda = 0.4a^{1.5}E^{0.5}, \quad (4.2)$$

where  $E$  is the kinetic energy of the photoelectron in eV and  $a$  is the diameter of the atoms in the monolayer in nm. The diameter of the atom in Equation (4.2) was calculated using Equation (4.3),

$$a = \left( \frac{A}{1000N_{av}\rho} \right)^{\frac{1}{3}}, \quad (4.3)$$

where  $A$  is atomic weight in g/mol,  $N_{av}$  is Avogadro's number in number/mol, and  $\rho$  is the density of the atom of interest in g/cm<sup>3</sup>. From the densities introduced above, the diameters of C, S, and Ga were calculated to be 0.256 nm, 0.308 nm, and 0.343 nm. Using these values, the escape

depths of Ga 3*d* photoelectrons through 1-propanethiol overlayers were calculated to be 2.688 nm in S and 2.035 in C, respectively. The escape depths of the S 2*p* and C 1*s* photoelectrons through the 1-propanethiol overlayer were calculated to be 2.551 and 1.841 nm, respectively.

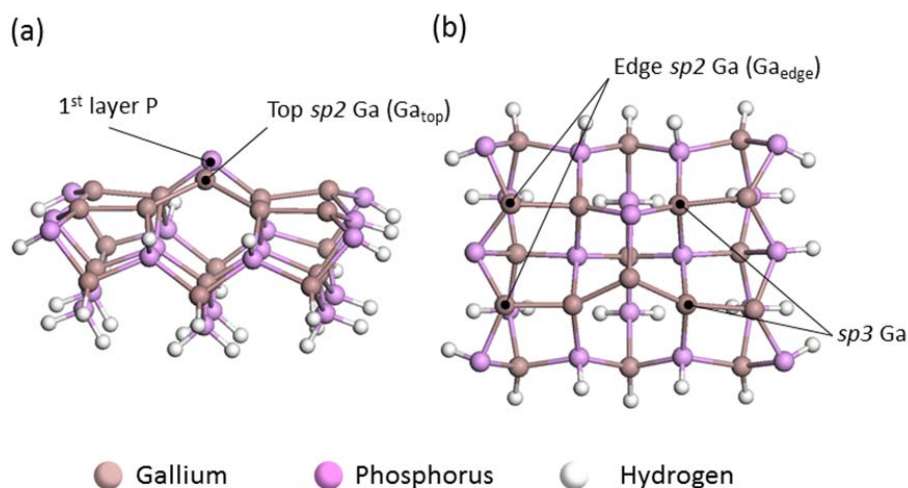


**Figure 4.1** a) Front and b) top view of the optimized Ga-rich GaP(001)(2×4) cluster model.

All density functional theory (DFT) calculations for the geometry optimization, the adsorption energy calculation, and the transition state search were performed by employing the JAGUAR 7.8 software package using the hybrid DFT method, including the Becke's three-parameter nonlocal-exchange functional with the correlation functional of Lee-Yang-Parr (B3LYP).[102] We constructed a Ga<sub>18</sub>P<sub>19</sub>H<sub>27</sub> cluster model to describe the GaP(001)(2×4) mixed-dimer surface reconstruction as shown in Figure 4.1. In the structure model, there is one Ga-P dimer in the first layer and four Ga-Ga dimers in the second layer. [44, 71] The Ga and P atoms below the second level were constructed to maintain four covalent networks on each atom using H atoms and lone pairs of electrons. The number of the H atoms was carefully chosen to satisfy the electron counting model[50]. Thereby, the P atom in the first layer has one completely filled dangling bond (two electrons in the orbital), and each of the five *sp*<sup>2</sup> Ga atoms on the first and second layers has an empty dangling bond (no electron in the orbital).

All calculations were carried out at the B3LYP/LACVP\*\* level of theory. The LACVP\*\* basis set is a mixed basis set that uses the LACVP basis set for the Ga atom and the 6-

31G basis set for the remaining atoms.[103] All structures were fully optimized without geometrical constraints on any atom in the cluster model. The optimized ground state and transition state structures were verified through frequency calculations. The ground states had no imaginary frequency and the transition states had one imaginary frequency. The adsorption energy ( $E_{ads}$ ) of a molecule of interest adsorbed on the GaP(001)(2×4) surface was calculated by subtracting the sum of the energies of the molecule and the bare GaP(001)(2×4) cluster from the energy of the molecule-adsorbed GaP cluster,

$$E_{ads}(eV) = E(\text{molecule adsorbed on GaP}) - E(\text{GaP}) - E(\text{molecule}).$$

Simulated STM images were produced by using the software such as Vienna ab-initio simulation package (VASP) and p4vasp 5.5.2. The Ga-rich GaP(001)(2×4) mixed-dimer reconstruction model was constructed with reference to the method described in previous literature [104]. Simulated STM images were produced using the Tersoff-Hamman approach [105] which was implemented in VASP. The simulated STM images were finally visualized in the p4vasp 5.2.2 software.

## 4.3 Results and discussion

### 4.3.1 Scanning tunneling microscopy (STM)

Figure 4.2 displays constant current STM images of a clean Ga-rich GaP(001)(2×4) surface at sample bias voltage of  $-4$  V and set point current of 200 pA. In the large scale image in Figure 4.2a, the terrace is composed of a number of bright and dark rows which run along the  $[-110]$  direction, called the *dimer row* and *vacancy row*, respectively. The dimer row is composed of bright protrusions attributed to the P atom of the first layer Ga-P dimer in the (2×4) unit cell. The inter-protrusion distance along  $[-110]$  is not constant due to the irregularity of the directions of the Ga-P dimers with respect to their neighboring Ga-P dimers. That is, the STM image of Ga-P/Ga-P is dissimilar to those of Ga-P/P-Ga and P-Ga/Ga-P.

In the STM image of a clean surface, we also observe two kinds of structural defects compared to a perfect Ga-rich GaP(001)(2×4) mixed-dimer reconstruction; one is a point defect and the other is a line defect based on many measurements, these defects are different from the defect features which probably stem from adsorptions and incorporations of alien molecules such

as background water and hydrocarbon in the UHV chamber. The two defects are shown in the magnified images in Figure 4.2a. When more than two first layer Ga-P dimers exist in a  $(2 \times 4)$  unit cell, a point defect is formed as shown in the left inset of Figure 4.2a. The line defect is called a *domain boundary* (DB) which is created when two dimer rows which come from the north (blue arrow) and the south (red arrow) meet on the different surface unit cell as shown in the right inset of Figure 4.2a. These two defects satisfy the electron counting model in spite of structural disorder; thus, they do not create charge accumulation or depletion. However, the defects could play a role in physical barriers that block the molecular diffusion motion along the  $[-110]$  direction if we assume that the transport mechanism happens along the dimer or vacancy row.

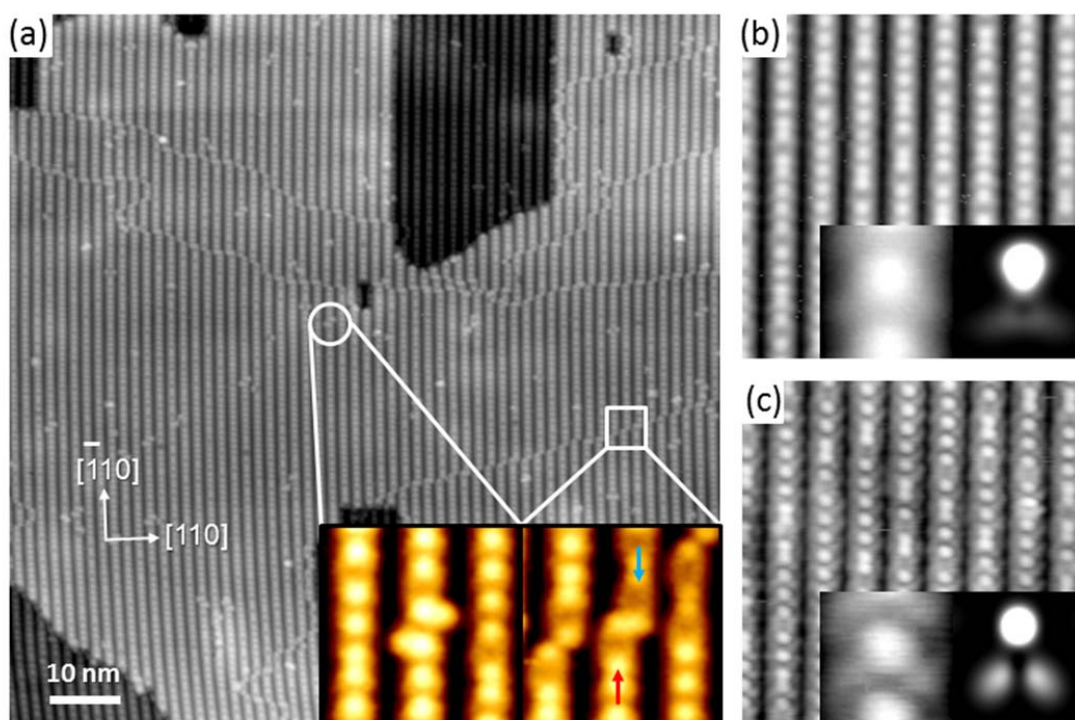


**Figure 4.2** a) Constant current STM images ( $V_s = -4$  V,  $I_t = 200$  pA) of a clean GaP(001)( $2 \times 4$ ) surface. (Insets represent high resolution STM images of two kinds of common defects (point defect and domain boundary “DB”, respectively). b), c) STM images obtained at  $-4.5$  V, 200 pA and  $-2.5$  V, 200 pA, respectively (image size  $15$  nm  $\times$   $15$  nm). Insets in b) and c) are zoom-in (left) and simulated (right) STM images. The sample bias voltages in the simulated STM images are b)  $-2.3$  V and c)  $-0.5$  V.

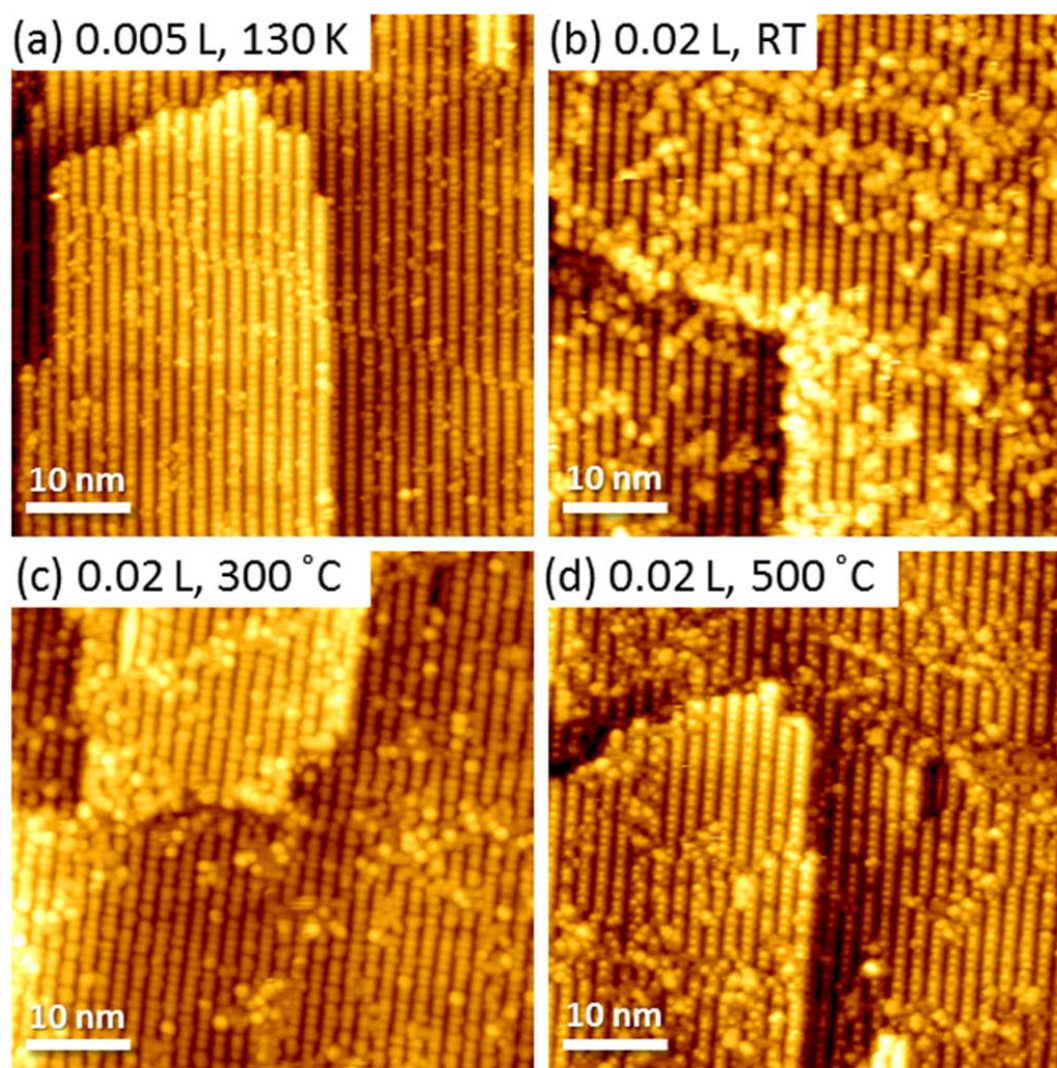
Figure 4.2b and c demonstrate the influence of the sample bias voltage on the STM images obtained from the same location. At constant set point current ( $I_t$ ), increasing the sample bias voltage ( $V_s$ ) by one volt varies the tip-sample distance by around 1 Å.[12] At a sample bias voltage of  $-4.5$  V in Figure 4.2b, the dangling bond in the 1<sup>st</sup> layer P is dominantly observed on both experimental and simulated STM images. The feature is also consistent with the electronic structure of the  $(2\times 4)$  reconstruction, since the highest occupied molecular orbital (HOMO) level is spatially localized at the dangling bond of the first layer P atom.[71] On the other hand, at  $-2.5$  V in Figure 4.2c, two less-bright protrusions are observed in addition to the strongest P-induced protrusion. These two less-bright protrusions are overlapped with the positions where the two back bonds of the first layer Ga atom are located. The second feature is also supported by the GaP(001) $(2\times 4)$  electronic structure. The second highest occupied molecular orbital occurs at the same location as the two less-bright protrusions.[71]

Figure 4.3 displays constant current STM images of 1-propanethiol/GaP(001) $(2\times 4)$  surfaces which are formed at various coverages and temperatures. At 130 K, 1-propanethiol molecules adsorb to the vacancy rows. In the high-resolution STM image in Figure 4.4a, the protrusion is not located in the center of the vacancy row but closer to one dimer row than the other. Another interesting point in the low temperature STM image is that the spatial distribution of the adsorption sites of the molecules is large; that is, the molecules adsorb to a random location of the surface.

The STM image in Figure 4.3b is obtained at RT. The shape and size of the STM feature at RT is significantly different from those of the feature observed at 130 K. The bright protrusion is larger than the low-temperature adsorbate, but the adsorption location on the  $(2\times 4)$  unit cell is almost the same as those shown in Figures 4.4b and c. Moreover, the adsorbates are not randomly distributed over the surface at RT, but instead form aggregated areas. In addition, the adsorbate density is higher around the step edge and DB.

Two new STM features are observed on the sample which was annealed at 300 °C (Figure 4.3c). One is a bright protrusion located on top of the dimer row (C in Figure 4.4d). The brightness of the other protrusion (feature D in Figure 4.4d) is not as strong as the feature C but similar to the first layer intact P atom. Lastly, there are two new features in the sample which was annealed at 500 °C, as shown in Figure 4.3d and 4.5a. One is the feature with  $(1\times 1)$  symmetry (feature E in the red square, Figure 4.5) which is less bright than the first layer P atom, and the other is an aggregation of bright protrusions (feature F in Figure 4.5). The STM image of the aggregated feature is different from the aggregated molecules in Figure 4.3b since we can

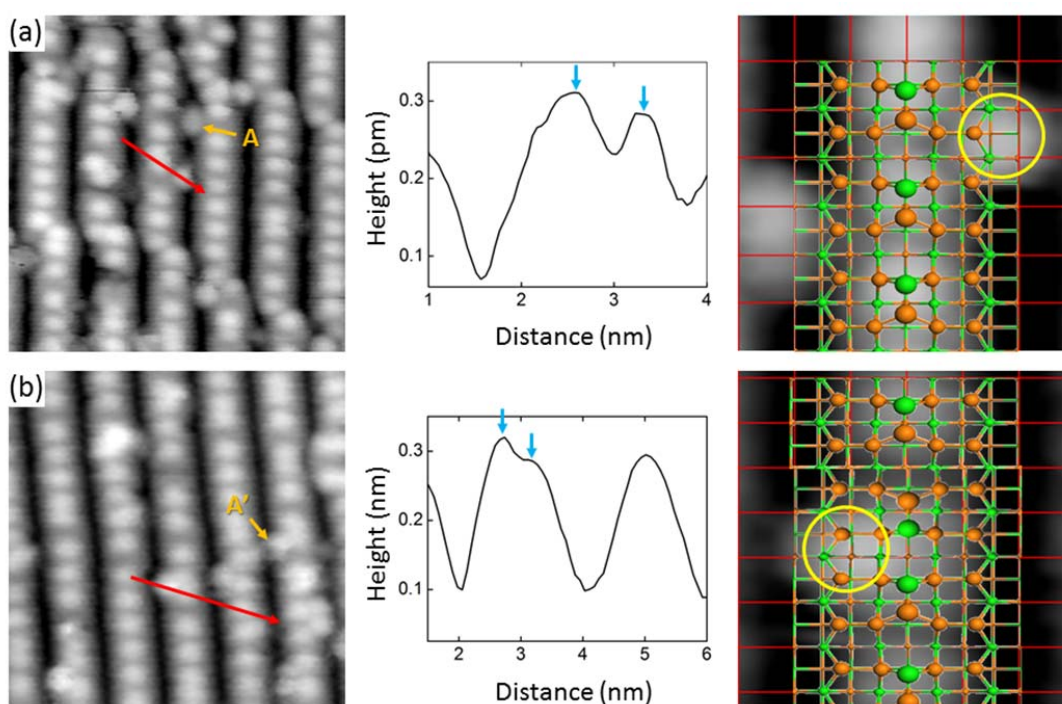
discriminate one molecule from the other molecule due to the clear boundary of feature B. However, for feature F, we cannot resolve one atom or molecule from another.



**Figure 4.3** Constant current STM images ( $V_s = -4$  V,  $I_t = 100$  pA). a) A clean GaP(001)(2 $\times$ 4) is exposed to 0.005 L 1-propanethiol at 130 K. b) A clean GaP(001)(2 $\times$ 4) is exposed to 0.02 L 1-propanethiol at 130 K followed by annealing at RT. c) The sample in b) is annealed at c) 300 °C and d) 500 °C for 30minutes, respectively. a) is measured at 130 K. b) to d) are measured at RT.

Figure 4.4 shows constant current STM images, cross-section line profiles, and high-magnification images on which the  $(1\times 1)$  unit cell grids and clean surface structural models are overlapped. The apparent height of feature A in Figure 4.4a is 28 pm lower than the first layer P atom. In addition, the adsorption location of the feature A overlaps with location of the edge  $sp^2$  Ga atoms (refer to Figure 4.1) in the  $(2\times 4)$  unit cell as marked with a yellow circle in Figure 4.4a.

The feature A' in Figure 4.4b is observed in the same sample at the same temperature where Figure 4.4a was obtained. Based on the number and coverage of the features, we find that feature A' stems from the same adsorbate as feature A in Figure 4.4a. We also observe the tip-induced transition from feature A to A' in successive images (not shown here). However, the adsorption location and apparent height of the protrusion of feature A' is slightly different from those of feature A. The apparent height of feature A' is 31 pm higher than the 1<sup>st</sup> layer P atom while that of feature A is lower than the first layer P atom. In addition, the adsorption location is slightly closer to the center line of the dimer row than feature A.



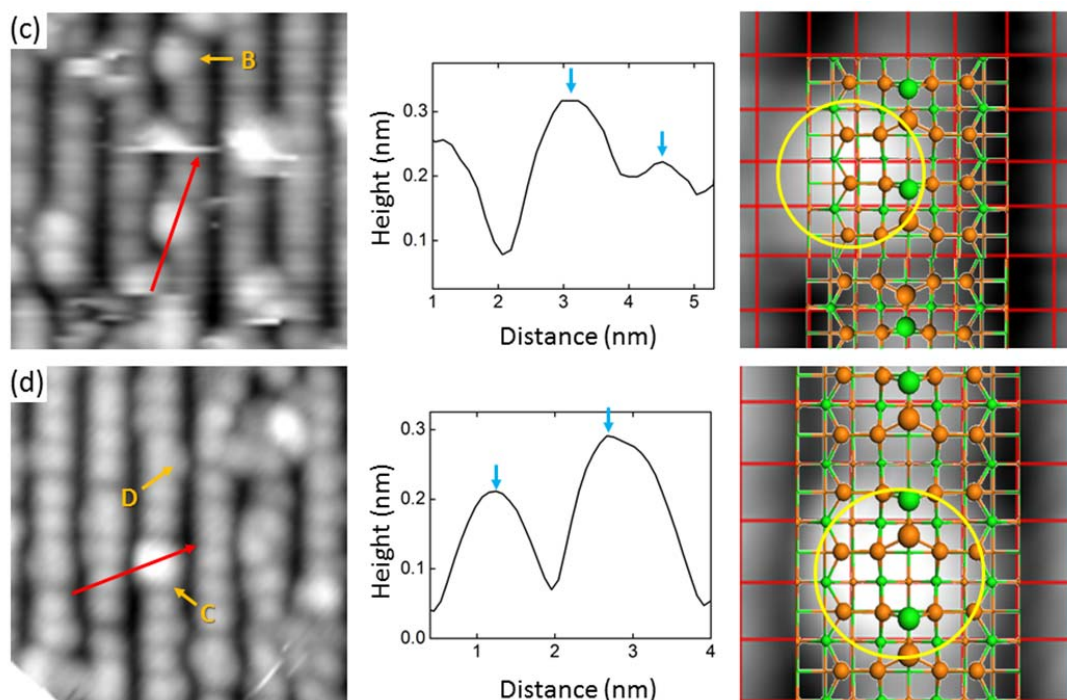


**Figure 4.4** (1<sup>st</sup> column) Constant current STM image ( $V_s = -4.5$  V,  $I_t = 100$  pA,  $10$  nm  $\times$   $10$  nm), (2<sup>nd</sup> column) cross-section line profile along the red arrow on the left image, and (3<sup>rd</sup> column) schematic model on the high magnification STM image of the protrusion A in the 1<sup>st</sup> column image. a), b) A clean GaP(001)( $2 \times 4$ ) surface is exposed to  $0.005$  L 1-propanethiol at  $130$  K. The images are obtained at  $130$  K.  $0.02$  L 1-propanethiol is dosed on a clean GaP(001)( $2 \times 4$ ) surface followed by annealing at c) RT and d)  $300$  °C. The peak-to-peak height differences marked as blue arrows in the 2<sup>nd</sup> column are  $28$ ,  $31$ ,  $95$ , and  $78$  pm, respectively. The yellow circle helps determine the center locations of the bright protrusions with respect to the grids. Green and orange spheres represent P and Ga atoms, respectively.

In Figure 4.4c, a new feature (feature B) is observed in the STM image which was obtained from the  $0.005$  L 1-propanethiol/GaP(001)( $2 \times 4$ ) sample at RT. The adsorption location of the feature B is similar to that of the feature A' in Figure 4.4b. However, the apparent height and size are significantly different from those of feature A'. The apparent peak height of feature B is  $95$  pm which is three times larger than that of feature A'. The diameter of feature B is  $2.1 \sim 2.9$  times larger than that of the surface ( $1 \times 1$ ) unit cell. The molecular length of 1-propanethiol from the center of the S atom to the center of C3 atom is  $4.18$  Å [106]. Thus, the diameter of the feature B is around 2.3 times the S-C3 length of the 1-propanethiol molecule. We propose the increased size of feature B compared with feature A' can be attributed to conformation change of the adsorbate due to temperature. Although the conformation change produces larger STM

feature in Figure 4.4c, locations of the centers of both features (A' and B) are almost same, which is the edge *sp*<sup>2</sup> Ga atom.

In Figure 4.4d, two new features (C and D) are discovered on the 0.02 L 1-propanethiol/GaP(001)(2×4) sample which is annealed at 300 °C. Feature C has a similar apparent size as feature B; however, the apparent height is slightly smaller than that of feature B. The critical difference between features B and C is the adsorption location. The center of feature C is located nearly on top of the center line of the dimer row, but the center of feature B is located on top of the edge *sp*<sup>2</sup> Ga atom. Feature D is the least clear feature observed in our STM images, appearing only with very sharp STM tips. In the STM image, the location of feature D is overlapped with that of the edge *sp*<sup>2</sup> Ga atoms, although boundary of the protrusion is not so clear.

Figure 4.5 shows an STM image of the 0.02 L 1-propanethiol/GaP(001)(2×4) followed by annealing at 500 °C for 30 min. Two new features (E and F) are observed. Feature E is composed of small protrusions which form (1×1) symmetry as marked with a red square in Figure 4.5a. We also observed (2×1) symmetry of the feature with the same apparent height and size on similarly prepared samples (not shown here). In contrast to feature E, the shape of feature F is irregular with no periodicity and ~ 50 pm higher than the first layer P atom in terms of their apparent heights.

To better understand the STM images of 1-propanethiol adsorbates, we investigated adsorption structures of other organosulfur molecules including 1-octanethiol, 1-pentanethiol, dipropyl disulfide, and 1,2-ethanedithiol (red arrows in Figure 4.6). Each molecule is dosed at 120 ~ 130 K on the clean GaP(001)(2×4) surfaces, which are prepared in the same way, followed by STM measurements at the dosing temperatures. The molecules are selected to determine the effects of 1) the alkyl chain length, 2) the number of the SH groups, and 3) the H atom of the SH group on the chemistry and adsorption geometries of organosulfur molecules on the surface. Figure 4.6 shows STM images of various organosulfur molecules adsorbed on the GaP(001)(2×4) surfaces at different coverages and temperatures. Surprisingly, at this cryogenic temperature, the STM features of each chemical are very similar to each other in spite of large variations in the length of the molecules and number/position of the S atoms. Moreover, the sizes of protrusions are not correlated with the alkyl chain lengths of various probe molecules. This implies that the features detected in STM images at these temperatures are associated with the S atoms of the molecules rather than alkyl chains. This assignment is also consistent with the spatial distribution

of HOMO and LUMO levels in an alkanethiol molecule, which are located on the S atom of alkanethiol; hence, the S atom is appeared brighter than alkyl chain in STM images.[107]

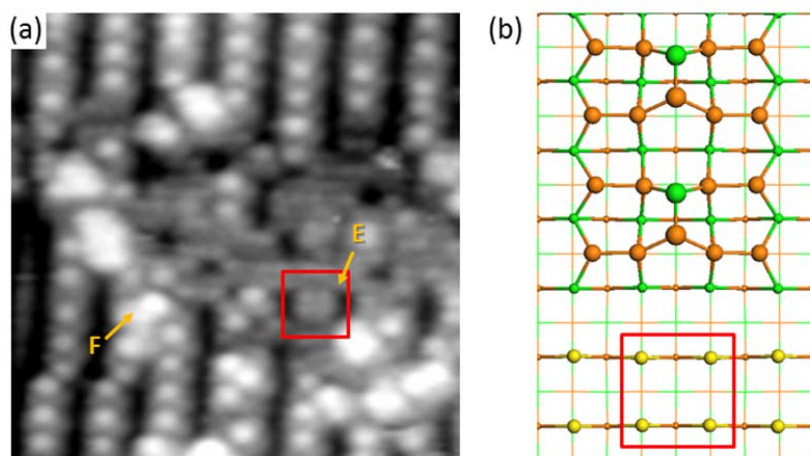


**Figure 4.5** a) Constant current STM image ( $V_s = -4.5$  V,  $I_t = 100$  pA,  $12.5$  nm  $\times$   $12.5$  nm) of the GaP(001)( $2 \times 4$ ) surface which is exposed to  $0.02$  L 1-propanethiol at  $130$  K followed by annealing at  $400$  °C for  $30$  minutes. The image is obtained at RT. b) Schematic model representing S-induced ( $1 \times 1$ ) reconstruction in the 3<sup>rd</sup> layer (marked by red square). Green, orange, and yellow spheres represent P, Ga, and S atoms, respectively.

We compare the STM images of three different thiol molecules such as 1-propanethiol, 1-pentanethiol, and 1-octanethiol as shown in Figure 4.4a and Figures 4.6a and b, respectively. We find that the alkyl chains are not detected as bright features in the current STM images, in contrast to the STM images of flat-lying physisorbed alkanethiols on a gold surface where the thiol group and hydrocarbon chain look like a bright sphere and a less bright zig-zag chain (or rod), respectively.[107] The imaging condition in that report was a sample bias voltage of  $2$  V and a set point current of  $200$  pA, which allow the tip-sample distance to be more than  $2$  Å closer than the current imaging condition, based on simple calculation.[12] Unfortunately, achieving an STM image on the GaP surface at the cryogenic temperature requires lower than  $-4$  V of the sample bias voltage. Therefore, this greater tip-sample distance is likely to be the main reason why the hydrocarbon chain is not detected in the current STM images. However, we find the trace of the alkyl chain in the STM image obtained from the 1-octanethiol/GaP(001) surface. The alkyl-chain-induced feature looks dark (but not as dark as the vacancy row) and is located next to a bright protrusion as indicated by the blue arrow in Figure 4.6b.

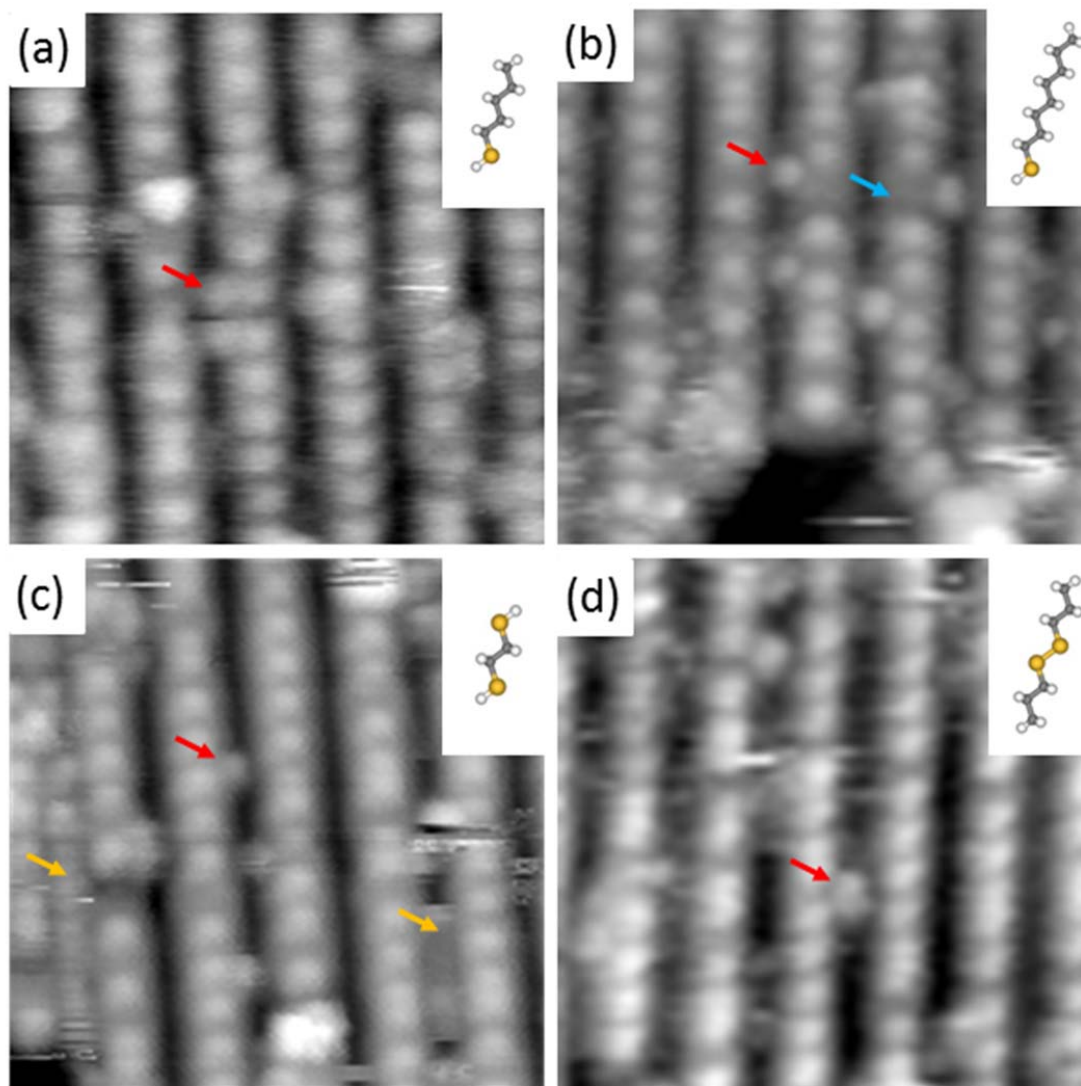


**Figure 4.6** Constant current STM images of various organosulfur molecules exposed to clean GaP(001)( $2 \times 4$ ) surfaces at various temperatures with various coverages. a) 0.001L pentanethiol at 130 K ( $V_s = -4$  V,  $I_t = 80$  pA), b) 0.01L 1-octanethiol at 130 K ( $V_s = -4$  V,  $I_t = 150$  pA), c) 0.012L 1,2-ethanedithiol at 130 K ( $V_s = -4.8$  V,  $I_t = 150$  pA), and d) 0.003L 1-dipropanedithiol at 121 K ( $V_s = -5.2$  V,  $I_t = 100$  pA). Images are obtained at the same temperatures as those at which each molecule is dosed. The size of each image is  $10 \text{ nm} \times 10 \text{ nm}$ .

This dark feature results from suppression of electron density on the first layer P atom rather than the missing first layer P atom since 1) the apparent height of the dark feature is higher than the missing atom defect site and 2) the number of dark features is much higher than the

average number of missing atom defect sites which are created by the sputtering-annealing procedure. Darkening of the STM image could occur if an H atom bonds with P to produce a P-H bond.[108-110] If true, the dark feature would be observed on the 1-propanethiol and 1-pentanethiol/GaP surfaces because the H-S dissociation is expected to be higher in shorter alkyl chain thiols. However, we did not observe as many dark features in the former two cases as in the 1-octanethiol/GaP case despite the similar number of bright protrusions. That is, there is no correlation between the number of bright protrusions and that of dark sites in 1-propanethiol and 1-pentanethiol/GaP(001). Thus, the dark feature is not associated with the P-H bond. Instead, we propose that the dark feature stems from the interruption of electron tunneling by the long hydrocarbon chain which is located on top of the first layer P atom. This hydrocarbon chain is likely to play a role in the insulating layer which increases the potential barrier for the tunneling electrons.

The 1,2-ethanedithiol molecule contains two S atoms separated by 4.5 Å in a fully relaxed model[106]. However, we could not obtain an STM image resolving the two S atoms of one molecule with the current imaging condition as shown in Figure 4.6c. Therefore, we assume that the STM features of the two S atoms are merged together to appear as one single protrusion. This assumption is made after excluding the upright adsorption geometry, where one of thiol groups interacts with the surface Ga atom and the other thiol group does not. In the upright adsorption geometry, the apparent height in the STM image is expected to be higher than the first layer P atom due to the height of the molecule, and this has not been observed in the STM images. Thus, the molecule has a flat-lying geometry.

We have discovered another intriguing characteristic of the 1,2-ethanedithiol molecule on the GaP(001) surface from low temperature STM images, where the molecule has higher diffusivity and diffusion anisotropy on the GaP(001)(2×4) surface than other organosulfur molecules (marked as an orange arrow in Figure 4.6c). The ghost image on the vacancy dimer row is proposed to result from high mobility of the molecule along the [-110] direction, and is not observed in the 1-propanethiol/GaP system in spite of its lower molecular weight compared to 1,2-ethanedithiol. Thus we interpret high diffusivity as a property of molecules with two thiol groups. The two thiol groups play the role of legs, such that the molecule is able to move along the edge *sp*<sup>2</sup> Ga atoms as if by walking. A similar mechanism was discovered in the catechol/rutile TiO<sub>2</sub>(110) surface.[111] The catechol molecule contains two hydroxyl groups which are located on the neighboring C atoms of the benzene ring. These two hydroxyl groups act as legs of the molecule to enhance diffusion along 5-fold Ti binding sites. However, there are

significant differences between the catechol/TiO<sub>2</sub> and 1,2-ethanedithiol/GaP systems. The HO groups of the catechol molecule on the TiO<sub>2</sub> surface dissociates when it is bound to the surface, which is facilitated by two-fold O adatoms at the neighboring location. This O adatom plays the role of a Lewis base on the surface. On the other hand, the thiol group of the 1, 2-ethanedithiol molecule on the GaP surface does not dissociate since the activation barrier of the dissociation mechanism is too high due to lack of a Lewis base at the neighboring location. We will discuss the energetics of thiol dissociation in the DFT chapter later.

The dipropyl disulfide molecule also has two S atoms which are separated by 2.1 Å as shown in Figure 4.6d [106]. As in the case of 1,2-ethanedithiol/GaP(001), the two S atoms in the dipropyl disulfide molecule are not resolved in the current STM condition. The one bright protrusion in Figure 4.6d is attributed to either a molecular dipropyl disulfide or dissociated propyl thiolate. We propose this protrusion is attributed to a molecular dipropyl disulfide bound to the edge *sp*<sup>2</sup> Ga atom because we observe a different STM feature on the dipropyl disulfide/GaP(001) sample at a higher temperature (130 K), which is proposed to be a propanethiolate adsorbate. Thus, the dissociation temperature of the disulfide bond is between 121 K and 130 K. Dissociation of the disulfide bond of dimethyl disulfide on the Ga-rich GaAs(001) surface is observed at 105 K in XPS and TPD experiment. [112] However, in dipropyl disulfide/GaP(001), the increase in dissociation temperature is likely due to the increased hydrocarbon chain length.

#### 4.3.2 X-ray photoelectron spectroscopy (XPS)

Figure 4.7 and Table 4.1 show fitted S *2p* core-level spectra and Ga *3d*, S *2p*, and C *1s* XPS data of the GaP(001)(2×4) surface which is exposed to 1 × 10<sup>4</sup> L 1-propanethiol at RT followed by annealing at the displayed temperatures. In previous chapter, we dosed 1-propanethiol on the GaP surface at cryogenic temperature followed by annealing to RT to obtain the RT STM images. However, for the XPS experiments, we dosed 1-propanethiol on the surface at RT. We verified that the XPS spectrum of the sample prepared with the latter method was always same as that of one prepared with the former method. We need to expose the sample exposed to the source at RT to a several-fold greater dosage than its counterpart due to the low sticking coefficient of the molecule on the surface at RT.

We first confirm that no P  $2p$  core-level binding energy shift is detected in the 1-propanthiol/GaP(001)( $2\times 4$ ) samples at various coverages up to the saturation coverage (not shown here). Annealing temperature effect is also checked on the P  $2p$  region, but there is no meaningful variation on the shape of spectra from the samples annealed from RT to 500 °C with 100 °C intervals. This is consistent with previous reports where the S atom in thiol and H<sub>2</sub>S molecules do not directly bond to the P atom but to the metal atom on the metal-rich III-phosphide (001) surfaces.[98, 113]

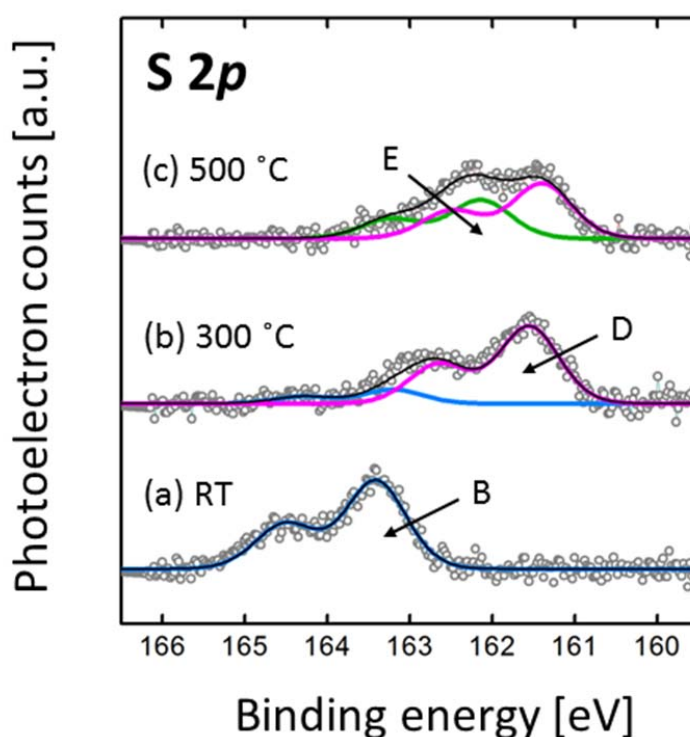


**Figure 4.7** Fitted X-ray photoelectron spectra of S  $2p$  and C  $1s$  regions. The Ga  $3s$  peak (160.2 eV) of the clean GaP(001)( $2\times 4$ ) is subtracted from the displayed spectra to show only the S  $2p$  core level. A clean GaP(001)( $2\times 4$ ) surface is exposed to  $1\times 10^4$  L 1-propanethiol, followed by annealing at displayed temperatures for 30 minutes. Data are obtained at RT after cooling the annealed samples. Blue, magenta, and green components are attributed to states B, D, and E in the S  $2p$  region.

Figure 4.7 presents the fitted XP spectra of the S  $2p$  region of 1-propanethiol/GaP(001) annealed at different temperatures. The spectra in Figure 4.7 are produced by subtracting the Ga  $3s$  peak of the clean GaP(001)( $2\times 4$ ) surface from the S  $2p$ /Ga  $3s$  regions of the 1-propanethiol/GaP(001)( $2\times 4$ ) samples to show only S  $2p$  core-level spectra. This is because there is a very strong Ga  $3s$  core-level peak with a binding energy of around 160.2 eV close to the S  $2p$  region in all 1-propanethiol/GaP(001) samples. Since the coverage of 1-propanethiol on the GaP surface is significantly low even at its saturation coverage (0.07 L in Table 4.1), we need this subtraction process to more clearly display the variation in the S  $2p$  region.

	Ga $3d_{5/2}$		S $2p_{3/2}$ (B)		S $2p_{3/2}$ (D)		S $2p_{3/2}$ (E)		C $1s$		Coverage	
	position (eV)	area* (count)	Sulfur	Carbon								
(a)	19.51	2548	163.4	162.0					285.6	946	0.07	0.32
(b)	19.46	2582	163.2	23.1	161.6	125.9			285.2	578	0.06	0.19
(c)	19.37	2870			161.4	86.9	162.1	61.1	284.6	237	0.06	0.07

**Table 4.1** XPS data of a) GaP(001)( $2\times 4$ ) exposed to  $1 \times 10^4$  L 1-propanethiol at RT followed by annealing at b) 300 °C and c) at 500 °C for 30 minutes, respectively. \* Integrated peak area is first subtracted by using Shirley background, and then scaled by background photoelectron count.

The S  $2p$  region is fitted with three discrete components throughout the measured annealing temperatures, as shown in Figure 4.7. This fitting is also verified by comparing the peak position of each component at various coverages (not shown here). The S  $2p$  core-level spectrum obtained at RT is fitted with only one component (B) as shown in Figure 4.7a. This component has the highest binding energy of the three components. Since the electronegativity of S (2.6) is higher than Ga (1.8), the S  $2p$  binding energy decrease as the strength and/or number of bonds between Ga and S is increased. Thus component B has the lowest interaction with surface Ga atoms among the three components.

The binding energy of the component D in Figure 4.7b has the lowest core-level binding energy of the three components ( $-1.6$  eV vs. B). The S  $2p$  binding energy of component D is the lowest because the state has the strongest interaction with the surface Ga atoms. Interestingly, the S coverage at 300 °C is similar to that at RT as shown in Table 4.1. On the other hand, the carbon

coverage is decreased significantly as the temperature of the 1-propanethiol/GaP surface is increased. Thus, the dominant process from RT to 300 °C is expected to be the dissociation of the S-C bond followed by desorption of hydrocarbon species, leaving S on the surface.

In the sample annealed at 500 °C, another component (E) is detected as well as component D. This new component E has a binding energy higher than component D (+ 0.7 eV) but lower than component B. We previously showed a featureless bright protrusion and a (1×1) reconstruction in STM images of the 1-propanethiol/GaP(001) sample which was annealed at 400 and 500 °C. Thus the two features are associated with the component E. There are many STM and low-energy electron diffraction (LEED) reports where formation of (1×1) and/or (1×2) reconstructions on the S-treated III-V semiconductor surfaces is followed by annealing. [99, 114, 115] In addition, previous XPS studies have shown two bonding states in the S 2*p* region from the S-treated III-V surfaces at similarly annealed samples.[114-117] The reported binding energy difference between the two components is 0.4 ~ 1.0 eV, which is consistent with our data where the difference is 0.7 eV.

The temperature dependent XPS study demonstrates that component D is dominant at 300 °C, but the higher binding energy component (E) is dominant at 500 °C. Table 4.1 shows the total S coverage is maintained when annealing from 300 °C to 500 °C. Thus, part of component D is transferred to E as annealing. Typically, annealing contributes an increase in interaction between S atoms and surface metal atoms by processes including alloying, incorporation, and so forth, which likely result in a red shift of S 2*p* core-level. However, several reports observed blue shifts from the S/III-V semiconductor surfaces when annealing. [114-117] In spite of common observations such as the blue shift as annealing, the interpretation is controversial, which therefore does not supply clear atomic structure models for the (1×1) and (2×1) reconstructions. However, analyzing the reconstructions is outside the scope of this report, so we do not propose accurate atomic models for those reconstructions. Instead, we note that our observations of the blue shift in S 2*p* core-level spectra and the (1×1) reconstruction in STM images agree with previous reports where the surface Ga-S-Ga bond is transferred to the S-incorporation as annealing.

In Table 4.1, we also observe significant loss of carbon coverage (0.07 ML) when annealing the sample from 300 °C to 500 °C. The carbon coverage at 500 °C is at a similar level to that of a clean GaP(110) sample which is cleaved in the UHV chamber (base pressure < 3 × 10<sup>-9</sup> Torr). Thus, the detected carbon in the sample annealed at 500 °C does not necessarily imply the

adsorbed 1-propanethiol is completely decomposed to form carbide, for example. The carbon peak could result from adsorption of adventitious carbon contaminants from the UHV chamber.

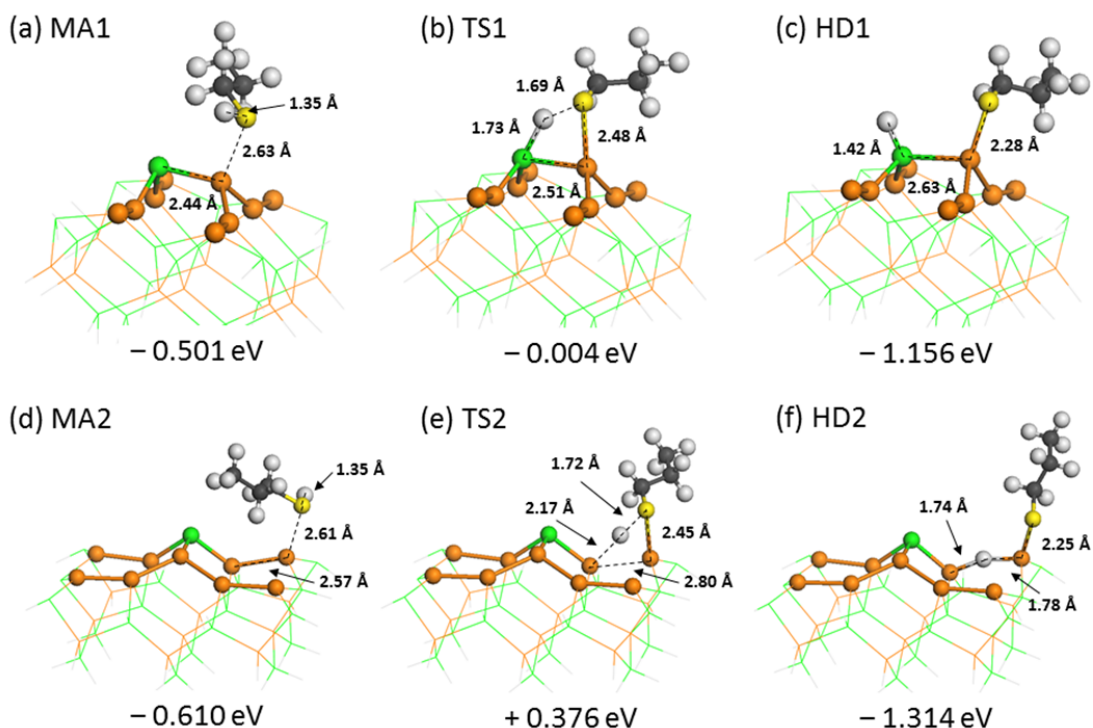


**Figure 4.8** Ground and transition state structures for 1-propanethiol adsorption on the top  $sp^2$  Ga atom a)-c) and edge  $sp^2$  Ga atom d)-f). a), d) Dative bonding state. b), e) Transition state for the H dissociation reaction. c), f) Ga-thiolate after H dissociation. The numbers in Å indicate the corresponding bond distances. The numbers below the models represent adsorption energies in units of eV. Green, orange, yellow, black, and white spheres represent P, Ga, S, C, and H atoms, respectively.

#### 4.3.3 Density functional theory (DFT) calculations

The adsorption structures and decomposition energetics of 1-propanethiol on the Ga-rich GaP(001)(2×4) mixed-dimer surface are investigated using the density functional theory (DFT) calculations. When a short alkane chain thiol molecule adsorbs onto a III-V semiconductor surface, molecular adsorption via the S-metal atom dative bond or H dissociative adsorption are proposed as the first step by several experimental and theoretical reports.[80, 93, 112, 118] Depending on the temperature and the H-S dissociation activation energy, the H dissociation by

an appropriate neighboring H acceptor is carried out simultaneously (dissociative adsorption)[118] or serially.[80]

We start with two dative bonding states as shown in Figures 4.8a and d followed by the most probable H dissociation pathways. In the first pathway (reaction 1; black lines in Figure 4.9), the 1-propanethiol bound to the top Ga atom dissociates and forms an H-P and a propanethiolate-Ga species. Since the P atom, which plays the role of a Lewis base, is located next to the top Ga atom, this pathway has relatively a low activation energy. On the other hand, in reaction 2, the H atom of the thiol group moves to the neighboring  $sp^3$  Ga atom, which finally forms a Ga-H-Ga bridge structure (reaction 2; red lines in Figure 4.9). The pathway in reaction 2 requires a higher activation energy but produces a lower product energy. Thus, reaction 1 is kinetically favorable, and reaction 2 is thermodynamically favorable. Simulation of the adsorption and decomposition reactions of 1-propanethiol on the edge  $sp^2$  Ga, which is located closer to the top Ga atom than the 1<sup>st</sup> layer P atom (in Figure 4.1), is excluded here since it is similar to reaction 2 except for a slight variation in the absolute energy values. That is, the activation and product energies for the H dissociation reaction of the 1-propanethiol adsorbed on that Ga atom are + 0.943 and - 1.202, respectively.

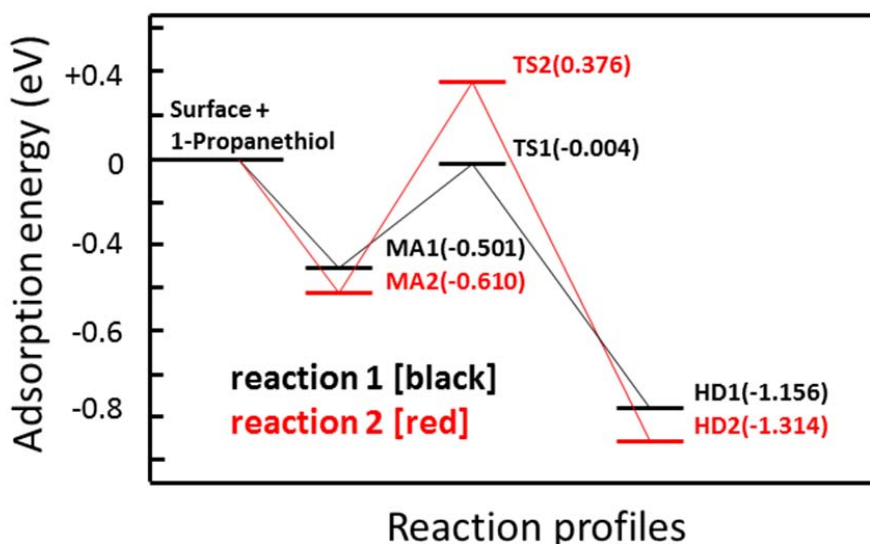


**Figure 4.9** Potential energy versus reaction profile plots for the 1-propanethiol adsorption and dissociation pathways on the top (black) and edge (red)  $sp^2$  Ga. Numbers in parenthesis refer to the adsorption energy of the corresponding structure in eV.

This result is supported by previous reports.[80, 119-121] Table 4.2 summarizes the energies of the transition and product states of various molecules and surfaces. Although there are some variations in the absolute values, the trends are the same throughout all of the systems. That is, the activation energy of reaction 2 is larger than that of reaction 1, but the ground state energy of the product in reaction 2 is lower than that of reaction 1. Thus, reaction 1 is kinetically more favorable but thermodynamically less favorable than reaction 2.

System	Reaction 1 $E_{a1}/E_{ads1}$	Reaction 2 $E_{a2}/E_{ads2}$	Tool	Reference
PH <sub>3</sub> In-rich InP(001)	0.993 / - 0.724	1.36 / - 0.885	Cluster model B3LYP/D95**	[119, 120]
AsH <sub>3</sub> Ga-rich GaAs(001)	0.716 / - 0.928	1.03 / - 0.984	Cluster model PW91/SD-ECP	[121]
1-propanethiol Ga-rich GaAs(001)	0.468 / - 1.24		Cluster model B3LYP/LANL2DZ	[80]
1-propanethiol Ga-rich GaP(001)	0.497 / - 1.16	0.986 / - 1.31	Cluster model B3LYP/LACVP**	Current result

**Table 4.2** Comparison of the simulation details.  $E_{a1}$  and  $E_{a2}$  represent the activation energies of the H dissociation reactions of the corresponding molecule adsorbed on the *sp*<sub>2</sub> metal atom of the group III – group V mixed-dimer and the group III – group III metal-dimer of the corresponding surfaces, respectively.  $E_{ads1}$  and  $E_{ads2}$  represent the adsorption energies of the products of the two H dissociation reactions. Unit of the displayed energy is eV.

Unfortunately, to the best of my knowledge, STM is not capable of directly observing complete H dissociation pathways, including transition states, since the H atom is too light and small to detect. We discovered from STM images taken at 130 K that feature A is located above the edge *sp*<sub>2</sub> Ga atom in the (2×4) unit cell. Thus, MA1 and HD1 in Figure 4.8 are excluded from consideration. Hence, we consider three models, which are MA2, HD2, and HD3 in Figure 4.8, and 4.10 to represent the feature A in Figure 4.4a. We exclude the HD3 model in spite of its higher stability (lowest adsorption energy) since we do not observe an STM image which supports the formation of the H-P bond.

We also cannot detect any STM feature induced by the Ga-H-Ga bond, which is not because there is no Ga-H-Ga bond but because H is again very difficult to detect using STM. The way researchers typically detect H is somewhat indirect. That is, one detects suppressed contrast in STM images after forming an H-surface atom bond where the surface atom originally looked

bright.[108-110] However, since the Ga-Ga dimer in the GaP(001)(2×4) surface looks dark in the filled-state STM images, adsorption of an H atom on the Ga-Ga dimer is not expected to change the STM contrast. A previous temperature programmed desorption spectroscopy (TPD or TDS) study proposed that the H atom of the thiol group of short chained alkanethiol molecules dissociates on the metal-rich III-V semiconductor surface below 100 K. Thus, it is likely that the observed feature A is assigned to the HD2-c3 state.[112]

A new question then arises; why is reaction 2 preferred over reaction 1 despite the significant activation energy? A similar issue was discussed in the PH<sub>3</sub>/InP(001) by Woo et al.[120] They explained this issue with reference to diffusion of PH<sub>2</sub> and H species. The H dissociation of H-PH<sub>2</sub> happens on the P-In dimer in a similar manner to reaction 1; and then the H and PH<sub>2</sub> species move to the thermodynamically more stable In-In dimer site to form an In-H-In bridge structure and an In-PH<sub>2</sub> adduct similar to the HD2 state.

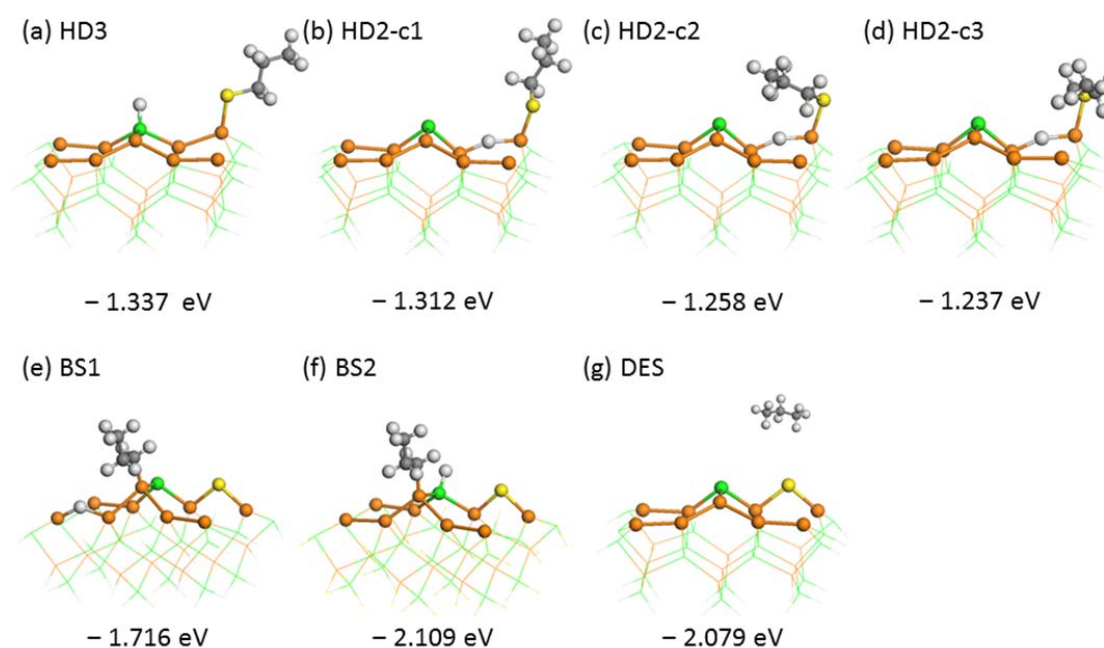


**Figure 4.10** a)-g) Optimized ground state structures of the 1-propanethiol/GaP(001)(2×4) surface. a)-d) H dissociation states. b)-d) Indicate structures with different conformation with the same bond configuration. e), f) Bridged S states. g) Propane desorption state. Green, orange, yellow, grey, and white spheres represent P, Ga, S, C, and H atoms, respectively. The numbers below the models represent the corresponding adsorption energies in eV.

We also observed a change in the STM feature from A to A' when we scanned the surface at bias voltages of  $-3.5\text{ V} \sim -4.5\text{ V}$ , as shown in Figures 4.4a and b (temperature maintained at 130 K). We propose that the change in the STM images is associated with a conformation change among the HD2 states. Figures 4.10b, c, and d show three different conformations with the same bond configuration. HD2-c2 and HD2-c3 explain features A' and A in the STM images especially well. The energy difference among the three conformations is within 75 meV, which could be overcome by the tunneling of electrons. In addition, the large protrusion of feature B, which maintains its center location as the same as that of feature A', could be explained by switching among the three conformations, such as HD2-c1, 2, and 3, by increased temperature and/or tunneling of electrons. The STM aspect of feature B is maintained from RT up to 200 °C.

We have observed that all five organosulfur molecules have similar STM features at liquid nitrogen cryogenic temperature (Figure 4.4a and Figure 4.6). Although there is a little variation in the size and shape of protrusions which are induced by the number of S atoms, all five molecules are proposed to be in a flat-lying geometry and located on top of the edge *sp*<sup>2</sup> Ga atoms. These observations are supported by previous STM studies. [122] When an alkanethiol molecule that is bonded through the S-surface atom has a flat-lying structure, the S atom displays bright contrast but the other alkyl chain is not detected. In addition, the brightness is not as bright as one would expect since tunneling electrons flow through only the S-surface atom bond. On the other hand, if a thiol molecule is in an upright geometry such as HD2-c1 in Figure 4.10b, tunneling electrons flow along the entire molecular backbone such that the molecule appears much brighter than its counterpart in the constant current STM image. In addition, the location of feature A is consistent with the S atom of structure HD2-c3.

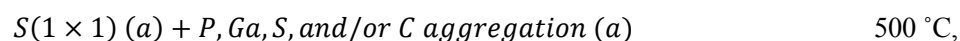
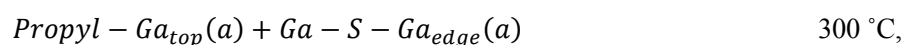
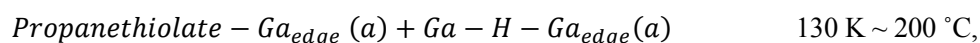
Now we move our focus from STM feature B (HD2-c3) to features C and D in Figure 4.4d. That is, the decomposition process of the thiolate adsorbate (feature B, HD2-c1 through c3) over 200 °C is discussed. At higher temperatures we saw two features from the STM images; an intense protrusion on the center line of the (2×4) unit cell (feature C) and a less intense protrusion near the edge *sp*<sup>2</sup> Ga atom (feature D) as shown in Figure 4.4d. Feature D is likely attributed to a bridged S configuration between the *sp*<sup>3</sup> Ga and edge *sp*<sup>2</sup> Ga atoms (Ga-S-Ga) based on the location and height of the protrusion. In addition, observation of the lowest binding energy component (D in Figure 4.7b) at 300 °C is consistent with the Ga-S-Ga feature.

Interpretation of Feature C in Figure 4.4d is somewhat controversial. Since the feature is located nearly on the center line of the  $(2\times 4)$  unit cell, it is likely that Feature C could be assigned as a propanethiolate or propyl bound to the first layer P (HD1 in Figure 4.8c) or the top Ga (BS1 or BS2 in Figure 4.10). However, since we observe 1) the S-dissociation product, such as the Ga-S-Ga configuration, and 2) no variation of the P  $2p$  core-level spectrum from RT to 500 °C, we propose that BS1 in Figure 4.10e is associated with Feature C. However, the adsorption energy based on DFT calculations could not completely explain this assignment since the BS1 state is not the most stable structure among the structures which are composed of propyl-X, H-X, and Ga-S-Ga (X = Ga or P) species. For instance the most stable structure is BS2 in Figure 4.10f. However, this could be explained by the possibility that both structures, BS1 and BS2, are not of the appropriate geometry for Feature C because the surface H atom desorbs at temperatures lower than 300 °C, based on previous literature results[87]. Further calculations for the structures excluding H- species are underway to explain this inconsistency.

Finally, we observed an S-induced  $(1\times 1)$  reconstruction (Feature E) in the STM images, as shown in Figure 4.5, once the sample was annealed at 500 °C. The locations of the bright protrusions in the  $(1\times 1)$  reconstruction are exactly matched by those of the third layer P atoms. Thus, we propose that these bright protrusions stem from the replacement of the third layer P by S. The  $(1\times 1)$  reconstruction areas are formed by removal of the first two layer atoms, such as 9 Ga and 1 P atoms. This is supported by the relocation or desorption of the Ga and P atoms which may accompany hydrocarbon desorption. Thus, the accumulation of featureless protrusions (Feature F) in Figure 4.5 can explain the relocation of Ga and P atoms. Lastly, the DES state in Figure 4.10g has a low enough energy to drive desorption of the propane molecule, leaving the S atom on the surface. Thus, the surface-bridged S (Ga-S-Ga) formation reaction from 1-propanethiol on the GaP(001) $(2\times 4)$  surface is an energetically favorable process.

### 3.4 Conclusion

In this chapter we studied the adsorption geometry and decomposition energetics of 1-propanethiol adsorbed on the Ga-rich GaP(001)(2×4) surface at the atomic level using STM, XPS, and DFT calculations. The following summarizes what we discovered both experimentally and theoretically under various temperature regimes:



where (a) and (g) imply adsorbate and gaseous states, respectively. We also investigated the adsorption geometries of other organosulfur molecules including 1-octanethiol, 1-pentanethiol, dipropyl disulfide, and 1, 2-ethanedithiol on the same surface at liquid nitrogen cryogenic temperatures. We discovered all the molecules have a flat-lying geometry, and their S atoms are located on the edge *sp*<sup>2</sup> Ga atoms. This study provides the detailed molecular structures of the thermal decomposition pathways of such species based on molecule-resolved STM images and DFT simulations. We expect this report to be of significant benefit to science and other technologies based on sub-molecular level understanding.

## Summary

The role of group III-V compound semiconductors in the semiconductor microelectronics industry has become significant since conventional group IV semiconductor materials are limited in performance in many applications, especially areas that require high power, high speed, and advanced optoelectronic properties in smaller device packages. The desirable electronic and optoelectronic properties of group III-V semiconductors have been proposed as solution to the limitations of group IV semiconductors. However, significant hurdles in applying III-V technologies to industrial areas still exist due to several undesirable properties of III-V semiconductors. One undesirable feature of many III-V materials is inferior surface passivation when compared with that of their group IV semiconductor counterparts. For example, one of the best ways to passivate the surface of GaAs to date is by forming epitaxial AlGaAs film on top of the GaAs, which is unfavorable in industry due to the relatively high cost of epitaxial processes. In addition to the surface passivation issue, there are many ways in which the chemical, electrical, and mechanical properties of the surfaces of III-V semiconductors might be developed, since their bulk properties are inherently excellent. Hence, major research and development is still required before these technologies can be successfully integrated.

It may be ideal and desirable to understand the relevant science of a material before application. At the very least, the author believes that science based on understanding has to be carried out in parallel with the development of a technology. Understanding the physics and chemistry of a material starts from its constitutional units such as atoms and molecules. Therefore, we focus on elucidating the atomic-level surface science of III-V materials in this dissertation. Regarding surfaces of III-V semiconductors, three systems have drawn the author's attention; inorganic epitaxial film growth, reaction with water, and organic functionalization/passivation. For better understanding of these systems, fundamental studies of interactions between the adsorbate molecules/atoms and the surface atoms were focused. We investigated the structures, chemistry, mechanisms, energetics, and electronics of such systems using several powerful surface analysis techniques such as scanning tunneling microscopy, X-ray photoelectron spectroscopy, and density functional theory calculations. The following summarizes the three research topics in this dissertation.

GaP is emerging as an important semiconductor for solid-state optoelectronics and photoelectrochemistry. The need to better understand the reaction of water on its surface is very significant since water is involved in almost every step of fabrication and processing. In addition, photo-induced conversion reactions of abundant and harmful carbon dioxide to valuable methanol in an aqueous solution was demonstrated previously,[7] but the water/GaP interface is not thoroughly understood. We explored all reasonable ground states involved in most of the possible adsorption and decomposition pathways in a single water molecule oxidation on the GaP(001)(2×4) surface using density functional theory calculations. Thus, our research elucidates structural and energetic information of every step in the water-induced GaP oxidation reactions, at the atomic level, in great detail. These results provide guidelines for experiments and theory to validate the key steps and to obtain kinetic data for modeling the oxidation processes.

Organosulfurs are very intriguing and useful molecules in that they have been researched significantly, especially with regard to immobilization of bio or chemical molecules or formation of self-assembly monolayers on metal and semiconductor surfaces. The organosulfur molecules play a role in not only chemical functionalization but also as electrical passivation materials on group III-V semiconductor surfaces. As the size of semiconductor-based devices is smaller, and nano and sub-nano fabrication technology is becoming significant, understanding the atomic level adsorption structure and their energetics are important. We elucidated adsorption geometries of 1-propanethiol as a function of annealing temperature. We obtained, for the first time, real-space single-molecule-resolved STM images of various organosulfur molecules on the Ga-rich GaP(001)(2×4) mixed-dimer surface at various temperatures. Adsorption geometries, chemistry, and energetics are thoroughly analyzed in collaboration with XPS and DFT calculations. Atomic-level structural and energetics information with experimental demonstration provides a clearer understanding of the organosulfur surface chemistry on the GaP surface.

Zn<sub>3</sub>P<sub>2</sub> is a promising semiconductor for inexpensive and efficient solar cells made from earth-abundant materials. A technology for growing high-quality, crystalline Zn<sub>3</sub>P<sub>2</sub> films using a GaAs substrate and the compound-source molecular beam epitaxy technique was demonstrated previously.[28] Before these technologies can develop, though, it will be necessary to develop an atomic-level understanding of this emerging material. We elucidated the chemistry, structure, and electronics of the surface and interface of the Zn<sub>3</sub>P<sub>2</sub>/GaAs(001) at the atomic level. We discovered that a P-rich amorphous layer covers the crystalline Zn<sub>3</sub>P<sub>2</sub> film during and after

growth. We also found that more accurate structural and electronic properties of the GaP interface between  $\text{Zn}_3\text{P}_2$  and GaAs, which had been anticipated in previous literature but has not been thoroughly characterized before. The information that our research provides is important and useful for the design of additional fabrication and processing steps in order to apply this material to a real device.

The major tool in this dissertation is a high-resolution, ultra-high vacuum scanning tunneling microscope. This tool requires significant commitment and patience to achieve a sub-molecular level resolution since high-resolution operation depends on the atomic-level sharpness of the apex of an STM probe, which cannot be controlled using known technology to date. Moreover, scanning the Ga-rich GaP or GaAs surface with large bias voltages often gives rise to probe contamination due to the low melting point of Ga (29.8 °C). Thus, successful imaging of single-molecule features on such surfaces is very challenging. However, STM is a unique and powerful tool for obtaining three dimensional and real-space views of a single atom/molecule on a solid surface. We expect the structural, chemical, electronic, and energetic information about various organic/inorganic adsorbates to be a useful reference for III-V semiconductor surface science research.

## Bibliography

1. *Electronic archive, New Semiconductor Materials. Characteristics and Properties. Physical Properties of Semiconductors.* [cited 2013 June 23]; Available from: <http://www.ioffe.ru/SVA/NSM/Semicond/GaAs/index.html>.
2. Powell, C.J., *The Surface Sensitivity of Electron Spectroscopies - a Citation Classic Commentary on Attenuation Lengths of Low-Energy Electrons in Solids.* Current Contents/Engineering Technology & Applied Sciences, 1990(3): p. 14-14.
3. Khaselev, O. and J.A. Turner, *A Monolithic Photovoltaic-Photoelectrochemical Device for Hydrogen Production via Water Splitting.* Science, 1998. **280**(5362): p. 425-427.
4. Tamboli, A.C., et al., *Conformal GaP Layers on Si wire Arrays for Solar Energy Applications.* Applied Physics Letters, 2010. **97**(22).
5. Kroemer, H., K.J. Polasko, and S.C. Wright, *On the (110) Orientation as the Preferred Orientation for the Molecular-Beam Epitaxial-Growth of Gaas on Ge, Gap on Si, and Similar Zinblende-on-Diamond Systems.* Applied Physics Letters, 1980. **36**(9): p. 763-765.
6. Halmann, M., *Photoelectrochemical Reduction of Aqueous Carbon-Dioxide on P-Type Gallium-Phosphide in Liquid Junction Solar-Cells.* Nature, 1978. **275**(5676): p. 115-116.
7. Barton, E.E., D.M. Rampulla, and A.B. Bocarsly, *Selective solar-driven reduction of CO<sub>2</sub> to methanol using a catalyzed p-GaP based photoelectrochemical cell.* Journal of the American Chemical Society, 2008. **130**(20): p. 6342-+.
8. Tomkiewicz, M. and J.M. Woodall, *Photoassisted Electrolysis of Water by Visible Irradiation of a Para-Type Gallium-Phosphide Electrode.* Science, 1977. **196**(4293): p. 990-991.
9. Green, A.M. and W.E. Spicer, *Do We Need a New Methodology for Gaas Passivation.* Journal of Vacuum Science & Technology A-Vacuum Surfaces and Films, 1993. **11**(4): p. 1061-1069.
10. Bessolov, V.N. and M.V. Lebedev, *Chalcogenide passivation of III-V semiconductor surfaces.* Semiconductors, 1998. **32**(11): p. 1141-1156.
11. Takayanagi, K., et al., *Structural-Analysis of Si(111)-7x7 by Uhv-Transmission Electron-Diffraction and Microscopy.* Journal of Vacuum Science & Technology a-Vacuum Surfaces and Films, 1985. **3**(3): p. 1502-1506.
12. Chen, C.J., *Introduction to Scanning Tunneling Microscopy.* 2nd ed. 2008, New York: Oxford University Press.
13. Powell, C.J., *Inelastic Mean Free Paths and Attenuation Lengths of Low-Energy Electrons in Solids.* Scanning Electron Microscopy, 1984: p. 1649-1664.
14. Hamers, R.J., R.M. Tromp, and J.E. Demuth, *Surface Electronic-Structure of Si(111)-(7 X 7) Resolved in Real Space.* Physical Review Letters, 1986. **56**(18): p. 1972-1975.
15. Powell, C.J., *Attenuation Lengths of Low-Energy Electrons in Solids.* Surface Science, 1974. **44**(1): p. 29-46.
16. Kimball, G.M., et al., *Photoluminescence-based measurements of the energy gap and diffusion length of Zn<sub>3</sub>P<sub>2</sub>.* Applied Physics Letters, 2009. **95**: p. 112103.
17. Pawlikowski, J.M., *Absorption edge of Zn<sub>3</sub>P<sub>2</sub>.* Physical Review B, 1982. **26**(8): p. 4711.
18. Bhushan, M. and A. Catalano, *Polycrystalline Zn<sub>3</sub>P<sub>2</sub> Schottky barrier solar cells.* Applied Physics Letters, 1981. **38**(1): p. 39-41.

19. Wadia, C., A.P. Alivisatos, and D.M. Kammen, *Materials Availability Expands the Opportunity for Large-Scale Photovoltaics Deployment*. Environmental Science & Technology, 2009. **43**(6): p. 2072-2077.
20. Arsenault, C.J. and D.E. Brodie, *Electrical and Optical-Properties of Vacuum-Deposited Amorphous Zn<sub>3</sub>P<sub>2</sub> Thin-Films*. Canadian Journal of Physics, 1987. **65**(7): p. 756-759.
21. Babu, V.S. and P.R. Vaya, *Studies on Hot Wall Deposited Zn<sub>3</sub>P<sub>2</sub> Thin-Film Surfaces and Interfaces*. Applied Surface Science, 1989. **37**(3): p. 283-290.
22. Fuke, S., et al., *Substrate Effect on the Deposition of Zn<sub>3</sub>P<sub>2</sub> Thin-Films Prepared by a Hot-Wall Method*. Journal of Applied Physics, 1989. **65**(2): p. 564-566.
23. Suda, T., *Zinc Phosphide Thin-Films Grown by Plasma Assisted Vapor-Phase Deposition*. Journal of Crystal Growth, 1990. **99**(1-4): p. 625-629.
24. Suda, T., T. Kanno, and S. Kurita, *Properties of Zn<sub>3</sub>P<sub>2</sub> Thin-Films Grown by Ionized-Cluster Beam Deposition*. Japanese Journal of Applied Physics Part 2-Letters, 1983. **22**(12): p. L777-L779.
25. Kakishita, K., S. Ikeda, and T. Suda, *Zn<sub>3</sub>P<sub>2</sub> Epitaxial-Growth by MOCVD*. Journal of Crystal Growth, 1991. **115**(1-4): p. 793-797.
26. Suda, T. and K. Kakishita, *Epitaxial-Growth of Zinc Phosphide*. Journal of Applied Physics, 1992. **71**(6): p. 3039-3041.
27. Suda, T., et al., *N-type Zinc Phosphide Grown by Molecular Beam Epitaxy*. Applied Physics Letters, 1996. **69**(16): p. 2426-2428.
28. Bosco, J.P., et al., *Pseudomorphic growth and strain relaxation of  $\alpha$ -Zn<sub>3</sub>P<sub>2</sub> on GaAs(001) by molecular beam epitaxy*. Journal of Crystal Growth, 2013. **363**(0): p. 205-210.
29. Schoonmaker, R.C., A.R. Venkitaraman, and P.K. Lee, *The Vaporization of Zinc Phosphide*. Journal of Physical Chemistry, 1967. **71**(8): p. 2676-2683.
30. Kocan, P., A. Ohtake, and N. Koguchi, *Structural features of Ga-rich GaAs(001) surfaces: Scanning Tunneling Microscopy study*. Physical Review B, 2004. **70**(20).
31. Ohtake, A., *Structure and Composition of Ga-rich (6x6) Reconstructions on GaAs(001)*. Physical Review B, 2007. **75**(15).
32. Seino, K., W.G. Schmidt, and A. Ohtake, *Ga-rich GaAs(001) surface from ab initio calculations: Atomic structure of the (4 x 6) and (6 x 6) reconstructions*. Physical Review B, 2006. **73**(3).
33. Shiraishi, K., *A New Slab Model Approach for Electronic-Structure Calculation of Polar Semiconductor Surface*. Journal of the Physical Society of Japan, 1990. **59**(10): p. 3455-3458.
34. Jenichen, A., et al., *Nitrogen Substitutions in GaAs(001) Surfaces: Density-Functional Supercell Calculations of the Surface Stability*. Physica Status Solidi B-Basic Solid State Physics, 2005. **242**(14): p. 2820-2832.
35. Du, Y.L., et al., *Ab initio studies on atomic and electronic structures of black phosphorus*. Journal of Applied Physics, 2010. **107**(9).
36. Gonze, X. and J.-P. Michenaud, *First-principles study of As, Sb, and Bi electronic properties*. Physical Review B, 1990. **41**: p. 11827-11836.
37. Venables, J.A., G.D.T. Spiller, and M. Hanbucken, *Nucleation and Growth of Thin-Films*. Reports on Progress in Physics, 1984. **47**(4): p. 399-459.
38. Xue, Q.K., et al., *Initial stages of cubic GaN growth on the GaAs(001) surface studied by scanning tunneling microscopy*. Japanese Journal of Applied Physics Part 2-Letters, 1997. **36**(11B): p. L1486-L1489.
39. Arima, K., et al., *Scanning tunneling microscopy/spectroscopy observation of intrinsic hydrogenated amorphous silicon surface under light irradiation*. Surface Science, 2004. **572**(2-3): p. 449-458.

40. Venkateswaran, N., et al., *The influence of surface structure on the reaction of dimethylzinc on GaAs(100)*. Surface Science, 1996. **365**(1): p. 125-135.
41. Laurence, G., et al., *Adsorption-Desorption Studies of Zn on GaAs*. Surface Science, 1977. **68**(1): p. 190-203.
42. Yamaguchi, H. and Y. Horikoshi, *Surface-Structure Transitions on InAs(001) and GaAs(001) Surfaces*. Physical Review B, 1995. **51**(15): p. 9836-9854.
43. Wallart, X., *A combined RHEED and photoemission comparison of the GaP and InP(001) (2x4) surface reconstructions*. Surface Science, 2002. **506**(3): p. 203-212.
44. Schmidt, W.G., *III-V compound semiconductor (001) surfaces*. Applied Physics a-Materials Science & Processing, 2002. **75**(1): p. 89-99.
45. Frisch, A.M., et al., *(2x4) GaP(001) surface: Atomic structure and optical anisotropy*. Physical Review B, 1999. **60**(4): p. 2488-2494.
46. Li, C.H., et al., *Arsenic adsorption and exchange with phosphorus on indium phosphide (001)*. Physical Review B, 2002. **65**(20).
47. Chen, J.C., *Introduction to Scanning Tunneling Microscopy*. 2008, New York: Oxford University Press. 56.
48. Winn, D.L., et al., *Direct and indirect causes of Fermi level pinning at the SiO<sub>2</sub>/GaAs interface*. Journal of Chemical Physics, 2007. **126**(8).
49. Gallagher, M.C., R.H. Prince, and R.F. Willis, *On the Atomic-Structure and Electronic-Properties of Decapped GaAs(001)(2 X 4) Surfaces*. Surface Science, 1992. **275**(1-2): p. 31-40.
50. Pashley, M.D., *Electron Counting Model and Its Application to Island Structures on Molecular-Beam Epitaxy Grown GaAs(001) and ZnSe(001)*. Physical Review B, 1989. **40**(15): p. 10481-10487.
51. Rud, V.Y., et al., *Photosensitive structures based on ZnP<sub>2</sub> single crystals of monoclinic and tetragonal modifications: Fabrication and properties*. Semiconductors, 2009. **43**(7): p. 858-864.
52. Udron, D., et al., *Evidence of Chemical Disorder in Amorphous GaP*. Physica B, 1989. **158**(1-3): p. 625-626.
53. Kadotani, N., M. Shimomura, and Y. Fukuda, *Surface structure of phosphorus-terminated GaP(001)-(2x1)*. Physical Review B, 2004. **70**(16).
54. J. F. Moulder, W.F.S., P. E. Sobol, K. D. Bomben, and J. Chastain, *Handbook of X-ray Photoelectron Spectroscopy*. 1992, Minnesota: Physical Electronics.
55. Suzuki, Y., et al., *High-resolution XPS analysis of GaP(001), (111)A, and (111)B surfaces passivated by (NH<sub>4</sub>)<sub>2</sub>S-x solution*. Applied Surface Science, 2004. **235**(3): p. 260-266.
56. Beaudry, R., et al., *Photoreflectance study of phosphorus passivation of GaAs (001)*. Journal of Applied Physics, 2000. **87**(11): p. 7838-7844.
57. Kraut, E.A., et al., *Semiconductor Core-level to Valence-band Maximum Binding-energy Differences - Precise Determination by X-ray Photoelectron-spectroscopy*. Physical Review B, 1983. **28**(4): p. 1965-1977.
58. Bosco, J.P., et al., *Band alignment of epitaxial ZnS/Zn<sub>3</sub>P<sub>2</sub> heterojunctions*. Journal of Applied Physics, 2012. **112**(9): p. 093703.
59. Bosco, J.P., et al., *Energy-band alignment of II-VI/Zn<sub>3</sub>P<sub>2</sub> heterojunctions from x-ray photoemission spectroscopy*. (in preparation), 2013.
60. Recio, M., et al., *Optical-Properties of GaAs/Gap Strained-Layer Superlattices*. Journal of Applied Physics, 1990. **67**(4): p. 2044-2050.
61. Del Alamo, J.A., *Nanometre-scale electronics with III-V compound semiconductors*. Nature, 2011. **479**(7373): p. 317-323.

62. Khaselev, O. and J.A. Turner, *Electrochemical stability of p-GaInP<sub>2</sub> in aqueous electrolytes toward photoelectrochemical water splitting*. Journal of the Electrochemical Society, 1998. **145**(10): p. 3335-3339.
63. King, R.R., et al., *40% efficient metamorphic GaInP/GaInAs/Ge multijunction solar cells*. Applied Physics Letters, 2007. **90**(18).
64. Geisz, J.F., et al., *40.8% efficient inverted triple-junction solar cell with two independently metamorphic junctions*. Applied Physics Letters, 2008. **93**(12).
65. Guter, W., et al., *Current-matched triple-junction solar cell reaching 41.1% conversion efficiency under concentrated sunlight*. Applied Physics Letters, 2009. **94**(22).
66. Wood, B.C., T. Ogitsu, and E. Schwegler, *Ab initio modeling of water-semiconductor interfaces for photocatalytic water splitting: role of surface oxygen and hydroxyl*. Journal of Photonics for Energy, 2011. **1**.
67. Warschkow, O., et al., *Water on silicon (001): C defects and initial steps of surface oxidation*. Physical Review B, 2008. **77**(20).
68. Cho, J.H., et al., *Dissociative adsorption of water on the Si(001) surface: A first-principles study*. Physical Review B, 2000. **61**(7): p. 4503-4506.
69. Foraker, A. and D.J. Doren, *Dissociative adsorption of water on Ge(100)-(2 x 1): First-principles theory*. Journal of Physical Chemistry B, 2003. **107**(33): p. 8507-8510.
70. Cho, J.H., et al., *Theoretical study of water adsorption on the Ge(100) surface*. Physical Review B, 2002. **66**(11).
71. Schmidt, W.G., J. Bernholc, and F. Bechstedt, *(001) Surfaces of GaP and InP: structural motifs, electronic states and optical signatures*. Applied Surface Science, 2000. **166**(1-4): p. 179-184.
72. Sanada, N., et al., *The (2x4) and (2x1) structures of the clean GaP(001) surface*. Surface Science, 1999. **419**(2-3): p. 120-127.
73. Naitoh, M., et al., *A clean GaP(001)4x2/c(8x2) surface structure studied by scanning tunneling microscopy and ion scattering spectroscopy*. Japanese Journal of Applied Physics Part 1-Regular Papers Short Notes & Review Papers, 1996. **35**(9A): p. 4789-4790.
74. *Numerical Data and Functional Relationships in Science and Technology Landolt-Börnstein Group III*, ed. K.-H. Hellwege, Madelung, O. 1982: Springer, Verlag Berlin.
75. Li, D.F., et al., *First-principles study of GaP(001) surfaces*. Journal of Alloys and Compounds, 2007. **440**(1-2): p. 229-235.
76. Sloan, D.W., Y.M. Sun, and J.M. White, *Interaction of 50 eV electrons with D<sub>2</sub>O on GaAs(100)*. Journal of Vacuum Science & Technology A-Vacuum Surfaces and Films, 1996. **14**(1): p. 216-222.
77. Chung, C.H., S.I. Yi, and W.H. Weinberg, *Temperature-programmed desorption and high-resolution electron energy loss spectroscopy studies of the interaction of water with the GaAs(001)-(4x2) surface*. Journal of Vacuum Science & Technology A-Vacuum Surfaces and Films, 1998. **16**(3): p. 1785-1789.
78. Henrion, O., A. Klein, and W. Jaegermann, *Water adsorption on UHV cleaved InP(110) surfaces*. Surface Science, 2000. **457**(1-2): p. L337-L341.
79. Voznyy, O. and J.J. Dubowski, *Adsorption kinetics of hydrogen sulfide and thiols on GaAs (001) surfaces in a vacuum*. Journal of Physical Chemistry C, 2008. **112**(10): p. 3726-3733.
80. Tang, S.B. and Z.X. Cao, *Density Functional Characterization of Adsorption and Decomposition of 1-Propanethiol on the Ga-Rich GaAs (001) Surface*. Journal of Physical Chemistry A, 2009. **113**(19): p. 5685-5690.

81. Lu, H.L., et al., *DFT calculations of NH<sub>3</sub> adsorption and dissociation on gallium-rich GaAs(001)-4 x 2 surface*. Chemical Physics Letters, 2007. **445**(4-6): p. 188-192.
82. Kolasinski, K., *Surface Science. Foundation of Catalysis and Nanoscience*. 2002: John Wiley & Sons Ltd.
83. McCash, E.M., *Surface Chemistry*. 2001.
84. "Standard Thermodynamic Properties of Chemical Substances," in *CRC Handbook of Chemistry and Physics*. 92nd ed. 2012, Boca Raton: CRD Press/Taylor and Francis.
85. Henrion, O., et al., *Low temperature adsorption of water on cleaved GaAs(110) surfaces*. Surface Science, 1996. **366**(1): p. L685-L688.
86. *For details, refer to the Supporting Information of the following publication: Jeon S. et al., Journal of Physical Chemistry C, 2012, 116 (33), pp 17604-17612.*
87. Foord, J.S. and E.T. Fitzgerald, *The Adsorption and Thermal-Decomposition of Hydrogen-Sulfide on GaAs(100)*. Surface Science, 1994. **306**(1-2): p. 29-36.
88. Ulman, A., *Formation and structure of self-assembled monolayers*. Chemical Reviews, 1996. **96**(4): p. 1533-1554.
89. Love, J.C., et al., *Self-assembled monolayers of thiolates on metals as a form of nanotechnology*. Chemical Reviews, 2005. **105**(4): p. 1103-1169.
90. Schreiber, F., *Structure and growth of self-assembling monolayers*. Progress in Surface Science, 2000. **65**(5-8): p. 151-256.
91. Park, S.J., T.A. Taton, and C.A. Mirkin, *Array-based electrical detection of DNA with nanoparticle probes*. Science, 2002. **295**(5559): p. 1503-1506.
92. Spruell, J.M., et al., *Heterogeneous Catalysis through Microcontact Printing*. Angewandte Chemie-International Edition, 2008. **47**(51): p. 9927-9932.
93. Voznyy, O. and J.J. Dubowski, *Structure of Thiol Self-Assembled Monolayers Commensurate with the GaAs (001) Surface*. Langmuir, 2008. **24**(23): p. 13299-13305.
94. McGuinness, C.L., et al., *Molecular Self-Assembly at Bare Semiconductor Surfaces: Cooperative Substrate Molecule Effects in Octadecanethiolate Mono layer Assemblies on GaAs(111), (110), and (100)*. Acs Nano, 2010. **4**(6): p. 3447-3465.
95. McGuinness, C.L., et al., *Molecular self-assembly at bare semiconductor surfaces: Investigation of the chemical and electronic properties of the alkanethiolate-GaAs(001) interface*. Journal of Physical Chemistry C, 2007. **111**(11): p. 4226-4234.
96. McGuinness, C.L., et al., *Molecular self-assembly at bare semiconductor surfaces: Preparation and characterization of highly organized octadecanethiolate monolayers on GaAs(001)*. Journal of the American Chemical Society, 2006. **128**(15): p. 5231-5243.
97. Lunt, S.R., P.G. Santangelo, and N.S. Lewis, *Passivation of GaAs Surface Recombination with Organic Thiols*. Journal of Vacuum Science & Technology B, 1991. **9**(4): p. 2333-2336.
98. Flores-Perez, R., D.Y. Zernlyanov, and A. Ivanisevic, *Quantitative evaluation of covalently bound molecules on GaP (100) surfaces*. Journal of Physical Chemistry C, 2008. **112**(6): p. 2147-2155.
99. Sanada, N., et al., *Clean GaP(001)-(4x2) and H<sub>2</sub>S-Treated (1x2)S Surface-Structures Studied by Scanning-Tunneling-Microscopy*. Applied Physics Letters, 1995. **67**(10): p. 1432-1434.
100. Briggs, D., Seah, M. P., *Practical Surface Analysis: Auger and X-ray Photoelectron Spectroscopy*. 2nd ed. 1990, New York: Wiley.
101. Tufts, B.J., et al., *X-Ray Photoelectron Spectroscopic Studies of Interfacial Chemistry at N-Type Si Liquid Junctions*. Journal of Physical Chemistry, 1992. **96**(11): p. 4581-4592.

102. Lee, C.T., W.T. Yang, and R.G. Parr, *Development of the Colle-Salvetti Correlation-Energy Formula into a Functional of the Electron-Density*. Physical Review B, 1988. **37**(2): p. 785-789.
103. Wadt, W.R. and P.J. Hay, *Abinitio Effective Core Potentials for Molecular Calculations - Potentials for Main Group Elements Na to Bi*. Journal of Chemical Physics, 1985. **82**(1): p. 284-298.
104. Jeon, S., et al., *DFT Study of Water Adsorption and Decomposition on a Ga-Rich GaP(001)(2x4) Surface*. Journal of Physical Chemistry C, 2012. **116**(33): p. 17604-17612.
105. Tersoff, J. and D.R. Hamann, *Theory and Application for the Scanning Tunneling Microscope*. Physical Review Letters, 1983. **50**(25): p. 1998-2001.
106. Mikhal'chuk, V.M., et al., *Effect of reaction conditions on the structure of interpenetrating polymer networks. V. The influence of a high energy surface on curing of epoxy-allylic interpenetrating networks*. Polymer Networks & Blends, 1997. **7**(4): p. 133-137.
107. Staub, R., et al., *Flat lying pin-stripe phase of decanethiol self-assembled monolayers on Au(111)*. Langmuir, 1998. **14**(23): p. 6693-6698.
108. Li, L., et al., *Example of a compound semiconductor surface that mimics silicon: The InP(001)-(2x1) reconstruction*. Physical Review Letters, 1999. **82**(9): p. 1879-1882.
109. Hahn, P.H., et al., *P-rich GaP(001) (2x1)/(2x2) surface: A hydrogen-adsorbate structure determined from first-principles calculations*. Physical Review B, 2003. **68**(3).
110. Kleinschmidt, P., et al., *Direct observation of dimer flipping at the hydrogen-stabilized GaP(100) and InP(100) surfaces*. Physical Review B, 2011. **83**(15).
111. Li, S.C., et al., *Hydrogen Bonding Controls the Dynamics of Catechol Adsorbed on a TiO<sub>2</sub>(110) Surface*. Science, 2010. **328**(5980): p. 882-884.
112. Huang, T.P., et al., *Adsorption and thermal reaction of short-chain alkanethiols on GaAs(100)*. Surface Science, 2009. **603**(9): p. 1244-1252.
113. Shimomura, M., et al., *Adsorption of H<sub>2</sub>S on InP(001) studied by photoemission spectroscopy*. Applied Surface Science, 1997. **121**: p. 237-240.
114. Shimomura, M., et al., *Surface structures and electronic states of H<sub>2</sub>S-treated InP(001)*. Journal of Applied Physics, 1996. **79**(8): p. 4193-4196.
115. Shimomura, M., et al., *Surface reconstruction of InP(001) upon adsorption of H<sub>2</sub>S studied by low-energy electron diffraction, scanning tunneling microscopy, high-resolution electron energy loss, and x-ray photoelectron spectroscopies*. Journal of Applied Physics, 1998. **83**(6): p. 3071-3076.
116. Moriarty, P., et al., *Photoelectron Core-Level Spectroscopy and Scanning-Tunneling-Microscopy Study of the Sulfur-Treated GaAs(100) Surface*. Physical Review B, 1994. **50**(19): p. 14237-14245.
117. Preobrajenski, A.B., et al., *Two types of sulfur-induced (2 x 1) reconstructions on InP(001)*. Surface Science, 2001. **481**(1-3): p. 1-12.
118. Donev, S., et al., *Surface reactions of 1-propanethiol on GaAs(100)*. Langmuir, 2005. **21**(5): p. 1866-1874.
119. Das, U., et al., *Phosphine adsorption on the In-rich InP(001) surface: Evidence of surface dative bonds at room temperature*. Langmuir, 2007. **23**(20): p. 10109-10115.
120. Woo, R.L., et al., *Phosphine and tertiarybutylphosphine adsorption on the indium-rich InP (001)-(2 x 4) surface*. Surface Science, 2006. **600**(21): p. 4888-4895.
121. Fu, Q., et al., *Mechanism of arsine adsorption on the gallium-rich GaAs(001)-(4 x 2) surface*. Journal of Physical Chemistry B, 2000. **104**(23): p. 5595-5602.

122. Zhang, J.D., Q.J. Chi, and J. Ulstrup, *Assembly Dynamics and Detailed Structure of 1-Propanethiol Monolayers on Au(111) Surfaces Observed Real Time by in situ STM*. *Langmuir*, 2006. **22**(14): p. 6203-6213.

## Appendix

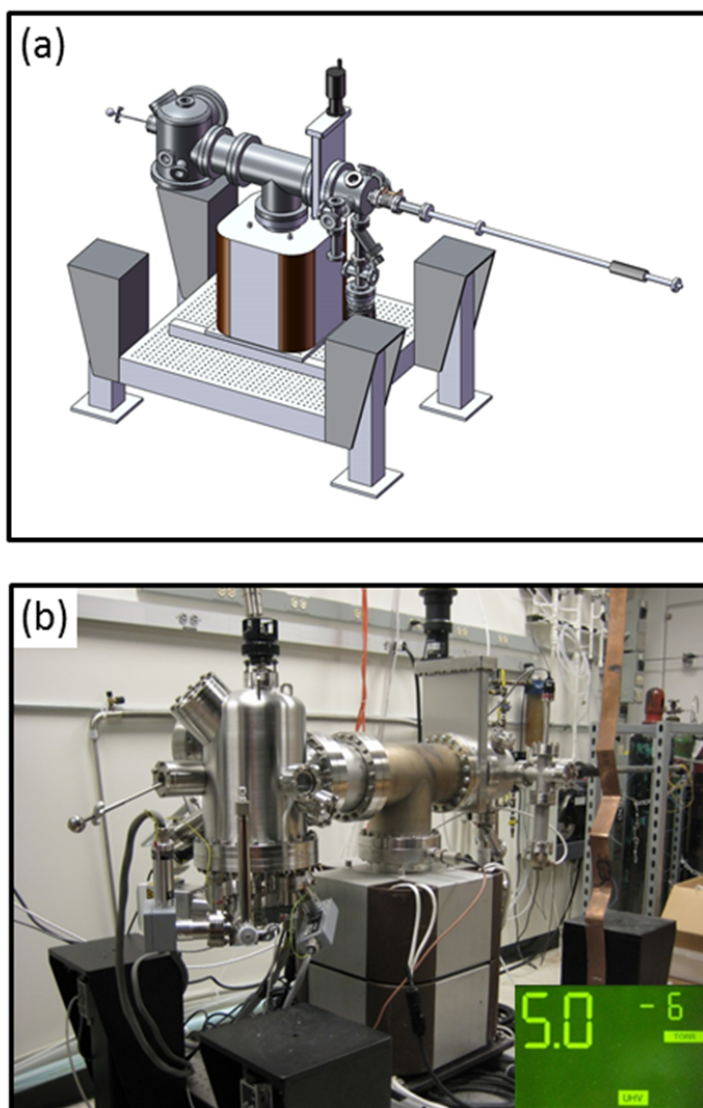


**Figure A.1** a) SolidWorks drawing and b) picture of the high vacuum (HV) chambers equipped with Omicron variable-temperature (VT) scanning tunneling microscope (STM) with a beam-deflection atomic force microscope (AFM) option in 249 Watson. The system was fabricated by a previous Atwater group member, Tao Feng. Picture b) was taken in April, 2008 when Seokmin Jeon became maintenance guru of the system. Inset in b) displays base pressure of the system in torr.

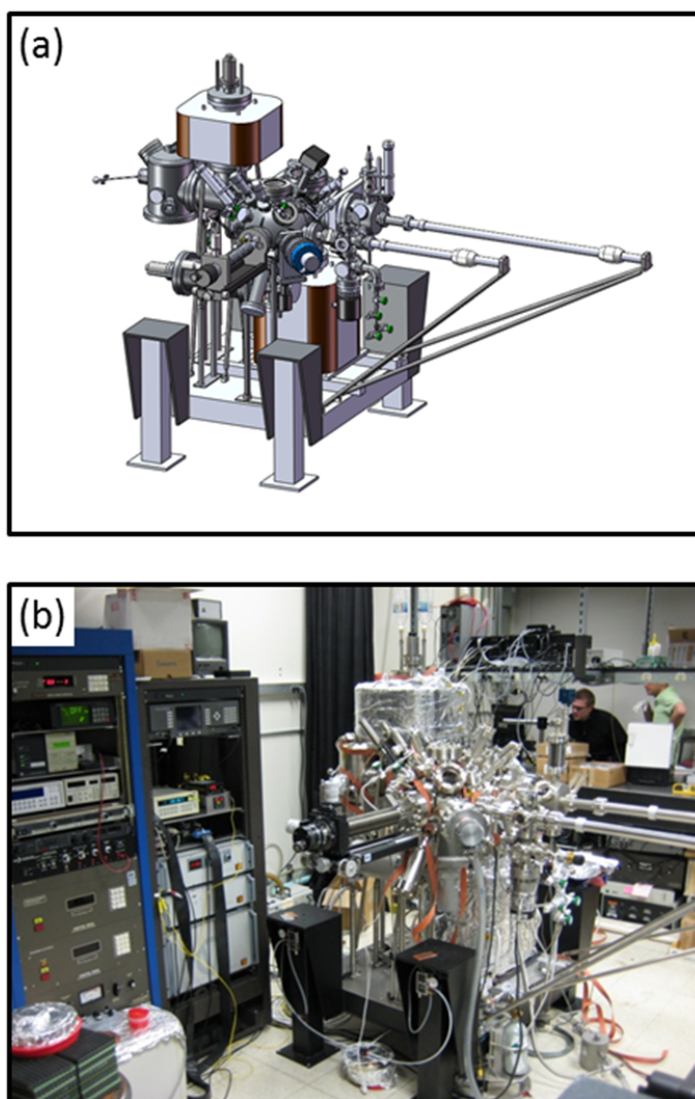


**Figure A.2** a) SolidWorks drawing, and b) picture of the ultra-high vacuum (UHV) chambers equipped with UHV sample preparation facilities including an Omicron PBN heater (max. 950 °C), an RBD ion gun, an Accufiber pyrometer (450 ~ 1200 °C), and Omicron VT STM with a beam-deflection AFM option in 249 Watson. The system was designed and assembled by Seokmin Jeon. Picture b) was taken in November, 2009.

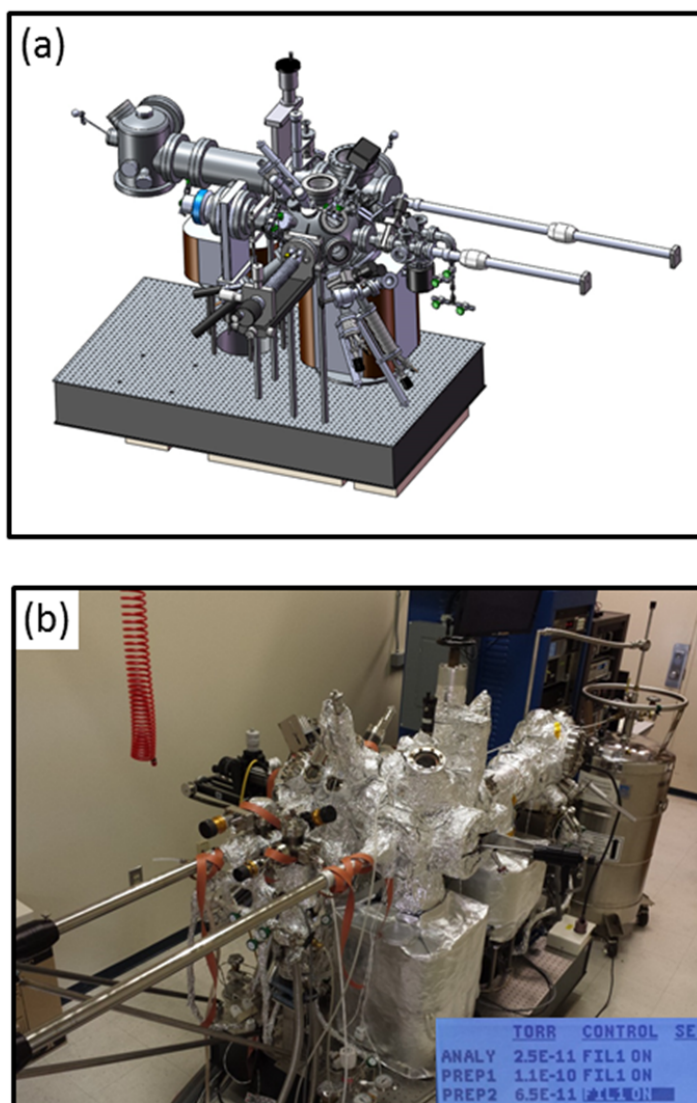


**Figure A.3** a) SolidWorks drawing, and b) picture of the UHV chambers equipped with Herzan active isolators, a Newport custom optical table, two custom effusion cells (Au and Cu loaded), a commercial effusion cell ( $Zn_3P_2$  loaded), a custom atomic hydrogen source, a Micro-Epsilon pyrometer (150 ~ 900 °C), an Omicron e-beam tip heater, UHV sample preparation facilities (details described in Figure A.2 caption), three gas dosers with flushing lines located on the load-lock, preparation, and analysis chambers (up to three liquid and two pressurized gas sources can be loaded), and an Omicron VT STM (version XA purchased in October, 2011) with a Qplus AFM option in 223 Watson. The entire system was designed and assembled by Seokmin Jeon. Inset in b) displays base pressures of the analysis chamber (top), preparation chambers (center and bottom) in torr. Top and bottom pressure were measured by Varian extended-range UHV nude ion gauges (UHV-24p). Picture b) was taken in October, 2013.

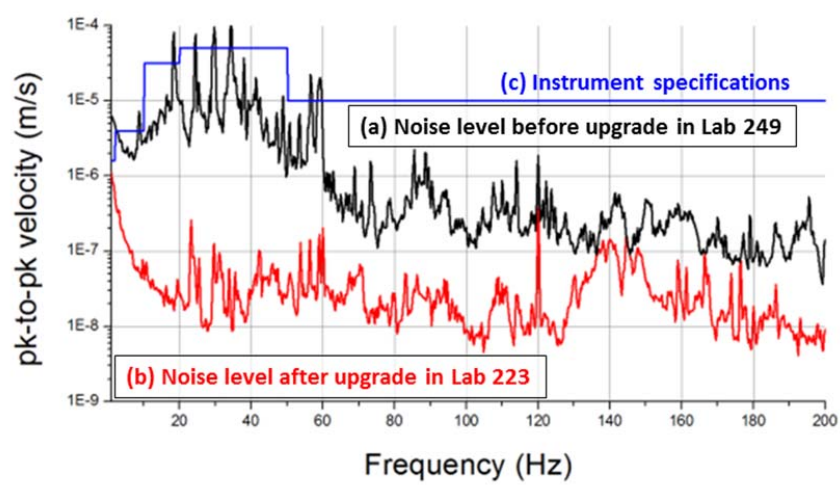


**Figure A.4** Peak-to-peak velocity versus frequency plots measured on two different systems; a) the system described in Figure A.2 located in 249 Watson and b) the system described in Figure A.3 located in 223 Watson. c) rule-of-thumb noise specifications supplied by Omicron. The data were collected using PCI accelerometers along the floor normal direction.